

AD-A105 872

PHOTOMETRICS INC WOBURN MA

F/G 18/3

EVALUATION OF INFRARED SIMULATION DATA.(U)

NOV 80 I L KOFSKY, D P VILLANUCCI, R B SLUDER

DNA001-80-C-0010

UNCLASSIFIED

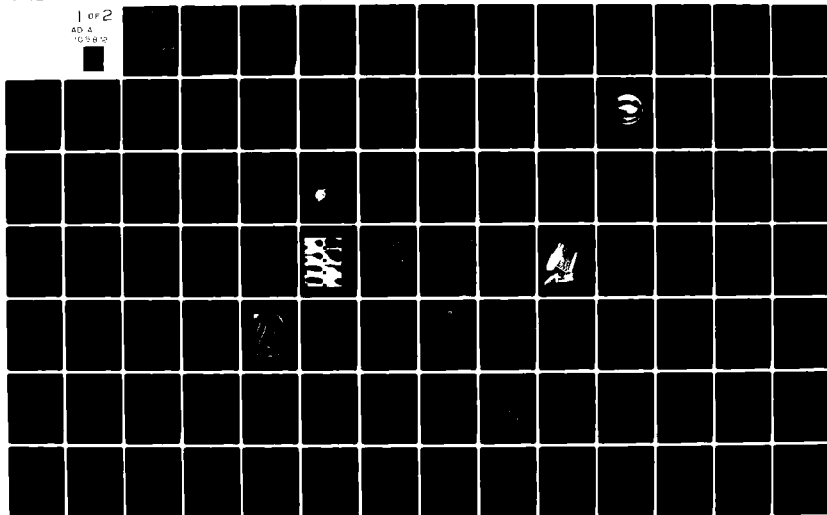
PHM-04-80

DNA-5521F

NL

1 of 2

AD A  
10 5 8 0



**12** LEVEL

DNA 5521F

AD A105872

# EVALUATION OF INFRARED SIMULATION DATA

PhotoMetrics, Inc.  
4 Arrow Drive  
Woburn, Massachusetts 01801

26 November 1980

Final Report for Period 1 December 1979—31 October 1980

CONTRACT No. DNA 001-80-C-0010

APPROVED FOR PUBLIC RELEASE;  
DISTRIBUTION UNLIMITED.

DTIC  
ELECTE  
OCT 20 1981  
S D  
B

THIS WORK SPONSORED BY THE DEFENSE NUCLEAR AGENCY  
UNDER RDT&E RMSS CODE B322080462 I25AAXHX63911 H2590D.

DTIC FILE COPY

Prepared for  
Director  
DEFENSE NUCLEAR AGENCY  
Washington, D. C. 20305

Destroy this report when it is no longer needed. Do not return to sender.

PLEASE NOTIFY THE DEFENSE NUCLEAR AGENCY,  
ATTN: STTI, WASHINGTON, D.C. 20305, IF  
YOUR ADDRESS IS INCORRECT, IF YOU WISH TO  
BE DELETED FROM THE DISTRIBUTION LIST, OR  
IF THE ADDRESSEE IS NO LONGER EMPLOYED BY  
YOUR ORGANIZATION.



UNCLASSIFIED

SECURITY CLASSIFICATION OF THIS PAGE (When Data Entered)

REPORT DOCUMENTATION PAGE		READ INSTRUCTIONS BEFORE COMPLETING FORM
1. REPORT NUMBER DNA 5521F	2. GOVT ACCESSION NO. 4D-A105872	3. RECIPIENT'S CATALOG NUMBER
4. TITLE (and Subtitle) EVALUATION OF INFRARED SIMULATION DATA	9	5. TYPE OF REPORT & PERIOD COVERED Final Report for Period 1 Dec 79- 31 Oct 80.
7. AUTHOR(s) Irving L. Kofsky Dennis P. Villanucci Randall B. Sluder	14	6. PERFORMING ORG. REPORT NUMBER Ph11-84-80
9. PERFORMING ORGANIZATION NAME AND ADDRESS PhotoMetrics, Inc. 4 Arrow Drive Woburn, Massachusetts 01801	15	8. CONTRACT OR GRANT NUMBER(s) DNA 001-80-C-0010
11. CONTROLLING OFFICE NAME AND ADDRESS Director Defense Nuclear Agency Washington, D.C. 20305	11	10. PROGRAM ELEMENT PROJECT, TASK AREA & WORK UNIT NUMBERS Subtask I25AAXHX639-11
14. MONITORING AGENCY NAME & ADDRESS (if different from Controlling Office)		12. REPORT DATE 26 November 1980
		13. NUMBER OF PAGES 126
		15. SECURITY CLASS (of this report) UNCLASSIFIED
		15a. DECLASSIFICATION DOWNGRADING SCHEDULE N/A
16. DISTRIBUTION STATEMENT (of this Report)  Approved for public release; distribution unlimited.		
17. DISTRIBUTION STATEMENT (of the abstract entered in Block 20, if different from Report)		
18. SUPPLEMENTARY NOTES  This work sponsored by the Defense Nuclear Agency under RDT&E RMSS Code B322080462 I25AAXHX63911 H2590D.		
19. KEY WORDS (Continue on reverse side if necessary and identify by block number) Nuclear-Effects Simulation                      Spaceborne Electron Accelerators Upper Atmosphere                                  Aurora and Airglow Infrared Radiation                                  Artificial Airglows Radiometry and Photometry		
20. ABSTRACT (Continue on reverse side if necessary and identify by block number) Infrared/optical nuclear-effects simulation data from DNA/AFGL sounding rockets HIRIS II (MWIR-LWIR auroral spectrum survey) and EXCEDE: Spectral (atmospheric excitation by a 3-keV electron beam) and instrumented NKC-135A aircraft are evaluated and interpreted. Most of the particle-irradiated air within HIRIS's field of view during high signal/noise spectrum scans near the atmosphere's limb is at altitudes 10's km distant from the rocket. Excitation altitude		

387376

JCS

## 20. ABSTRACT (Continued)

profiles and total column energy input rates for calibrating and scaling the infrared spectral intensities are calculated.

The brightness distribution of air near EXCEDE: Spectral, measured at 113 and 123 km altitude with radiometrically calibrated onboard cameras, is found to differ markedly from predictions of code models. The intensity and broadening of the radiating volume suggest that a discharge may be taking place within a few meters of the accelerators; beyond this distance the electron beam's transport appears to be as expected. A plasma with high concentrations of 10 eV temperature electrons is consistent with many of the optical/IR features that were observed, among them the H<sub>2</sub>O, enhanced CO<sub>2</sub>, continuum, and strong N<sub>2</sub>-triplet manifold emissions. It is suggested that discharges excited by charged particle beams ejected from sounding rockets may allow verification of theoretical models of the intensity of plasma radiations excited by nuclear explosions.

Recent aircraft measurements of zenith 2.8-3.1 μm sky background enhancements induced by particle precipitation again show correlation with energy input to within a few sec and a few km horizontally in most aurora. Further evaluation of those segments of the radiance data with longer decay times, which appear to be associated with the sunlit ionosphere, is underway.

RE: Reference to Classified Paper on Page  
109

No change in distribution statement per Ms.  
Melanie Bell, DNA/TISI

Accession For	
NTIS GRA&I	<input checked="" type="checkbox"/>
DTIC TAB	<input type="checkbox"/>
Unannounced	<input type="checkbox"/>
Justification	
By	
Distribution/	
Availability Codes	
Dist	Avail and/or Special
<b>A</b>	

## SUMMARY

The objective of the work reported here is to evaluate and interpret sounding rocket and aircraft data on atmospheric IR/optical radiations resulting from natural and artificial inputs of energy that simulate high-altitude nuclear explosions. The field measurements, which were directed by Air Force Geophysics Laboratory under Defense Nuclear Agency sponsorship, are described in reports of recent program reviews (Ref's 1, 2). Data from the HIRIS II and EXCEDE: Spectral rockets and the 1979-80 auroral missions of AFGL's optical aircraft are addressed. Evaluations of other data segments by PhotoMetrics (who also participated in the field operations) are documented in previous DNA reports (Ref's 3-7).

Energy deposition within the field of view during sixteen high signal/noise spectrum scans of HIRIS II is calculated (in Section 1). The changing aspect of the rocket (IC630.02-1A, flown to 123 km at Poker Flat Research Range on 01 Apr 76) caused the MWIR- and LWIR-sensitive spectrometer to view space- as well as time-varying distributions of particle excitation. Altitude profiles of the volume excitation rate at the midpoint of the 1.26-sec interferometer mirror sweeps were also calculated from the Poker Range photometry and incoherent-scatter radar data; this profile, like the total column energy input, changes as the instrument field sweeps across the auroral limb. Most of the deposition is in general separated by  $\sim 10$ 's km in altitude from the rocket. This altitude distribution serves in determining the dependence of yields of infrared features - in particular, the NO vibrational fundamental sequence above  $5.3\mu\text{m}$  - on the ambient species concentrations (and atmospheric temperature). The total column energy inputs calibrate and thus help scale to nuclear interchange scenarios the IR spectral intensities measured at the charged particle fluxes reached in the natural aurora.

Brightness distributions of the air into which 3 keV electrons are injected from EXCEDE: Spectral (A51.970, flown to 128 km at Poker Range on 19 Oct 79) are derived from photographs taken by wide-angle cameras onboard the payload (Section 2). (The camera system had been initially designed, built, and radiometrically and geometrically calibrated by PhotoMetrics.) The images of the glow, which are the first such achieved, are presented in radiance contour plots suitable for comparison to predictions of code models of electron transport in the atmosphere. The surface radiance pattern is sufficiently cylindrically symmetric to permit straightforward unfolding of 3-dimensional volume emission rate distributions.

Glow dimensions and radiances at the two altitudes assessed (123 km upleg and 113 km downleg) differ markedly from calculated values within a few meters of the accelerators, beyond which the electron beam appears to deposit energy as expected. Direct impact excitation of molecules outgassed from the vehicle and accelerators does not appear to explain the photographic data. The intensity and broadening of the close-in optical emissions suggest that a discharge, similar to those observed near several other ~kilovolts electron-ejection rockets, is contributing to the optical excitation within the fields of EXCEDE: Spectral's instruments. Further information on this effect will come from the spectral intensities and ratios measured by the onboard instruments and the spatial distribution of visible radiance measured by the groundbased cameras.

A discharge with ~eV's electron temperature in the vicinity of the accelerators is consistent with many of the optical/IR spectrum features that have been reported, among them the 2.7, 6.3 and 17 - 22 $\mu$ m H<sub>2</sub>O emissions; the strong N<sub>2</sub>-triplet manifold (Wu-Benesch, Herman-Kaplan, and Second Positive bands); the excess CO<sub>2</sub>-band radiation at 4.3 $\mu$ m (vibrational excitation of N<sub>2</sub>, which is rapidly transferred to CO<sub>2</sub>, is efficiently produced by soft electron impact) and 15 $\mu$ m; the continuum underlying the discrete emissions; and perhaps others. It is recommended that in future EXCEDE investigations plasma conditions

in the region viewed be diagnosed by sensors of the type applied in electron-injection experiments from sounding rockets and in large laboratory tanks (in particular, electron energy spectrometers and radiofrequency wave analyzers); and that discharges in the F-region induced by charged-particle beams be considered as a means of verifying DNA/DoD models of the infrared spectral intensity of the plasma radiation backgrounds excited by high altitude nuclear explosions.

Support was provided to AFGL in locating ground stations for triangulation to auroral forms within the field of radiometers on the ELIAS earth limb-scanning rocket (Ref 2), and in transfer-calibrating the aircraft's energy input-measuring photometer (Sections 3 and 4). The overlap of fields of wide angle cameras at logistically-supportable sites underneath the morning-sector auroral oval near the tangent intercepts of ELIAS (scheduled for launch from Poker Range in Feb 81), was calculated by coordinate transform methods. Auroral radiance data taken by a second photometer onboard AFGL's optically-instrumented aircraft (NKC-135A S/N 55-3120), which is otherwise used to determine altitudes of peak particle-energy deposition and intensities of  $\text{NO}^+$  precursor species emissions, were used to cross-calibrate the photometer that determines energy input for the high spatial resolution 2.8 - 3.1  $\mu\text{m}$ -band radiometer.

Further measurements on auroral particle-excited air by these  $0.4^\circ$ -field instruments again show that the SWIR temporal-spatial inhomogeneities correlate with column energy input to within a few sec and a few km horizontally. Some of the data on the sunlit auroral ionosphere, however, indicate longer characteristic decay and rise times of the SWIR radiance. Some fifteen  $\sim 5$ -min segments of data from IBC  $\geq$  II twilight and nighttime aurora have been identified for further evaluation; auroral and observation parameters, such as altitude of peak energy deposition, solar angle and earth's shadow height, orientation of the radiometer and photometer with respect to the geomagnetic field, and previous atmosphere dosing have been tabulated for these events. (Final calibrations were not applied to these flight data in time for us to determine visible-infrared correlation parameters.)

## PREFACE

This is the Final Report on Contract DNA001-80-C-0010, covering evaluation and interpretation of data from simulations of optical/IR sky backgrounds excited by atmospheric nuclear detonations. Field data from the following sources, taken by Air Force Geophysics Laboratory and contractor personnel (including PhotoMetrics) under sponsorship of the Defense Nuclear Agency, are considered.

- HIRIS II LWIR spectrometer rocket IC630.02-1A,  
(01 Apr 76)
- EXCEDE: Spectral electron-injection rocket  
A51.970 (19 Oct 79) and
- USAF NKC-135 A Aircraft 55-33120 (auroral  
flight missions in 1979-80).

Additional tasks included planning for ground measurements supporting the ELIAS rocket and support in calibrating aircraft instruments.

This work was done under the direction of I. L. Kofsky. Mrs. C. C. Rice was responsible for typing the manuscript. Information about the field measurements were made available by staff of AFGL's Optical Physics (OPR) branch, in particular E. R. Huppi and R. R. O'Neil, and useful modeling data was supplied by D. H. Archer of Mission Research Corp. and G. E. Caledonia of Physical Sciences, Inc. The authors also acknowledge the support and encouragement of A. T. Stair Jr. of AFGL, and Capt. P. Lunn, Lt. Col. W. McKechney, and Dr. H. C. Fitz Jr. of the Defense Nuclear Agency.

## TABLE OF CONTENTS

<u>Section</u>	<u>Page</u>
SUMMARY .....	1
PREFACE .....	4
LIST OF ILLUSTRATIONS .....	7
LIST OF TABLES .....	10
1   PARTICLE ENERGY DEPOSITION RATES IN HIRIS II's FIELD .....	11
INTRODUCTION .....	11
APPLICATION OF THE DATA .....	13
FURTHER HIRIS OBSERVATIONS .....	14
PROCEDURE .....	15
ALTITUDES OF ENERGY DEPOSITION .....	36
SUMMARY .....	36
2   SPATIAL DISTRIBUTION OF ENERGY DEPOSITION BY EXCEDE: SPECTRAL's ELECTRONS .....	39
BACKGROUND .....	39
INSTRUMENTATION .....	41
CALIBRATIONS .....	47
GEOMETRY OF VIEWING .....	51
APPLICATION OF THE RADIANCE DATA .....	52
PRELIMINARY OVERVIEW OF THE FILM DATA .....	53
METHOD OF FILM DATA ACCESS .....	57
GLOW RADIANCE DISTRIBUTIONS AND DIMENSIONS .....	60
SUMMARY AND RECOMMENDATIONS .....	68
3   POSITIONING PHOTOGRAPHIC STATIONS FOR TRIANGULATION TO ELIAS AURORAL FORMS ....	72
BACKGROUND .....	72
PROJECTION OF THE CAMERA FIELDS .....	74
COMMENTS .....	76
4   TRANSFER CALIBRATION OF THE AIRCRAFT PHOTOMETER .....	78
INTRODUCTION .....	78
PHOTOMETER OPTICS .....	78
TRANSFER CALIBRATION .....	82
APPLICATION .....	87

TABLE OF CONTENTS (Concluded)

SECTION	PAGE
5 AIRCRAFT SWIR STRUCTURE DATA .....	88
REFERENCES .....	92
APPENDIX	
I INFRARED SKYGLOW FROM IONOSPHERE RECOMBINATION .....	95
II DNA/AFGL NUCLEAR WEAPONS EFFECTS CHEMISTRY CONFERENCE .....	109
III AURORAL ALTITUDES .....	113

## LIST OF ILLUSTRATIONS

<u>Figure</u>		<u>Page</u>
1.	Pointing of the HIRIS II (IC 630.02-1A) spectrometer's optic axis at the beginning and end of the 16 scans for which column energy input rates and altitudes have been derived .....	12
2.	All-sky view from Fort Yukon of the distribution of visible air fluorescence between 100 and 109 sec after launch of HIRIS II .....	19
3.	Meridian-plane projection of HIRIS II's pointing on the model fluorescing regions during scans 23 and 24 .....	20
4.	Power inputs within HIRIS II's field during the eight scans assessed in this report .....	23
5.	All-sky view from Poker Flat of the distribution of visible air fluorescence between 248 and 253 sec after launch of HIRIS II, with the projection of the optic axis of the spectrometer into the film plane during scans 136 and 137 .....	28
6.	Meridian plane projection of the HIRIS II spectrometer's viewing geometry on the model fluorescing regions during scans 136 and 137. ....	29
7.	Elevation scan from PKR in a vertical plane $16^{\circ}$ E of N starting in the north at 257 sec after launch of HIRIS II, with identification of emitting regions .....	30
8.	Elevation scans from PKR in a vertical plane $16^{\circ}$ E of N between 277 and 297 sec after launch of HIRIS II, with projections of the 120 km intercepts of the spectrometer and DNA 617 radar fields and the rocket's position .....	32
9.	Altitude profiles of $3914 \text{ \AA}$ volume emission rate in HIRIS's field at the midpoint of each spectral scan... ..	34
10.	Mean power input within HIRIS II's field during half-scans and at the mid-point of the interferometer excursion in each of the sixteen scans reduced .....	37

LIST OF ILLUSTRATIONS (Continued)

<u>Figure</u>	<u>Page</u>
11. Typical photographs from onboard of the air fluorescence excited by EXCEDE; Spectral's electron accelerators on upleg and downleg .....	42
12. Side view of the camera fields and region of atmosphere into which electrons from EXCEDE; Spectral accelerator #4 deposit energy .....	43
13. Relative spectral response of the monochrome (EK 2475 film) photometric camera with 5.7 mm, f/1.8 lens .....	45
14. View of the intervalometer assembly and two 16 mm cameras .....	46
15. Relative irradiance in the image plane and field-of-view half-angle as a function of displacement of the image point from the center of the EXCEDE; Spectral cameras' field .....	50
16. Plot for relating positions on uncorrected (for lens distortion) equidensity contour plots to distances in object space .....	54
17. Equi-density contour plot from 0.08 sec exposure at 123 km upleg, EXCEDE; Spectral .....	55
18. Radiance distribution projected to the onboard camera at 123 km upleg, EXCEDE; Spectral .....	58
19. Radiance distribution projected to the onboard camera at 113 km downleg, EXCEDE; Spectral .....	59
20. Radiance projected to the onboard camera along the electron beam's axis and viewing perpendicular to the axis at 123 km upleg, EXCEDE; Spectral .....	63
21. Radiance projected to the onboard camera along lines perpendicular to the electron beam's axis at 123 km upleg, EXCEDE; Spectral .....	64

LIST OF ILLUSTRATIONS (Concluded)

<u>Figure</u>	<u>Page</u>
22.	Radiance projected to the onboard camera along the electron beam's axis at 113 km downleg. EXCEDE: Spectral ..... 76
23.	ELIAS limb-viewing geometry with 120 km projections of the $75^\circ$ zenith angle contours from each ground site and $Q=4$ auroral oval at 0930 UT ..... 73
24.	Transformation geometry illustrating the procedure referencing zenith angle contours from Watson Lake to a coordinate system with origin at Fort Nelson, Canada ..... 75
25.	120 km projections of five contours of zenith angle from Watson Lake and Tuchtua at Fort Nelson, Canada ..... 77
26.	Model relative spectral sensitivity of the narrow-field aircraft photometer and spectrum of the $N_2^+$ 0, 0 First Negative band at 200 K rotational temperature ..... 81
27.	5577 Å and 3914 Å column brightnesses measured by the 12-channel photometer overlaid on the voltage output signal from the near-coaligned narrow field aircraft instrument ..... 83
28.	Cross-plot of $N_2^+$ First Negative band intensities measured by the aircraft's 12-channel photometer and signal output from the narrow-field photometer in a segment of Flight 911 ..... 84
29.	Cross-plot of OI 5577 Å line intensities measured by the 12-channel photometer and signal output from the aircraft's narrow-field photometer ..... 85

LIST OF TABLES

<u>Tables</u>		<u>Page</u>
1.	Summary of HIRIS II's pointing geometry, average power input within the spectrometer field in half-scans and power input at the midpoint of the spectrum scans .....	17
2.	Summary of specifications of EXCEDE: Spectral's photographic system .....	40
3.	SWIR emission data flights of narrow-field radiometer/photometer, 1979 .....	79
4.	Auroral and observation parameters during SWIR enhancements .....	89

## SECTION I

### PARTICLE ENERGY DEPOSITION RATES IN HIRIS II's FIELD

#### INTRODUCTION

We have determined column integrated particle-energy input rates for seven additional near limb-viewing spectrum scans of HIRIS II (IC 630.02-1A, 01 Apr 76) following the procedure described in Section 2 of Ref 3 and Section 2 of Ref 4. Altitude profiles of the energy deposition at the scans' centers were also calculated. This brings to 16 the number of double-sided interferograms for which "input" information has been derived from the ground-based radiance (meridian-scanning photometer and all-sky camera) and electron density (incoherent-scatter radar) data on the auroral forms.

The pointing history of the tumbling/precessing  $2^\circ$  field of the instruments is documented in Ref 5, and the directions and altitudes of its optic axis during each of the 4- $22\mu\text{m}$  spectrum scans addressed are shown in Fig 1. The field in effect described a cone of  $165^\circ$  apex angle with axis near  $9^\circ$  el  $-130^\circ$  geomagnetic az (that is, toward the southeast), once each 34.5 sec. This rotation pointed HIRIS alternatively into the nadir hemisphere, where it sees thermal radiation from the atmosphere and earth surface, and near the limb and into the upper hemisphere, where it measures aurorally-excited infrared emissions (along with some thermal radiation and scattered earthshine). Changes of up to  $14^\circ$  in instrument elevation during the 1.26 sec of the interferometer mirror scans produced a broad range of intercept altitudes on distant ( $\sim 100$  km horizontally) regions of particle precipitation, and thus substantial variability in the instantaneous power inputs (as was shown by the previously-reduced data).

The long optical paths near the earth's limb were found to provide the highest signal/noise infrared spectra. As Fig 1 shows, HIRIS's field is nearly horizontal toward the southwest, where the aurora

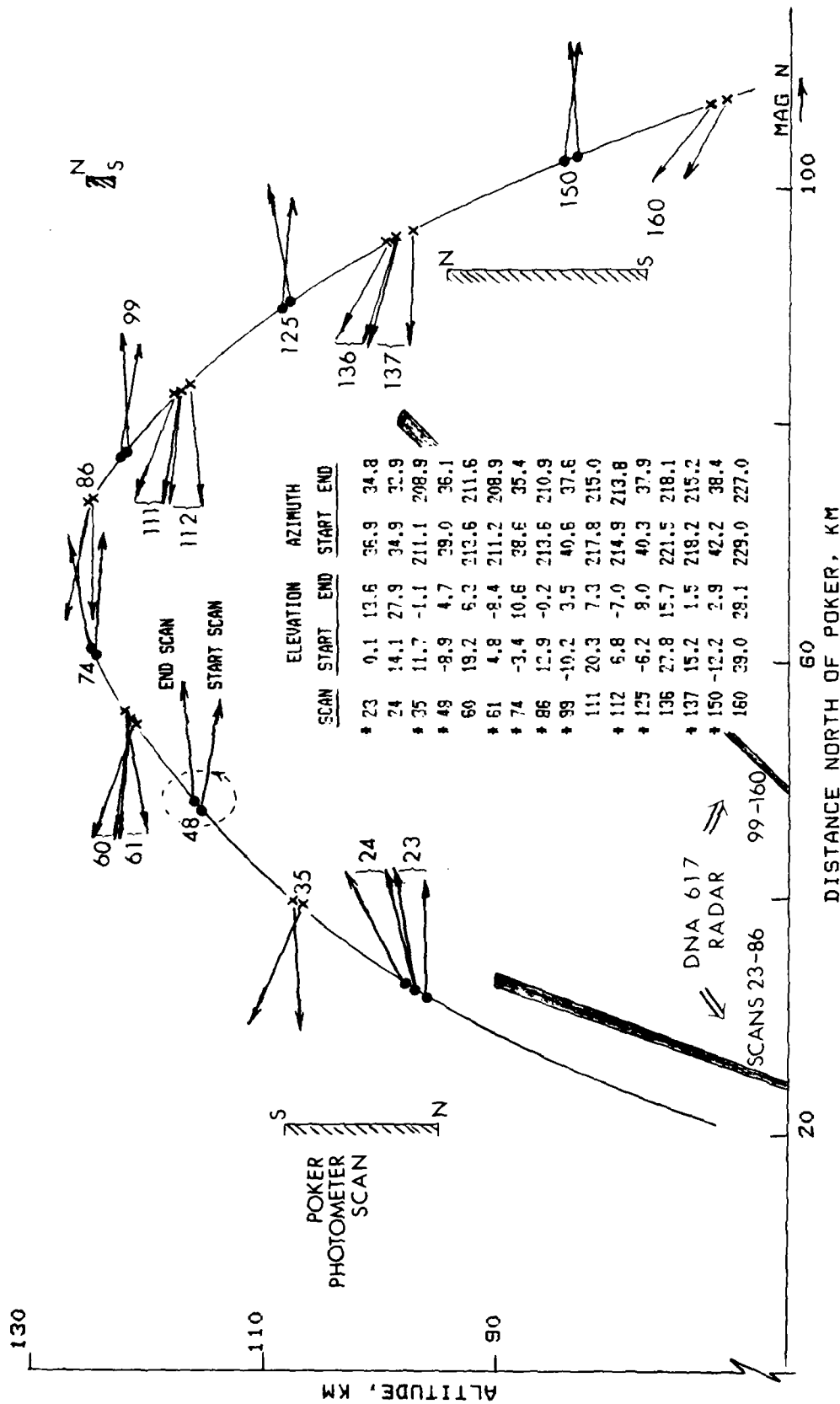


Figure 1. Pointing of the HIRIS II (IC 630.02-1A) spectrometer's optic axis at the beginning and end of the 16 scans for which column energy input rates and altitudes have been derived. The rocket's trajectory has been projected into the geomagnetic meridian plane passing through Poker Flat. The relative lengths of the arrows indicate cosine of azimuth angle west (x), or into the paper, and east (o) identifies spectrum scans included in the data evaluation of Ref 8. Altitudes traversed by the rocket during three elevation scans of the PKR-USU auroral photometer and the projection into the meridian plane of the incoherent-scatter radar's field are shown.

consists of bright arcs, and toward the northeast, where the precipitation produces diffuse glows. A montage of all-sky projections to Poker Flat and Fort Yukon is in Fig 58 of Ref 6, and enlargements of photographs at times when the interferometer scans near the limb are in Ref's 3 and 4.

#### APPLICATION OF THE DATA

The information in this Section serves to reference the atmosphere's output of medium- and long-wavelength infrared radiations to the input of ionizing-exciting particle energy, and to identify effects of altitude (i. e., concentration of ambient species) at which this energy is deposited.

The energy inputs that we derived previously have been applied in a recent determination from HIRIS limb spectra (Ref 8) of the aurora's efficiency for production of nitric oxide ( $X^{2\pi}$ ) vibrational fundamental radiation. It was found that the NO  $\Delta v = 1$  ( $5.3\mu\text{m}$ -band) cascade sequence emission follows the simultaneously-measured power inputs (from Ref 3); that effective yields are  $1.1 \pm 0.5\%$ , with a further uncertainty of a factor 2 from the calibration of the infrared spectrometer; and that the upper vibrational-state distribution forming the cascade spectrum does not change with rocket altitude over the range 100 to 125 km (within the errors in the relative spectral radiances). We note that the effective emission altitudes are in general considerably different from the spectrometer's altitude, as the instrument typically points several degrees from the horizontal toward aurorally-excited air volumes hundreds of km distant (see, for example Fig's 3 and 6); this issue is addressed later in this Section.

The  $\Delta v = 1$  sequence's spectral distribution and its apparent invariance with altitude led to the conclusion (Ref 8) that collisional relaxation of NO(v), presumably by the atmosphere's O atoms, dominates the otherwise-expected radiative (cascade) relaxation. In contrast, data from two DNA/AFGL rocketborne filter radiometers that pointed at high zenith angles into nearby isolated arcs indicate

that the effective total yield in the NO overtone ( $2.8\mu\text{m}$ -band) system changes by a factor two between 100 and 125 km rocket altitude (Ref 3). This finding of an altitude variation is semiquantitatively supported by model calculations of quenching of  $\text{NO}^{\ddagger}$  by O (Ref 9). Further, both the mean  $\Delta v = 2$  yield measured from these rockets and the vertical column-integrated "fluorescence" yields measured with the AFGL/DNA aircraft's SWIR radiometer (Ref 3), which average near 0.6%, are about a factor five higher than would be predicted were collisional deactivation of  $\text{NO}^{\ddagger}$  substantially more probable than radiation at all energy-deposition altitudes. Thus the aforementioned results from HIRIS are not in agreement with the current DNA model of background radiation in the  $2.8\mu\text{m}$  band, which is based on field and laboratory data on what is interpreted as  $\Delta v = 2$  emission from NO molecules. (We note that the unexpected distribution in upper-state population inferred from the HIRIS spectra has a small effect on the overlap of the aircraft radiometer's passband on this overtone spectrum, and negligible effect on the overlap of the wide-band ( $2.4 - 3.1\mu\text{m}$ ) rocket radiometers.)

The column power inputs that we determined previously were found to be approximately proportional to the intensities of the simultaneously-measured cascade radiation in the NO fundamental band. This component of the  $\Delta v = 1$  spectrum is interpreted as coming from the  $\text{NO}^{\ddagger}$  being produced by reaction of ambient  $\text{O}_2$  with  $\text{N}^2\text{D}$  atoms, which are a primary and secondary product of ionization and dissociation by electron impact; a second component, in the 1,0 band, comes from thermal reaction of NO with O atoms and scattering of earthshine from NO. "Input" data for further infrared spectrum scans serve to relate the observed variation about the mean in fundamental-band yield to ambient species concentrations. The calculations of excitation altitude profiles define the range of emission altitudes over which the infrared spectrum's shape is observed to remain unchanged.

#### FURTHER HIRIS OBSERVATIONS

Rotational temperatures in the R branch of the 1,0 band, which unlike the other  $\Delta v = 1$  R branches is not overlaid by P-branch lines

of the adjoining vibrational-fundamental transition, were also estimated from the HIRIS spectra (Ref 8). These temperatures provide some measure of the effective altitude from which this radiation originates, as the altitude profile of kinetic temperature in the auroral atmospheres is known with reasonably good accuracy. However, since most of the emission in the 1,0 band results from the "chemiluminescent" reaction of NO with O the temperatures, which in any case cannot be determined with high precision from the measured ratios of rotational line intensities, are not an effective check on our calculations of the spatial distributions of visible air fluorescence. That is to say, the mean altitudes from which arises the component of nitric oxide vibrational-rotational radiation excited in reactions of  $N^2D$  with  $O_2$  cannot be reliably inferred from the HIRIS infrared spectra. We note that a mean energy deposition altitude could be derived from an onboard-rocket measurement of intensity ratios in the R branch of an  $N_2^+$  First Negative fluorescence band, which is readily made with a pair of narrow-band filter photometers (see for example, Ref 10).

The near-limb column intensity in the chemiluminous component of the NO 1,0 band was observed (Ref 8) to remain constant within experimental error at rocket altitudes between 100 and 125 km. This is interpreted as being due to a near-constant volume emission rate in the feature, the decreasing concentration with altitude of O and NO being compensated by the increase in reaction rate coefficient. This effect was previously observed (Ref 7) in the zenith-pointing circular variable filter spectrometer data from HAES rockets NJ 74-1 (11 Apr 74, "quiet" ionosphere) and A18.219-1 (25 Feb 74, little auroral activity overhead). The absolute volume emission rates measured from those earlier rockets were near  $5 \times 10^4$  photons/cm<sup>3</sup> sec, while that from HIRIS in a heavily predosed atmosphere is  $10 \times 10^4$  photons/cm<sup>3</sup> sec ( $1\frac{1}{2} \times 10^{12}$  photons/cm<sup>2</sup>-sec from an approximately-150 km sight path).

#### PROCEDURE

Hiris's first 12 spectrum scans record emission from the instrument cover and an inflight calibration-verification source. The spectrum from Scan 14 shows the cover to be fully open when

the rocket reaches  $88\frac{1}{2}$  km altitude,  $86\frac{1}{2}$  sec after launch. The spectra through Scan 22 (95.3 km) exhibit very strong earthshine and atmospheric absorption-emission features, with no detectable auroral component. In Scan 23 (96.3 km) the spectrometer field has swung above the horizontal and points toward the north-lying aurora; we defined this scan as starting Rotation 1 (in Ref 4). On downswing, for example in Scan 35 (see Fig 1), the southern arcs come into the field. Rocket apogee is 125.3 km, and after 5.5 rotations (starting from Scan 23) the instrument door begins to close at 66.3 km altitude (during Scan 164). Each 1.26-sec interferometer mirror sweep is followed by a 0.10-sec flyback.

We again applied meridian-scanning photometer and all-sky photographic data taken from the ground stations at Poker Flat (Ref's 11 and 12) and Fort Yukon (Ref 11), and some of the ionospheric electron density profiles measured by the DNA 617 incoherent-scatter radar at Chatanika, to determine north-south extents and maximum energy deposition altitudes in the particle-precipitation regions. The derivation of model volume emission rate profiles from optical triangulation and emission-intensity data is outlined in Section 2 of Ref 4, and the procedure used to correct for out- and in-scattering of auroral radiation by the lower atmosphere is in Section V of Ref 6.

Table 1 is a listing of the pointing geometry, average power inputs within HIRIS's field in half-scans, and (in the last column) the power input at the center of the interferometer mirrors sweep for the sixteen scans. This last quantity is tabulated because (as noted in Ref 8) the integral over frequencies of a spectral band is proportional to its intensity component at the position of zero path difference in the interferogram, that is, at the sweep center. Energy deposition rates are given in units of line-of-sight column intensity in the  $N_2^+$  First Negative 0,0 band;  $21\frac{1}{2}$  ion pairs are produced per  $3914 \text{ \AA}$  photon emitted at 100 km, 23 at 123 km, and 24 at 140 km altitude (Ref 13). Details of the data evaluation for the new scans 23 N,

Table 1. Summary of HIRIS II's pointing geometry, average power input within the spectrometer field in half-scans, and power input at the midpoint of the mirror scan.

SCAN	TIME, SEC		ALTITUDE, KM		ELEVATION, °		MAG AZ, °		POWER INPUT, KR 3914Å EQUIV		
	START	END	START	END	START	END	START	END	AVG 1st HALF	AVG 2nd HALF	SCAN CTR
23 N	100.9	102.1	96.3	97.2	0.1	13.6	36.9	34.8	91	68	87
24 N	102.2	103.4	97.3	98.2	14.1	27.9	34.9	32.9	25	9	19
35 S	117.0	118.3	107.0	107.7	11.7	-1.1	211.1	208.9	206	214	230
48 N	134.6	135.9	115.9	116.4	-8.9	4.7	39.0	36.1	58	214	186
60 S	150.8	152.1	121.5	121.8	19.2	6.3	213.6	211.6	46	101	76
61 S	152.2	153.5	121.8	122.1	4.8	-8.4	211.2	208.9	237	261	330
74 N	169.7	171.0	124.9	125.0	-3.4	10.6	38.6	35.4	87	65	90
86 S	185.9	187.1	125.1	125.0	12.9	-0.2	213.6	210.9	64	214	115
99 N	203.5	204.8	122.6	122.3	-10.2	3.5	40.6	37.6	124	258	226
111 S	219.7	221.0	117.7	117.2	20.3	7.3	217.8	215.0	251	321	282
112 S	221.0	222.3	117.2	116.7	6.8	-7.0	214.9	231.8	516	365	595
125 N	238.5	239.8	108.9	108.2	-6.2	8.0	40.3	37.0	79	109	129
136 S	253.4	254.6	99.5	98.7	27.8	15.7	221.5	218.1	18	27	21
137 S	254.7	256.0	98.6	97.7	15.2	1.5	218.2	215.2	53	115	64
150 N	272.3	273.6	84.6	83.5	-12.2	2.9	42.2	38.4	0*	14	0
160 S	285.8	287.0	71.8	70.5	39.0	28.1	229.0	227.0	26	30	28

\* POINTING BELOW AURORA

48N, 99N, 60S, 111S, 136S, and 160S ( N and S again identify north limb or south limb pointing: see Fig's 2 and 5) are as follows.

Scan 23 (96.8 km mean rocket altitude, 100.9-102.1 sec after launch)

Figure 2 is the all-sky image of visible air fluorescence at Fort Yukon between 100 and 109 sec. The projection onto the film plane of the instrument's line-of-sight at the beginning and end of Scan 23 is shown by the solid curved lines, and for comparison the pointing during adjoining Scan 24 as dashed lines.

Two broad auroral regions to the north of the rocket are vertically scanned as the instrument's elevation angle goes from  $0.1^\circ$  to  $13.6^\circ$ . We used the equidensity plot of this photographic frame with contours calibrated by the radiances measured by FYU's meridian photometer to assign apparent surface brightnesses (from FYU) to the two regions. The mean  $N_2^+ 0,1$  (4278 Å) band brightness in the more northerly region 1N is  $4\frac{1}{2}$  kR, and in 2N it is 8 kR. (Intensity in this band, which the FYU photometer measures, is  $(1/2.9) \times$  the 0,0 band intensity.) The altitude at which particle energy deposition peaks and the latitudinal extent of each region are taken to be the same as previously determined for Scan 24 (the same groundbased data apply to both spectrums). Figure 3 is a meridian plane projection of the viewing geometry.

Triangulation to arc 2N placed its altitude of peak deposition at 107 km, which is fit by a characteristic energy parameter  $\alpha = 5\frac{1}{2}$  keV in the usual power-exponential energy distribution of the precipitating electrons (Ref 6). The diffuse region 1N is too broad to permit effective triangulation from the two stations; applying the arguments in Ref 4 (p. 64), we assigned it the relative volume emission rate profile that results from a 3 keV characteristic energy (115 km peak). Absolute peak 4278 Å volume emission rates for the two regions (before correction for in- and out-scattering) are  $1.4 \times 10^3$  photons/cm<sup>3</sup> sec (1N) and  $3.0_5 \times 10^3$  photons/cm<sup>3</sup> sec (2N).

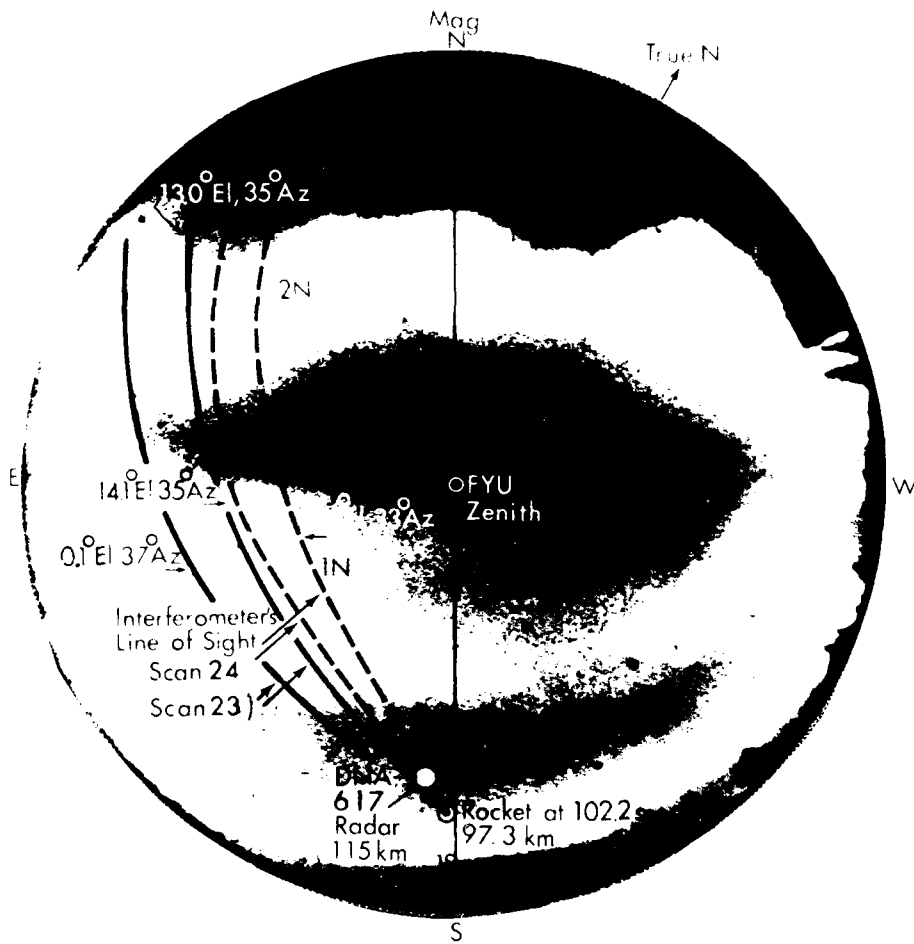


Figure 2. All-sky view from Fort Yukon of the distribution of visible air fluorescence between 100 and 109 sec after launch of HIRIS II. The projection of the axis of the spectrometer's field of view during scans 23 and 24 (with elevation and azimuth angles measured from the rocket), and the Chatanika radar beam's intercept at 115 km altitude are shown.



As shown in Ref 4 (pp 94-96), the effective "wide-beam" transmission of 4278 Å photons from the two regions is 1/1.3 and 1/2.0 respectively. We applied these corrections to the volume emission rate profiles, and then summed along the instrument's sight path during the interferometer scan. The resulting power input rates are in Fig 4, which summarizes the results for the seven new spectrum scans and gives corrected data for previously-reported Scan 137. Averages over half-scans and instantaneous power inputs at mid-scan are listed in Table 1 (as noted).

Both auroral regions contribute about equally to the column intensity in the direction of the field. The uncertainty in power input is expected to be due principally to errors in correcting for buildup and in absolute calibration of the photometer (as noted in Ref 4, the readings from the Fort Yukon unit required an upward correction), and secondarily in estimating the widths and latitudinal uniformity of the particle-precipitation regions. We estimate the accuracy of the power inputs for this spectrum scan as +65%, -50%.

Scan 48N (110.2 km, 134.6 - 135.9 sec)

Four precipitation regions contribute to the line of sight power input during Scan 48. The bright region well north of FYU (2N in Fig 3) developed into a double arc near 62° zenith angle (as shown in Fig 6 of Ref 3 and Fig 58 of Ref 6), and two broad diffuse regions centered at 26° and 32° from FYU also lay within the instrument's field.

The more southerly of the two far-northern arcs extended westward through the geomagnetic meridian, so that its brightness could be measured by the elevation-scanning photometer. Its altitude of peak radiance was estimated by triangulation to be 115 km ( $\alpha = 3$  keV). Since the arc a few degrees to the north has the same apparent surface intensity (15 kR 4278 from FYU) we assumed it to be at the same altitudes. The diffuse areas nearer the rocket were again too broad for effective triangulation; they were assigned 122 km peak energy

deposition altitude ( $\alpha = 1.9$  keV) on the basis of their lower intensities (near 5 kR 4278 Å in the projection to FYU).

An equi-density contour plot from the all-sky frame at 133 sec was used in assessing auroral brightnesses in the direction of the field northeast of the rocket. Contours were again assigned radiance values from the meridian photometer data. Peak volume emission rates after correction for vignetting by the all-sky camera lens (but not yet for atmospheric scattering) are  $4.0 \times 10^3$  in both northern arcs and  $1.0 \times 10^3$  in the two diffuse regions, in units of 4278 Å photons/cm<sup>3</sup> sec. Wide-beam lower atmosphere transmissions are (following the previous arguments) 0.45, 0.45, 0.68, and 0.61 respectively. The resulting column input rates are in Fig 4.

During Scan 48 the instrument's optic axis moves up from  $-8.9^\circ$  elevation, where it intercepts only the nearby diffuse emitting volumes, and by mid-scan all four auroral regions are viewed nearly horizontally. The average power input in the first and second halves of the scan interval is 58 and 214 kR (3914 Å units) (Table 1). This increase of a factor 3.7 is the largest fractional change between half scans in the HIRIS input data that we have assessed.

The uncertainty in energy input rates is particularly high for this scan because of the uncertainty in peak energy deposition altitude (and thus deposition profile) of all four regions, and in scaling intensities from a densitometric representation of the FYU all-sky film. A best-estimate of the expected error is +85%, - 60%.

#### Scan 99N (122.5 km, 203.5 - 204.8 sec)

The particle-precipitation distribution as seen from Fort Yukon at this time is in Fig 6 of Ref 3. The double arc far north of FYU (refer to the previous subsection) has merged into a single broad diffuse glow centered near  $60^\circ$  zenith angle,  $45^\circ$  az. As its apparent surface brightness is about 5 kR 4278 Å (as determined with the aid of an equidensity contour plot that extended through the meridian

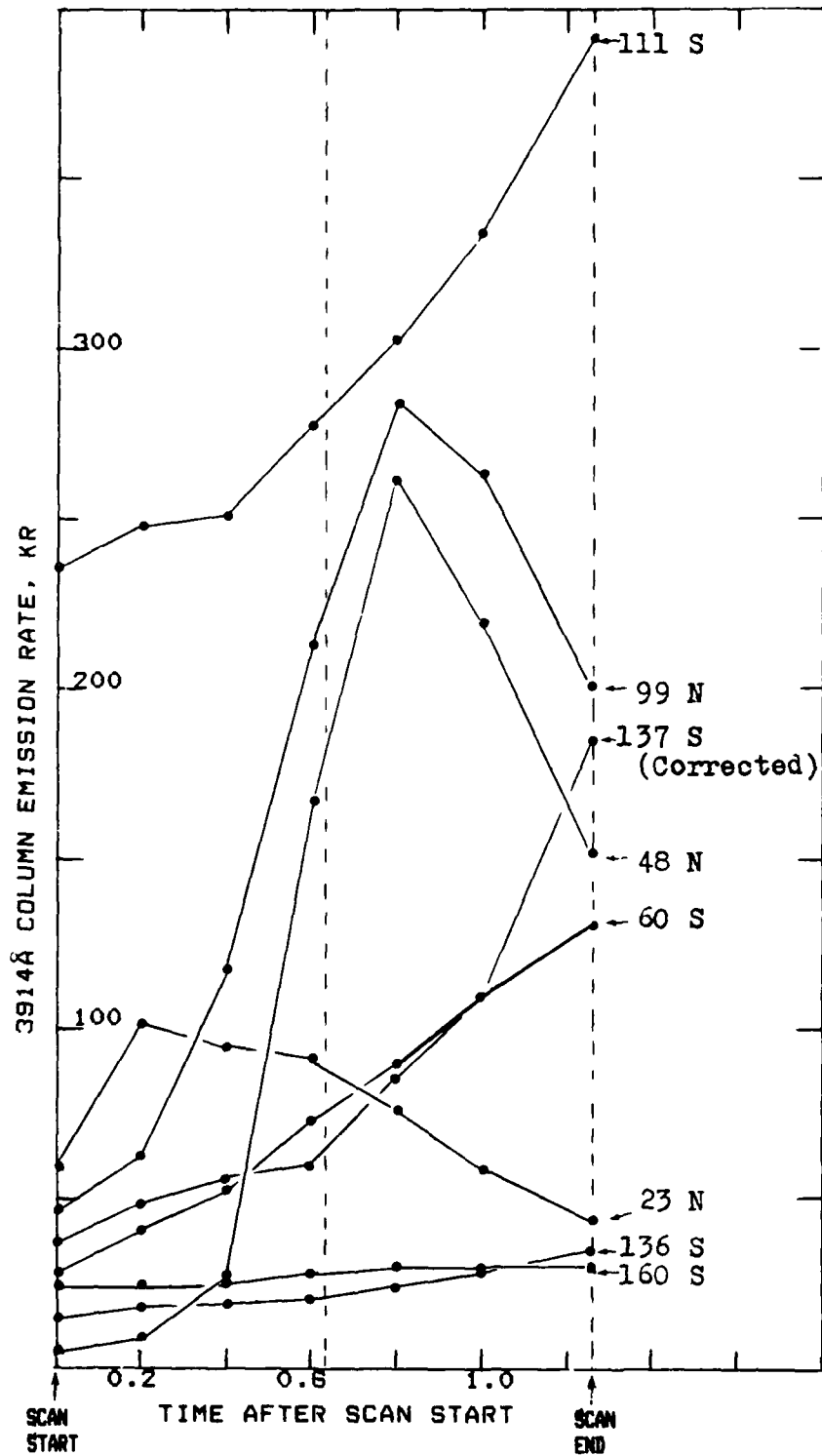


Figure 4. Power inputs within HIRIS II's field during the eight scans assessed in this report. Results for eight further scans are in Fig 9 of Ref 3 and Fig's 11 and 14 of Ref 4 .

plane), it was assigned a peak altitude of 122 km  $\alpha = 1.9$  keV. Two narrow diffuse regions near  $42^\circ$  zenith angle (north of FYU) and  $20^\circ$  (south) were assigned peaks at 117 km ( $\alpha = 3.0$ ) and 122 km ( $\alpha = 1.9$ ) on the basis of their relative brightnesses; two-station triangulation to these features was not possible. A more intense (21.5 kR), 15 km wide arc has also formed near the rocket position; its peak energy deposition altitude was determined by triangulation to be 107 km ( $\alpha = 5\frac{1}{2}$  keV).

During the first half of the (upswing) scan the instrument is pointing generally below the more northerly auroral regions (at  $-10.2^\circ$  to  $-4.3^\circ$  elevation); most of the energy input comes from the arc surrounding the rocket and the diffuse glow  $20^\circ$  S of FYU. Peak (uncorrected for scattering) 5278 Å volume emission rates were determined to be  $9.1 \times 10^3$  (arc) and  $1.0 \times 10^3$  (glow) 4278 Å photons/cm<sup>3</sup>-sec. These result in about equal contributions from each region to the total column power input (see Fig 4), the longer average path length through the 60 km wide glow compensating for its lower volume emission rates. Effective atmospheric transmissions were taken as 0.60(arc) and 0.69 (glow) in the final calculation of power input.

In contrast, the input signal in the second half of Scan 99 comes principally from the two diffuse glows north of FYU. Maximum (uncorrected) 4278 Å volume emission rates are  $2.0 \times 10^3$  photons/cm<sup>3</sup> in the  $42^\circ$  and  $6.1 \times 10^2$  photons/cm<sup>3</sup> sec in the  $60^\circ$  zenith angle regions. The column power input rises sharply near mid-scan as the field of the instrument, which is near the glows' peak emission altitude, approaches horizontal. 4278 Å wide-beam transmissions applied were 0.59 and 0.50. The ratio of average power input (2nd half/1st half) is about 2.

As was usually the case when the instrument pointed toward the northeast limb, additional error in energy input rates is introduced by the uncertainty in determining emission altitudes in the diffuse-auroral regions and in scaling off-meridian brightnesses from equidensity contour plots of all-sky negatives. Furthermore, whenever the major contribution to the total column power input comes from relatively weak, distant regions of particle precipitation with poorly defined boundaries,

accuracy will be further reduced. We estimate the mean error over Scan 99 to be +90%, -60%.

Scan 60S (121.7 km 160.8 - 152.1 sec)

We applied to Scan 60 the volume emission rate profiles derived for Scan 61 (in Ref 3). Two narrow (25 km wide) arcs were south of PKR at  $6^\circ$  and  $20^\circ$  zenith angle, and two broad diffuse regions lay near the southern horizon, at  $65^\circ$  and  $76^\circ$  mean zenith angle (refer to Fig 58 of Ref 6). The narrow-beam 4278 Å photon transmissions to PKR are 0.57, 0.55, 0.26, and 0.12 (in order of increasing zenith angle); we adopted (Ref 4) effective transmissions of 0.65, 0.65, 0.30, and 0.25.

The very bright arc at  $6^\circ$  (70 kR 4278 Å from PKR), which was determined by triangulation to peak at 107 km (5.5 keV,  $3.4 \times 10^4$  photons/cm<sup>3</sup> sec maximum volume emission rate corrected for scattering) dominated the signal. Altitude of peak energy deposition, characteristic incoming-electron energy, and maximum (corrected) 4278 Å volume emission rate for the other three features are 120 km (triangulated) - 2 keV -  $1.1 \times 10^3$  photons/cm<sup>3</sup> sec, 120 km (estimated) - 1.9 keV -  $1.8 \times 10^3$  photons/cm<sup>3</sup> sec, and 120 km (estimated) - 1.9 keV -  $1.9 \times 10^3$  photons/cm<sup>3</sup> sec.

By mid-scan, when the instrument's elevation was  $12^\circ$ , the diffuse region at  $65^\circ$  zenith angle had entered its field. The lower-altitude arc at  $75^\circ$  zenith angle does not come into the field until approximately 0.2 sec before scan end and thus does not contribute significantly to the total energy input rates. These rates (Fig 4), together with those during Scan 61 (Fig 9 of Ref 3), illustrate the change in excitation viewed as the instrument sweeps near-vertically across the series of arc forms. The average input during Scan 60 is about half that in Scan 61, which extends through the atmosphere's limb.

As Scan 60, like Scan 61, is dominated by the near-zenith arc, we again judge the uncertainty in input rates to be due principally to

error in the correction for buildup in this region. The uncertainty should be the same as that for Scan 61, which we estimated (Ref 3) as +50%, -40%.

Scan 111 S (117.5 km, 219.7 - 221.0 sec)

We applied to Scan 111 the volume emission rate profiles derived for Scan 112 (reported in Ref 3). The auroral precipitation distribution was changing rapidly (refer to Fig 58 of Ref 6), and the rocket was penetrating a moderately intense (30 kR 4278 Å from PKR) narrow arc. Two broad (~ 100 km N-S) features south of PKR were also in the instrument's field.

Peak 4278 Å volume emission rates (uncorrected for scattering) in the three regions are  $1.7 \times 10^4$  photons/cm<sup>3</sup> sec (arc at 36° zenith angle north of PKR (1S), 110 km,  $\alpha = 4$  keV);  $5.1 \times 10^3$  photons/cm<sup>3</sup> sec (arc at 12° south (2S), 120 km,  $\alpha = 2$  keV);  $1.2 \times 10^3$  photons/cm<sup>3</sup> sec (arc near 66° south (3S), 122 km,  $\alpha = 1.9$  keV). Each of the particle precipitation regions was assumed to be uniform in the E-W direction, as is qualitatively indicated by the all-sky photograph in Ref 6. Wide-beam transmissions applied were again 0.65, 0.65, and 0.40.

During the first half-scan, which starts at 20.3° elevation, most of the input comes from the nearby bright arc; the high elevation angles result in high intercept altitudes on the distant aurora in the southwest. Near the end of the scan long sight paths develop through the arc 12° south of PKR, so that its contribution becomes about equal to that from Region 1S.

The total column power input in Scan 111 (Fig 4) increases monotonically as the instrument swings downward. During the next spectrum scan (Fig 9 of Ref 3) the column emission rate first continues to increase and peaks near 600 kR 3914 Å, and then drops off rapidly as the instrument's field goes below the maxima in the auroral profiles. Uncertainty in the Scan 111 power inputs is estimated as +75%, -50%.

Scan 136 S (99.1 km, 253.4 - 254.6 sec)

(Corrected results for Scan 137 are given later in this subsection.)

As HIRIS was pointing at relatively high elevation angles ( $27.8^\circ$  to  $15.7^\circ$ ), it views only the nearby ionosphere, where the particle precipitation is weak and diffuse (Fig 5). In the following scan (originally reported in Ref 4) the two discrete, bright arcs near the southern horizon come into the field of view. The two adjoining scans thus provide different conditions of excitation input and altitude for comparison of infrared spectrums.

Volume emission rate profiles for the four particle-precipitation regions in Fig 6 were derived in Section 2 of Ref 4. The effective widths of regions 1S and 2S were determined from the elevation-scanning photometer traces from PKR (Fig 7) and FYU (not shown), and the all-sky photograph from PKR (Fig 5). Measurements taken with the Chatanika radar a few minutes before launch on a diffuse region with surface brightness close to that of 1S (and 2S, which at 8 kR 42.0 is about twice as intense as 1S) led to an estimate of the peak excitation altitude in these areas,  $\sim 135$  km ( $\alpha = 1.4$  keV).

Peak 3914 Å volume emission rates before correction for scattering were determined to be  $2.2 \times 10^3$  photons/cm<sup>3</sup> sec in Region 1S and  $3.3_5 \times 10^3$  photons/cm<sup>3</sup> sec in 2S. We reconstructed the PKR meridian photometer scan from the volume deposition model, which as noted is derived from data from four ground instruments. The results, shown as the solid curve in Fig 7, indicate that the auroral distribution model used to derive column intensities in the projection to the rocket is satisfactorily self-consistent.

Long sight paths through region 1S make it the major contributor to the power input, as Fig 6 shows. The adjustment for scattering by the lower atmosphere was based on a radar-derived equivalent brightness in the northern section of region 1S; it reduces the photometrically-inferred volume emission rates in the diffuse regions by

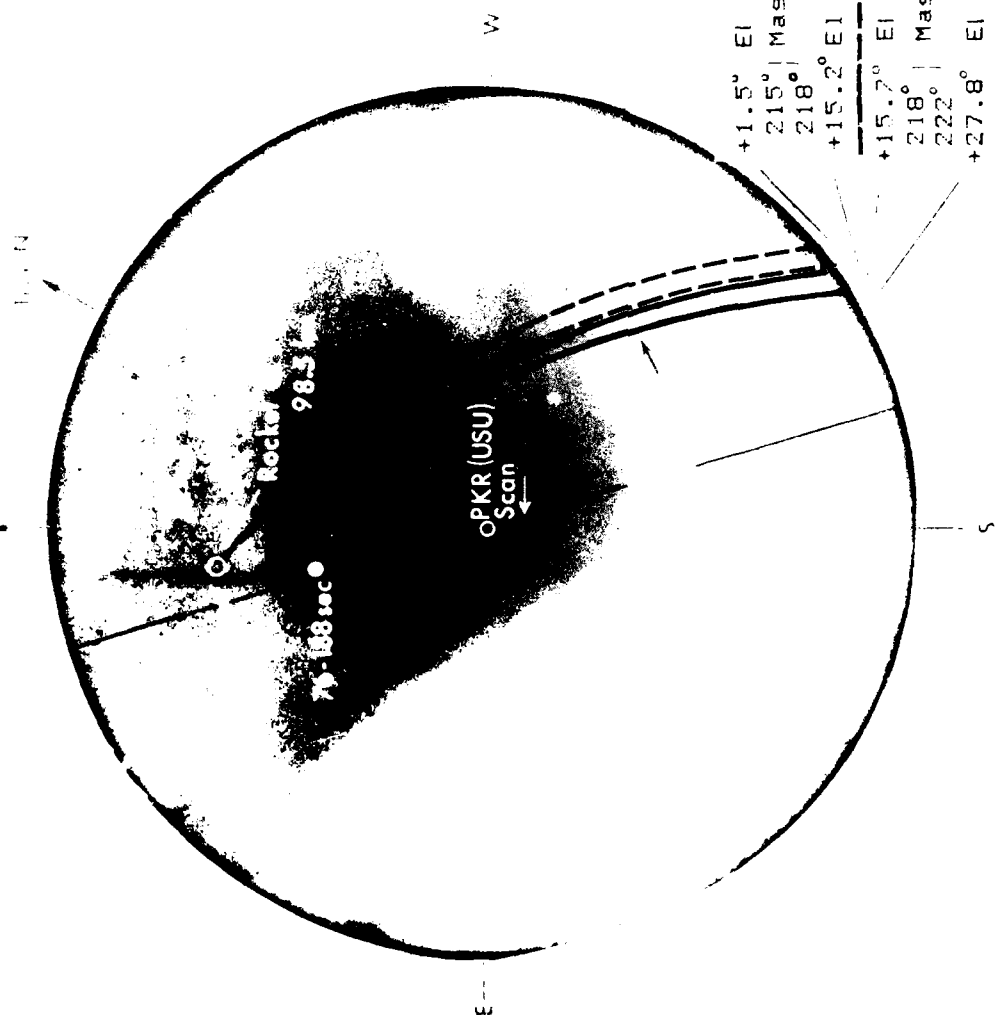


Figure 5. All-sky view from Poker Flat of the distribution of visible air fluorescence between 248 and 253 sec after launch of HRES II. The projection of the optic axis of the spectrometer into the film plane during scans 136 and 137 is shown. Also shown are the pointing directions of the PFR elevation-scanning photometer and the Chatanika radar beam.

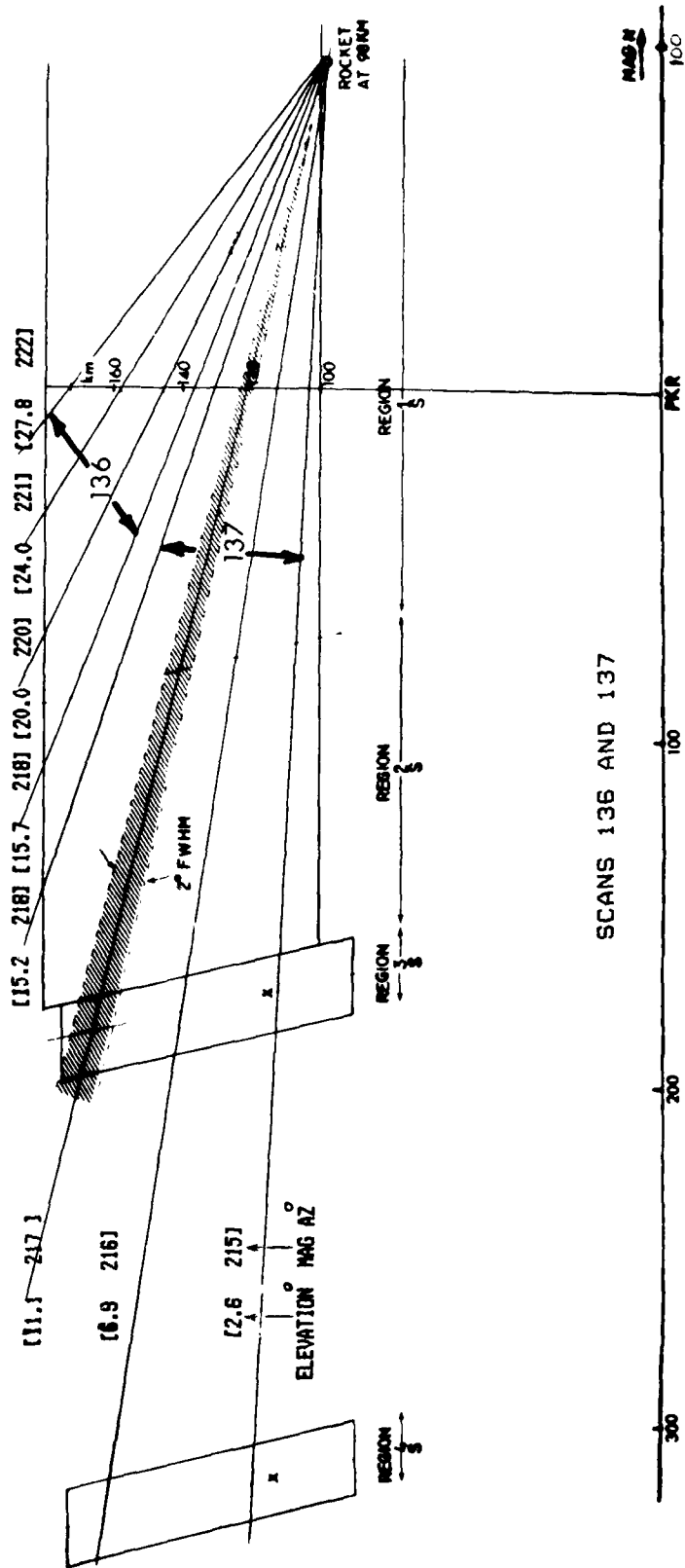


Figure 6. Meridian plane projection of the HIRIS II spectrometer's viewing geometry on the model fluorescing regions during scans 136 and 137. Earth curvature was taken into account in the calculations of column emission rates within the fields.

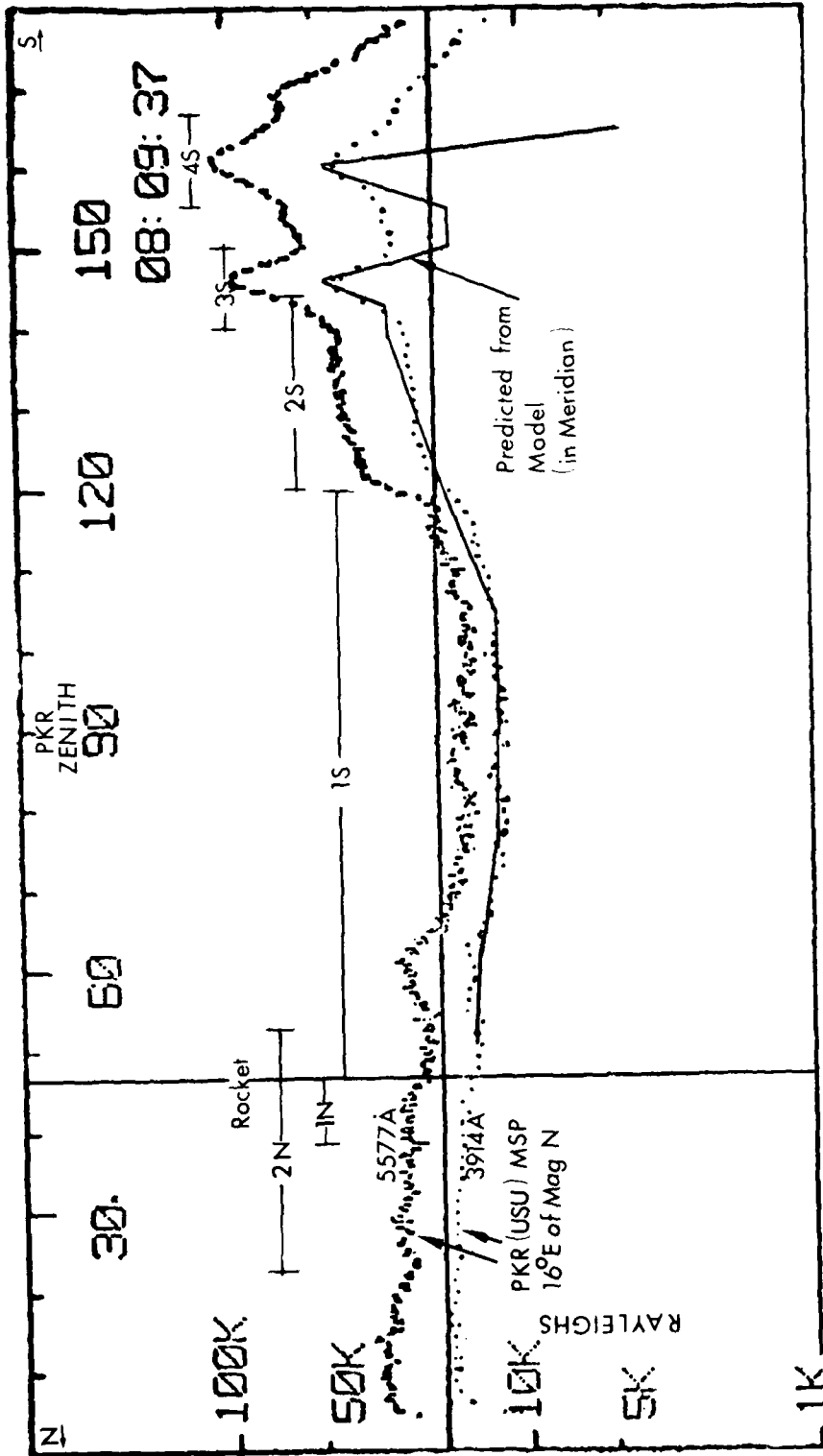


Figure 7. Elevation scan from PKR in a vertical plane  $16^{\circ}$  E of N starting in the north at 257 sec after launch of HIRIS II, with identification of emitting regions. The fit of the model altitude profiles of the system of discrete arcs and diffuse emitting areas (for scans 136 and 137) is indicated by the solid line.

1/3. As would be expected from path-length (van Rhijn gain) considerations, the radiances projected to the rocket instrument are about twice those measured in the zenith by the photometer at PKR.

The average power input downswing during Scans 136 and 137 (Fig 4 and Table 1 ) increases by about a factor 2 per half-scan. Specifically, the mean input goes from 18 kR 3914 Å when HIRIS is pointing above the bright arcs ( at  $\sim 24^\circ$  elevation) to above 100 kR when it points into the main precipitation altitudes (at  $\sim 3^\circ$  elevation). Estimated uncertainty in these values, which is due largely to errors in correcting for buildup, is +50%,- 40%.

Scan 160 S (71.2 km, 285.8 - 287.0 sec)

Most of the aurora continued to move south of PKR in the  $\sim 1$  min preceding Scan 160, leaving only a very broad diffuse glow from  $\sim 30^\circ$  south of the zenith to well north of FYU (Fig 8). The rocket in this low-altitude, downleg scan was 108 km north of PKR, with the instrument axis at  $39^\circ$  to  $28^\circ$  elevation and  $228^\circ$  magnetic azimuth; the sight path thus passes through energy-deposition altitudes northwest of PKR.

The Chatanika radar beam had been repositioned to  $43^\circ$  el,  $15^\circ$  magnetic az after Scan 103 to measure electron density profiles near downleg of the rocket trajectory (see Fig's 1 and 5). It intercepts auroral altitudes some 130 km northeast of the intercept of the rocket instrument's field. The large area of diffuse aurora over PKR appears in the meridian photometer scans and all-sky photographs (Fig 58 of Ref 6 ) to extend far enough northward and eastward to fall within the radar beam. (Note from Fig 1 that the region viewed was closer to the radar's initial pointing direction.)

The volume emission rate profile calculated from the radar data was thus assumed to extend into the instrument field. Peak rate is  $1.5 \times 10^3$  photons/cm<sup>3</sup> sec near 125 km altitude. This calculation is supported by the results of a manual integration of the electron density contours measured near 270 sec; these show an equivalent

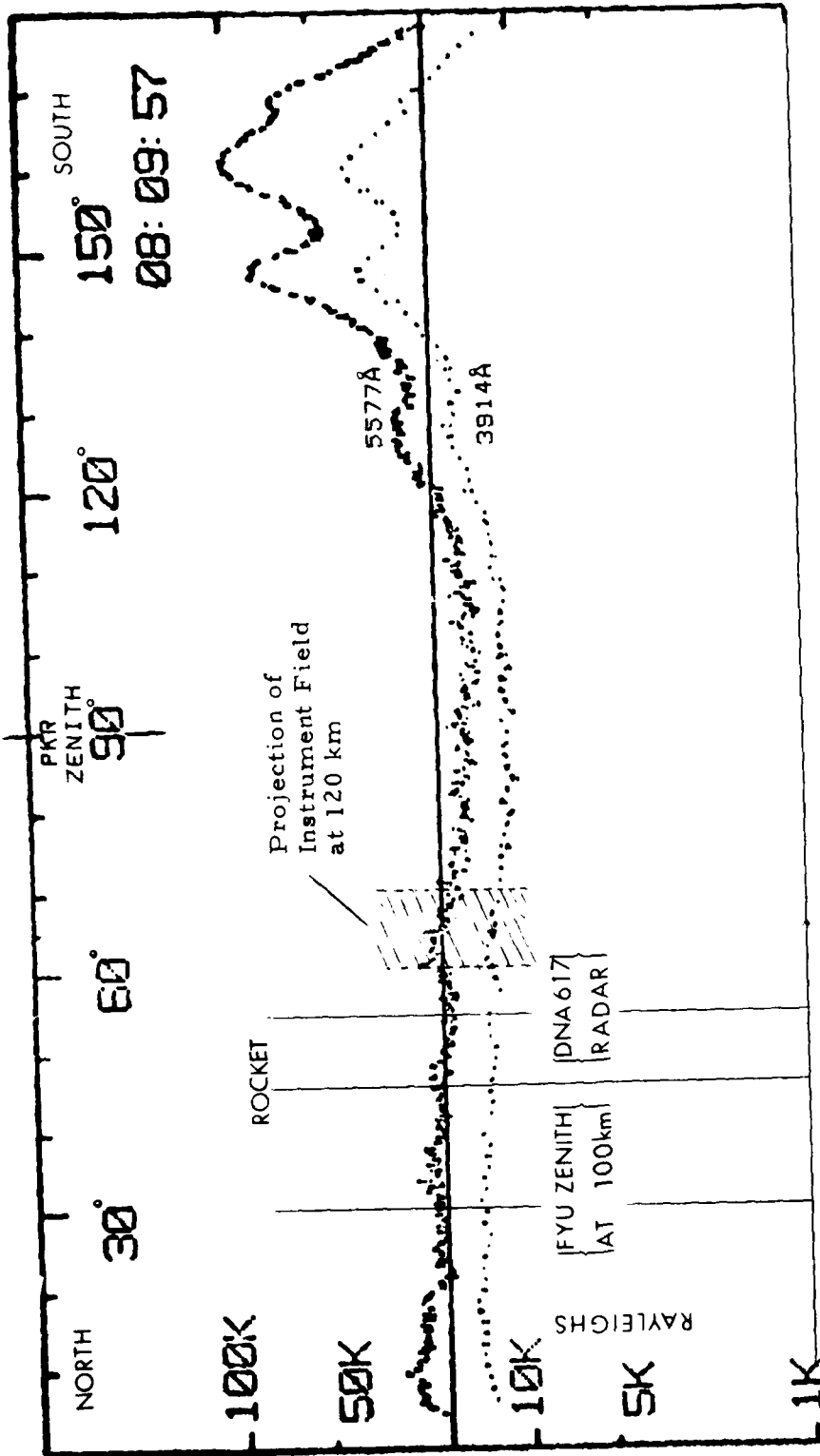


Figure 8. Elevation scans from PKR in a vertical plane  $16^{\circ}$ E of N between 277 and 297 sec after launch of HIRIS II. Projection of the 120 km intercepts of the spectrometer and radar fields and the rocket's location are shown. The spectrometer's field in scan 160 crosses altitudes of maximum particle precipitation northwest of PKR, while the radar's intercept is fixed in the northeast (see Fig 5); thus the fields of the two instruments are separated by a greater distance than would be indicated in this projection.

3914 Å zenith brightness of 10 kR, which is somewhat less than the 12 kR near-zenith intensity from PKR measured photometrically (Fig 8).

The energy input rate (Fig 4) is "flat" and comparatively low over the scan interval, as would be expected from the viewing geometry. Average power input increases by less than 15% between the two half-scans. The mean figure of 28 kR (3914 Å) at the instrument's  $\sim 34^\circ$  elevation is somewhat lower than what would be expected from the  $\sim 14$  kR (uncorrected) at  $65^\circ$  *el* measured from PKR (Fig 8), because as noted above, energy input rates were derived from the radar data. Uncertainty in the uniformity of the diffuse glow within  $45^\circ$  of the zenith contributes to the error, which we estimate as +60%, -40%.

#### Scan 137

In our initial assessment of energy deposition rates during this scan (Ref 4), we compared the optical brightness in the northern section of diffuse region 1S (see Fig's 6 and 7) with an equivalent column emission rate derived from the incoherent-scatter radar data. As the radar results indicated that 1/3 of the measured photons coming from the direction of 1S were inscattered, we assumed that 1/3 of the photons appearing to originate from diffuse region 2S were also inscattered. (That is, we in effect normalized the scanning photometry results to the single-point radar profile.) Due to a transcription error, however, we reduced the contributions at the rocket from these two glow regions by 2/3 rather than 1/3. Additionally we made a small further underestimate of the column integral by omitting a section of region 1S between PKR zenith and the rocket.

The corrected power inputs for Scan 137 are included in Fig 4 and Table 1. During the first half-scan they are about twice those reported earlier (Fig 11 of Ref 4), as the volume emission rates assigned to nearby regions 1S and 2S are doubled. In the second half-scan, when the distant bright arcs 3S and 4S make the major input (see Fig 6), the change is small. At the mid-scan point the input rate is increased from 40 to 64 kR.

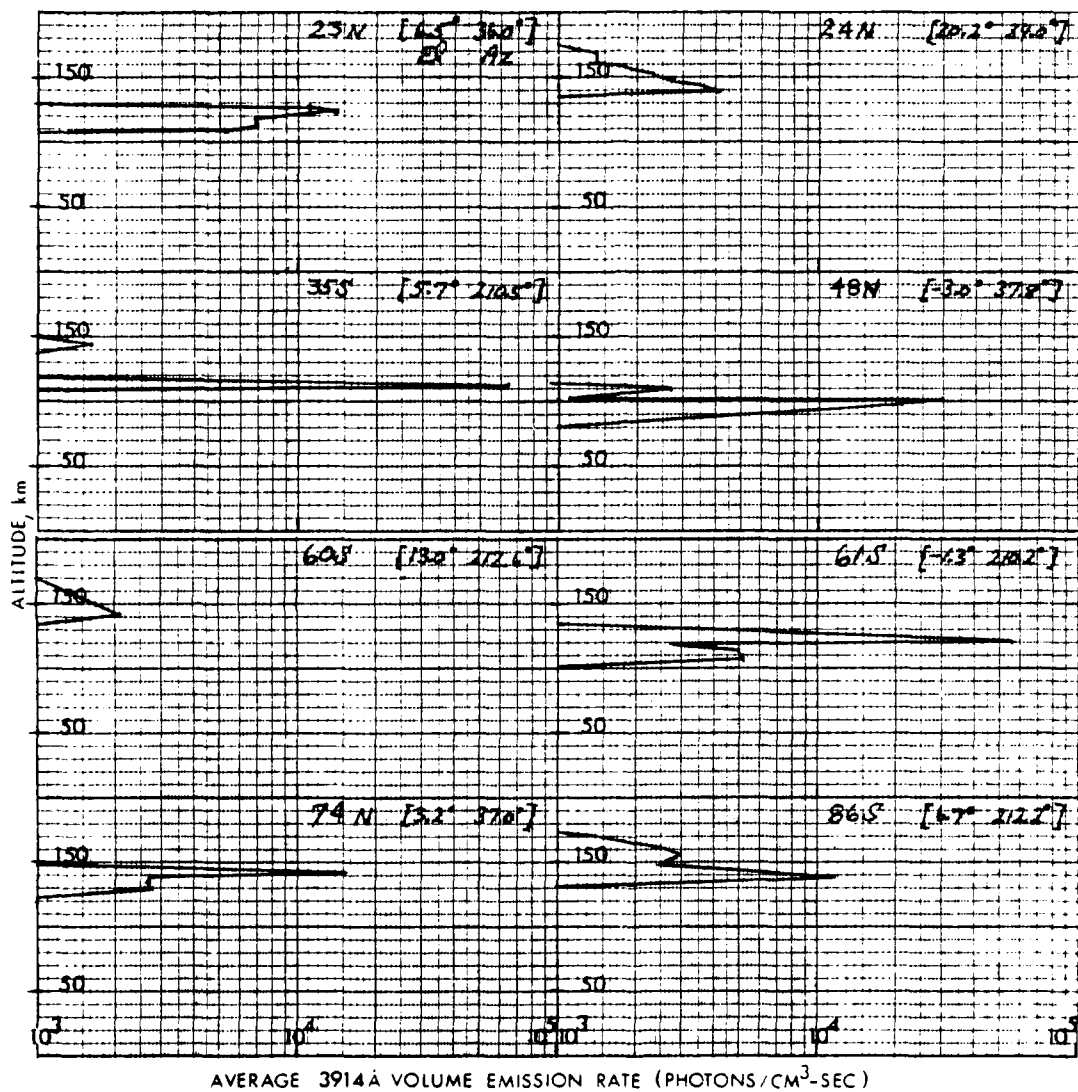
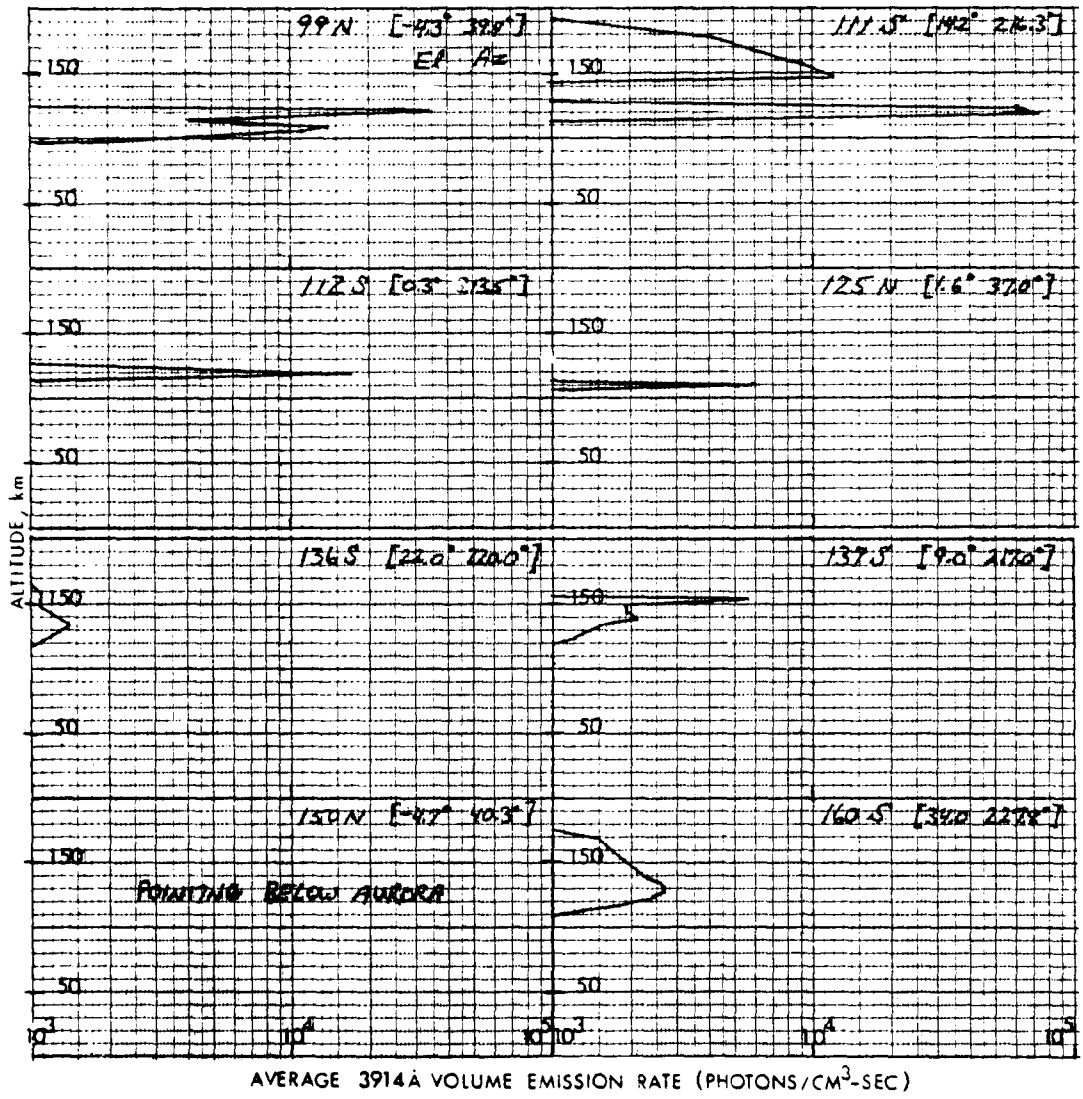


Figure 9 . Altitude profiles of 3914 Å volume emission rate in HIRIS's field at the midpoint of each spectral scan. The data represent averages over 5 km altitude intervals.



## ALTITUDES OF ENERGY DEPOSITION

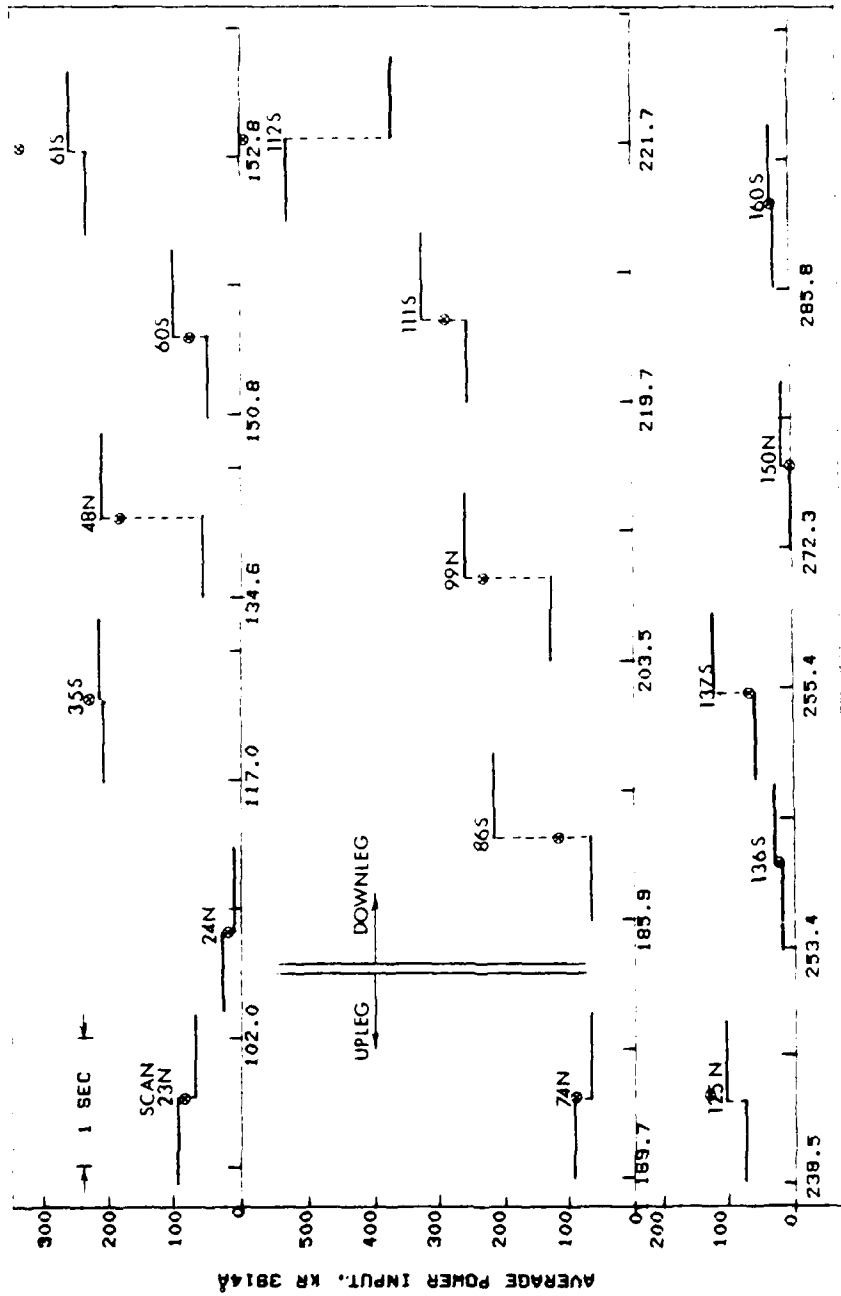
Altitude profiles of the volume emission rate along the line of sight at mid-point of each interferometer mirror scan are shown in Fig 9. These were derived from the model plots of deposition distribution, examples of which are Fig's 3 and 6. The volume emission rates have been averaged over 5 km vertical cells. They are intended to provide a relative rather than absolute measure of the input rate from column segments at each altitude along the sight path, as the total radiance depends also on instrument elevation angle (that is, path length) through 5-km altitude "slices."

These altitude profiles refer to the HIRIS's band-integrated spectral intensities, which as we noted previously are proportional to their interferogram's intensity component at mid-scan. Other profiles could of course be readily generated for other mirror positions, and averaged over half or full spectrum scans.

(It should be pointed out that the profiles in Fig 9 refer to relative particle energy deposition rates as indicated by volume emission rates in  $N_2$  fluorescence bands. They have not been weighted by the altitude profile of yield of  $N^2D$  atoms per photon, or probability that  $N^2D$  reacts with  $O_2$  to produce  $NO(v)$  (rather than quenching on O).)

### SUMMARY

Column emission rates within HIRIS II's field calculated here for the seven further spectrums (and corrected Scan 137) are in Fig 4. Fig 10 and Table 1 summarize the column power inputs averaged over half-scans and when the interferometer mirror was at its midpoint for the 16 instrument viewing aspects illustrated in Fig 1. Altitude profiles of excitation rate at mid-scan, calculated to help assess the effects of atmospheric species concentrations and temperature on yield of  $NO$  vibrational fundamental-band photons, are plotted in Fig 9.



TIME AFTER LAUNCH, SEC

Figure 10. Mean power input within HIRE II's field during half-scans and at the mid-point of the interferometer excursion (⊗) in each of the sixteen scans reduced. N indicates a scan of the north-east aurora (as in Fig 3), S a scan southwest (as in Fig 6).

Consecutive scan pairs 23 - 24, 60 - 61, 111 - 112, and 136 - 137 provide  $\sim 30^\circ$  elevation "sweeps" from near co-altitude across the particle energy deposition regions, and as expected show the substantial variation in column excitation rate along the instrument's sight path. As the same input data are applied to each member of a pair, their relative accuracies of column excitation would be expected to be better than the absolute accuracies that we have estimated for individual scans.

In this regard, the narrow range of efficiencies for excitation of NO fundamental-band radiation by the  $N^2D + O_2$  reaction measured by HIRIS (Ref 8) suggests that the set of power inputs that we have calculated is reasonably self-consistent. These "fluorescence" yields are also subject to random error from the uncertainty in the absolute infrared spectral distribution, over and above the possible systematic error in the interferometer's calibration.

As we have noted, effective energy deposition altitudes could be determined in future HIRIS-like surveys of the spectral emission of air irradiated by naturally-occurring charged particles, by relatively straightforward filter photometry to measure rotational temperatures in a band of the  $N_2^+$  First Negative system.

## SECTION 2

### SPATIAL DISTRIBUTION OF ENERGY DEPOSITION BY EXCEDE: SPECTRAL'S ELECTRONS

#### BACKGROUND

PhotoMetrics, Inc., designed and built a radiometrically-calibrated photographic system for the EXCEDE: Spectral rocket (Ref's 14, 15), whose function was to assess the magnitude and uniformity of energy deposition within the spectroradiometers' fields of view and to provide information about the behavior of the planned 3 kV, 32 A ejected electron beams and the resulting atmospheric-ionization conditions. We succeeded in obtaining the first photographic images from onboard of artificial aurora excited by a rocketborne electron accelerator, and furthermore the film data are of very high quality. In this Section we describe the camera system and determine from these data the spatial distribution of column energy input near the payload at one upleg and one downleg altitude.

A detailed engineering description of the two coaligned wide angle cameras, their exposure controller, and the method for identifying frames from the telemetry record is in Ref 14. System specifications are summarized in Table 2. The camera system was first flown as part of EXCEDE: Spectral (alternatively called EXCEDE II) payload EX851.44-1, on 29 Oct 78 (Ref 16). As an exterior protective cover failed to open after launch, none of the IR/optical instruments were able to take data on the atmospheric glows excited by the electron beams. The recovered film and the telemetry record from EX851.44-1 showed (Ref 17) that the camera system had operated as planned during the rocket flight.

The cameras were re-installed in a second Talos Castor sounding rocket (A51.970), which was flown successfully from Poker Flat Research Range on 19 Oct 79 (Ref's 2, 18). Both the black-and-white and color camera again functioned as planned, and returned extremely

Table 2. Summary of specifications of EXCEDE photographic system

Cameras:	Two 16 mm Photo-Sonics 1VN, pin-registered with magazine load
Film:	125 ft, double perforated, 0.004 in Estar base, spooled to Kodak Specification 430
Lens:	5.7 mm fl, f/1.8 (on optic axis), T/2.2 at 4000 Å
* Field of view:	62° x 94° on 16 mm film frame (7.6 x 12.1 mm image)
Emulsion types:	Kodak 2475 (monochrome) and Kodak EF 7241 (color)
Optical filters	For 2475: - Schott BG-12 FWHM 3450 Å - 4650 Å For 7241: - none (quartz window)
Intervalometer:	One controlling each camera, independently programmed: see Ref 14
Exposure cycle:	3 x 0.008 sec, 4 x 0.078 sec, 1 x 0.80 sec; total duration 1.75 sec nominal
Frame identification:	By correlation with electron gun pulses
Start time:	84 sec after rocket launch, 78 km

---

\* Refer to Fig 12 for pointing.

high signal/noise, onscale images of the air fluorescence over the full altitude range 116 km (accelerators turn on) - 128 km (apogee) - 72 km (accelerator module separation). The black-and-white film, for example, has some 270 useful frames. Although the camera bodies and film magazines were irreparably damaged in the hard landing of the payload, fortunately only some extreme edges of the film rolls and frames outside the data-image area were fogged by leakage light. Fig 11 shows a series of typical photographs of the radiance distributions, taken by the monochrome camera. The viewing geometry for these projections is illustrated in Fig 12.

#### INSTRUMENTATION

We include here a brief description of the camera system as background for the following data assessment (see also Table 2 ).

The monochrome camera is filtered so that it measures principally the electron impact-excited radiations from  $N_2$  molecules at wavelengths between  $\sim 3800 \text{ \AA}$  (where the lens transmission begins to decrease sharply) and  $4600 \text{ \AA}$ . Most of the signal is due to the familiar  $N_2^+$  First Negative  $3914 \text{ \AA}$  (0, 0) and  $4278 \text{ \AA}$  (0, 1) bands. In high-altitude air excited by electrons of energy  $\gtrsim 0.1 \text{ keV}$  - which includes most of the auroral-particle spectrum, beams from EXCEDE: Spectral and similar active probes, and the beta rays and Compton secondaries of gamma rays emitted from nuclear explosions - and their accompanying secondary electrons, about a third of all the emitted photons within the panchromatic-photographic emulsion wavelength range (3800 - 6800  $\text{\AA}$ ) are in these two features. Weaker bands of the  $N_2$  Second Positive system, excited principally (if not wholly) by secondary or knock-on and degraded-primary electrons, also contribute to the signal (refer, for example, to p 28 of Ref 18). Delayed radiation from metastable states, principally the  $O^1S - ^1D$  transition at  $5577 \text{ \AA}$  (about half the photographically-actinic photons are emitted in this line under steady-state particle excitation of air above 100 km), would "smear" the intensity distri-

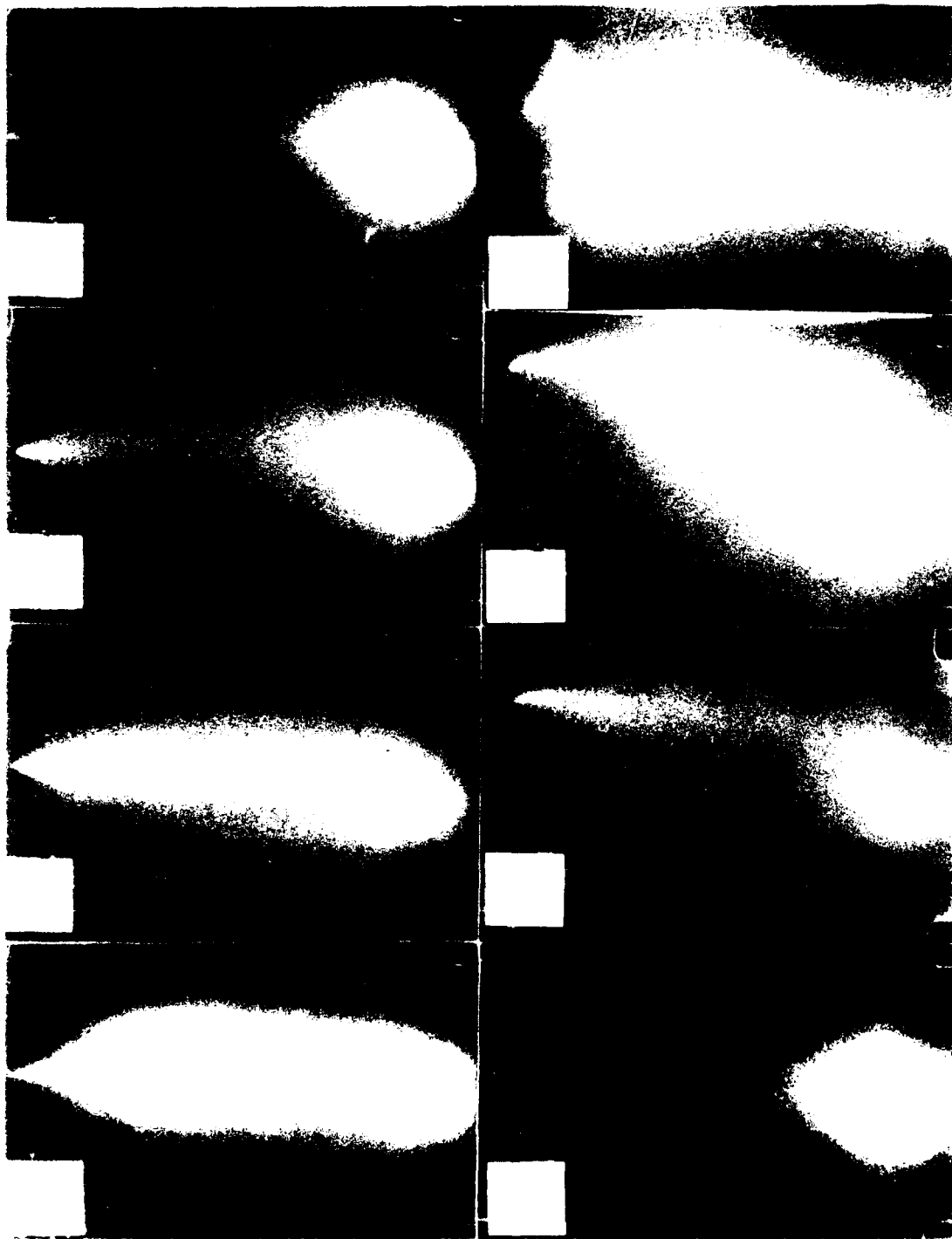


Figure 11. Typical photographs from orbit of the air fluorescence excited by EXCEDE. Spectral's electron accelerators in upleg and downleg. The radiance distributions projected to the camera differ from the true density distributions, as explained in the text.

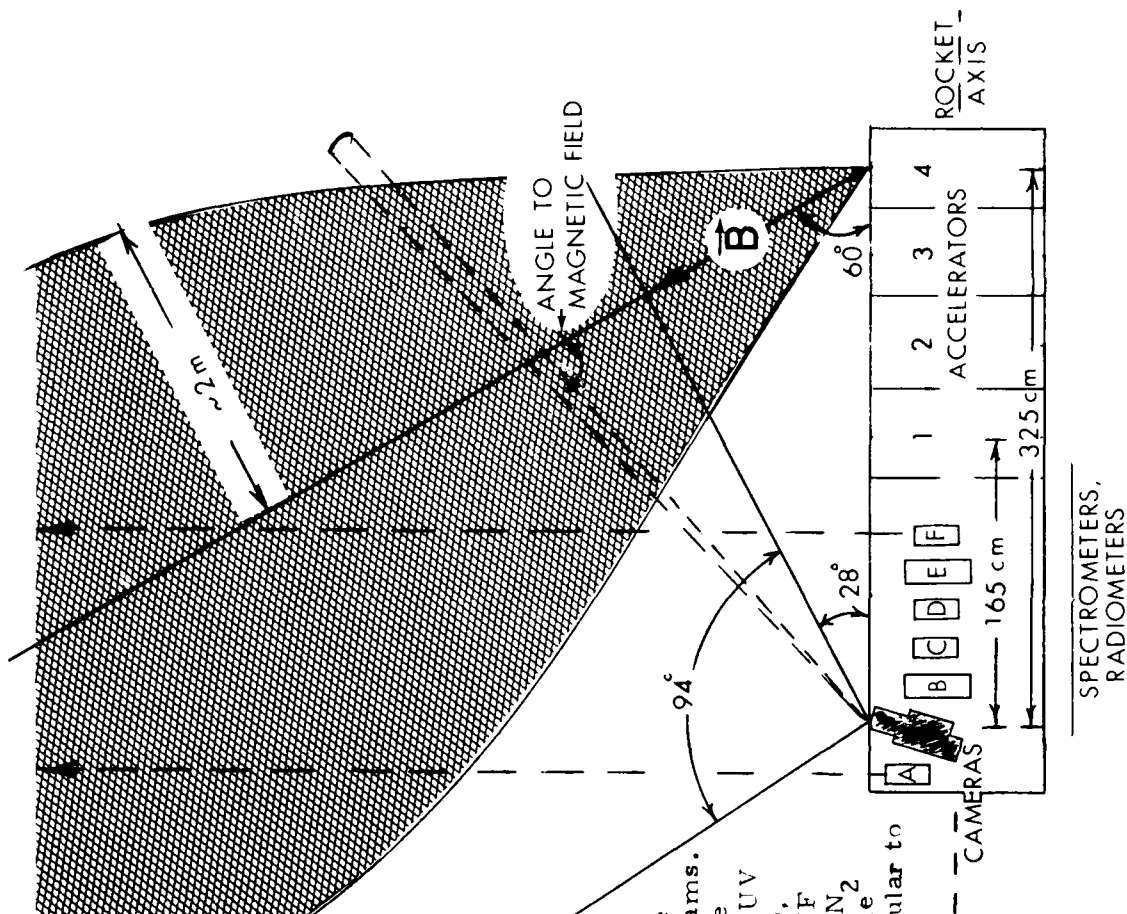


Figure 12.

Side view of the camera fields and the region of atmosphere into which electrons from EXCEDE: Spectral accelerator #4 deposit energy. The plane defined by the optic axes of the two onboard cameras is offset 13 cm (out of the page) from the plane containing the axes of the electron beams. The optic axes of the two cameras are separated by 8 cm horizontally. The UV diodes (A), CVF-He spectrometer (B), radiometers and photometers (C), CVF spectrometer and photometers (D), LN<sub>2</sub> interferometer (E), and UV and visible spectrometers (F) all point perpendicular to the rocket's long axis.

bution in the vicinity of the moving rocket, which advances its own length in about 1 millisecond. Fig 13 shows the spectral sensitivity of this camera (taking into account lens transmission) and the wavelengths of the major contributors to irradiance at its film plane. Eastman Kodak 2475 film has moderately high granularity and nominal exposure index 1250 developed to contrast  $\gamma = 1$  when its full spectral range is used; the manufacturer's data in Fig 13 are a more appropriate measure of its sensitivity in scientific applications (this proved to be lower in the actual calibration). Forced development to increase film speed is not indicated, as it reduces the dynamic range of scene brightness that can be recorded.

The other camera uses three-color film, principally to assess the contribution to scene radiance from the laterally-ejected secondary electrons and also to increase dynamic range (exposure index is 160 under normal development). The less-energetic secondaries selectively excite triplet-manifold transitions in  $N_2$ , to produce First Positive bands in the red and near IR and Second Positive bands in the blue-violet and near UV, along with other  $N_2$  triplet sequence features outside the photographic sensitivity range. The color positives (not reproduced here) indeed show the expected magenta (blue + red) glow surrounding a white (which is overexposed blue) "core" along the beam trajectory, just as do photographs of kilovolt electron beams fired into air in laboratory tanks. (Some of the primary electrons also are Coulomb-scattered across the magnetic field lines (Ref 19).) Spectral sensitivity of this camera is essentially that of the three layers of its Eastman Kodak EF 7241 film, which is similar to daylight sensitivity Ektachrome.

Alternate short and long exposures were made to keep on-scale the extremely broad range of maximum brightness of the beam-induced glows and the wide dynamic range of brightness expected within each scene. Peak radiance (in the absence of collective-interaction or discharge effects) is roughly proportional to the atmosphere's density, which changes by almost four orders of magnitude between

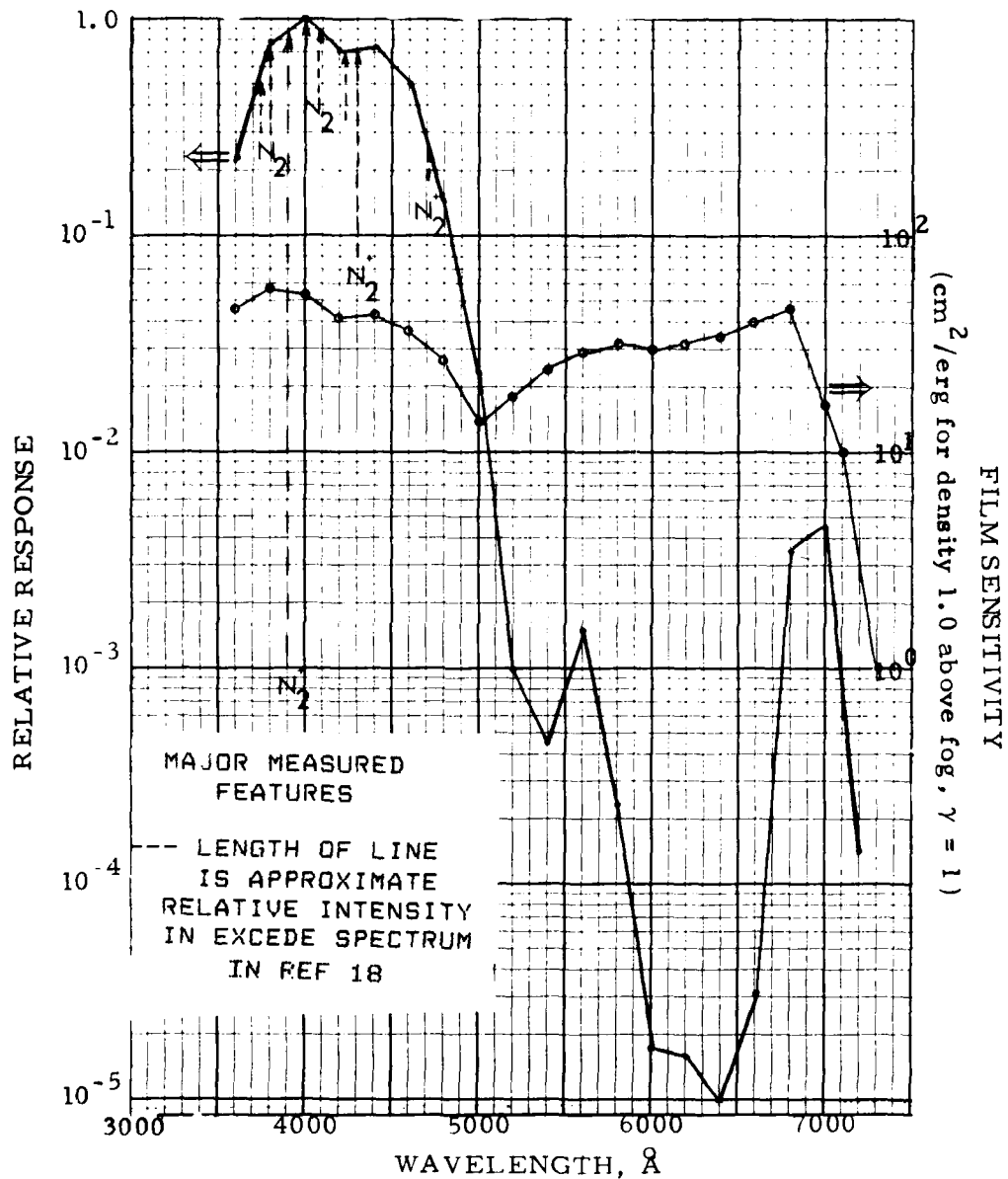


Figure 13. Relative spectral response of the monochrome (EK 2475 film) photometric camera with 5.7 mm f/1.8 lens. The sharp falloff above 4600 Å results from the attenuation by its 1½ mm thick BG-12 Schott filter. Response at wavelengths below 3900 Å is limited by lens absorption and at wavelengths beyond 7000 Å by the falloff of the film's sensitivity (circles).

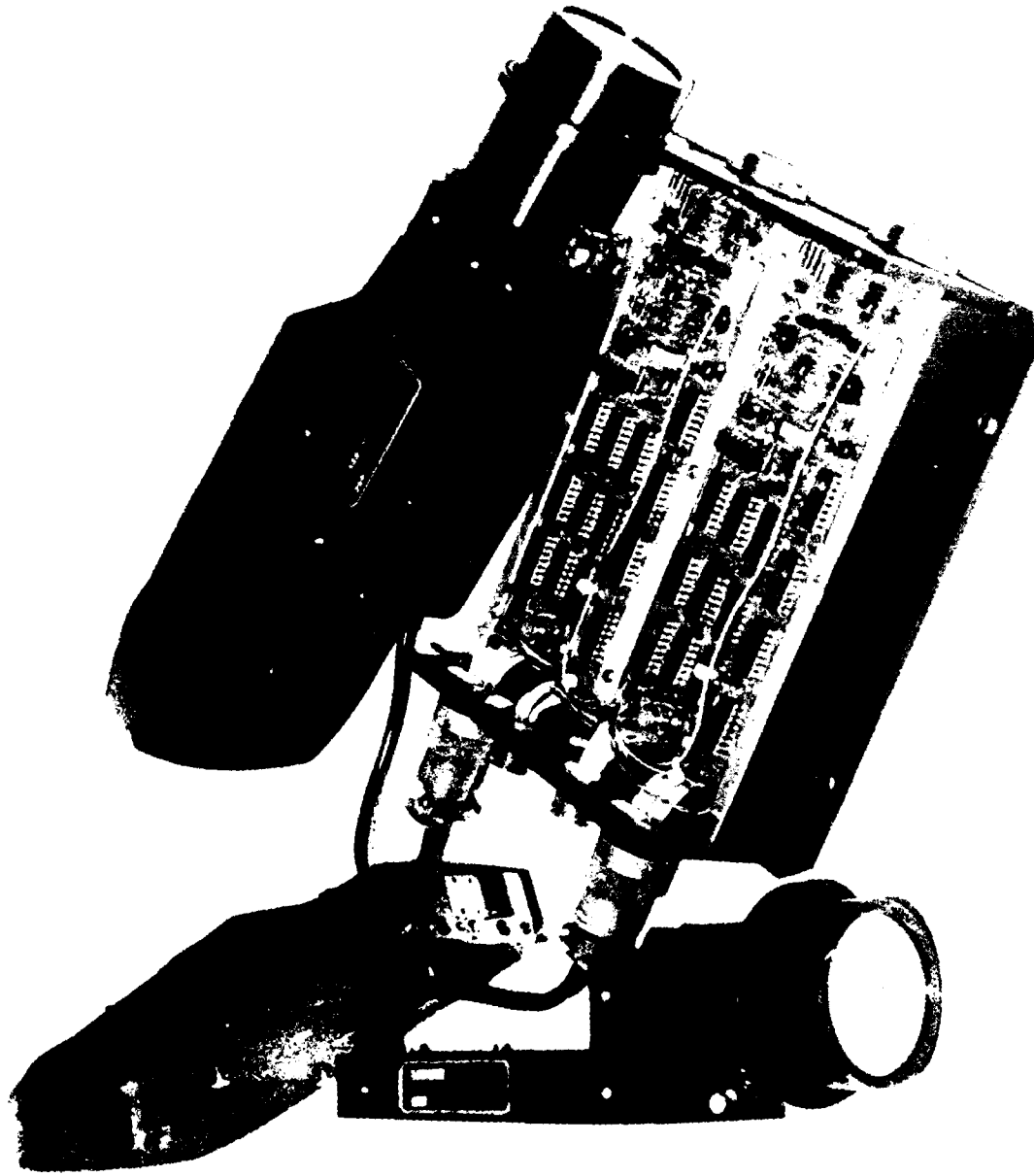


Figure 14. View of the intervalometer assembly (center, with cover removed to show the circuit boards) and two 16 mm cameras. The shutter movement sensor, used to control the camera motor and provide a signal for the telemetry of film advance, is just to the left of each lens. The film magazine has been separated from the left camera.

apogee and the lowest altitude at which the electron accelerators were in operation. The minimum exposure is limited to 8 millisecond by the design of the camera's rotating-blade shutter, and the maximum exposure to 8/10 sec by the desired time resolution of the photographic measurements (the electron beam pulses are 4 sec long).

To ensure redundancy in case of failure the two cameras are controlled by separate circuits, the only shared elements being a 28-volt power supply and the signal from the rocket's programmer that initiates exposure sequencing. We installed shutter movement sensors (consisting of a light-emitting diode and photocell) whose output is multiplexed onto a telemetry channel at a sampling rate of 16/sec to indicate the starting time of each exposure. Wide angle lenses cover as much of the glow as practical (refer to Fig 12); the camera's angular resolution, which is determined primarily by the granularity of the fast photographic emulsions, is about  $10^{-2}$  radians. A view of the two cameras with their dual intervalometer-controller is in Fig 14.

#### CALIBRATIONS

Radiometric sensitivity of the films used in the actual rocket measurements was determined by exposing the same emulsion number film in a 21-step sensitometer having a 2900 K (tungsten continuum) lamp. The step-wedge areas were then as usual developed along with the data films, that is, under identical agitation conditions. Calibration exposures were made through Schott BG-12 (see Table 2) and  $\sim 10 \text{ \AA}$  FWHM filters, for times close to those of the field exposures (1.0 sec, 0.064 sec, and for the faster monochrome film 0.012 sec) to minimize any effects of film reciprocity failure. Filtering was as follows (the wavelengths are at the filter peaks):

<u>EK 2475 (B&amp;W)</u>	<u>EK 7241 (color)</u>
No filter (tungsten)	No filter (tungsten)
BG-12	3914 Å
3914 Å	4278 Å
4278 Å	4700 Å
5577 Å (low transmission by BG-12)	5577 Å 6086 Å 6315 Å .

The exposures through filters in the right-hand column serve to calibrate the color film's three layers. As data from this roll have not yet been reduced, the discussion following refers only to the black-and-white photographic emulsion.

As we have noted, photons with wavelengths just shortward of 3914 and 4278 Å (the First Negative bands are shaded to the violet) make the major contribution to the image of the primary ejected-electron beam on this film. This is shown by EXCEDE: Spectral's visible light-sensitive spectrometer, which as Fig 12 shows views through the beam and necessarily also detects radiation excited by secondary electrons scattered outside the "core." As expected, the published spectrum (p 28 of Ref 18) has N<sub>2</sub> Second Positive bands near 3750, 3805, 3998, and 4060 Å along with strong N<sub>2</sub><sup>+</sup> First Negative (0, 0) and (0, 1) and  $\Delta v = 0, -1, \text{ and } -2$  sequence bands with heads at 3884, 4236, 4652, and 4709 Å.

Fig 13 shows that the response of the camera is reasonably flat over this range of wavelengths. Weighting the spectral irradiance from fluorescence of air at E-region altitudes, we find that the effective wavelength of exposure is about 4000 Å in the "core", and where the color film is magenta it is about 3900 Å. Since the camera's sensitivity differs by 12% between these two wavelengths (Fig 13), even if there is excess Second Positive band emission from the core (on which more presently) the radiometric calibration is changed only negligibly. We chose to use the calibration with BG-12,

whose effective wavelength is  $\sim 4450 \text{ \AA}$ , as the sensitometric exposures through this wider filter resulted in a useful range of developed film densities at all exposure times; thus no correction for reciprocity failure is needed. We applied a correction of 25% for the difference between effective spectral sensitivities of the film at  $4550 \text{ \AA}$  and the camera at  $4000 \text{ \AA}$ . (The extra effort to apply a further 12% radiance correction to the area of image outside the core was not considered justified.)

We measured the diffuse density interval of the nominally-neutral step tablet for the appropriate spectral illumination of the sensitometer with BG-12 filter using two different instruments, each with tungsten lamp and S-11 photocathode. The data show no variation from an average of  $\sqrt{2}$  per step - the expected value - up to step 10 (tablet attenuation 32, optical density  $10 \times 0.15 = 1.5$ ). Above step 10, the average increase in density appears to be 0.16 per step; however, the laboratory data are noisy because the BG-12 filter itself has the high effective density of 1.5 in the optical system of the densitometers, and the increase could be due to nonlinearity in their logarithmic amplifiers. Since the maximum cumulative inaccuracy resulting from such a variation in the step tablet would be about 25% in the regions of lowest exposure on the negative, we did not consider this correction further. This potential inaccuracy does not apply to areas of the images in which the film's optical density is greater than 1.5; it increases gradually to the maximum stated possible error toward fog density (that is, where the scene radiances are very low).

Vignetting and distortion of the wide-angle lens at full  $f/1.8$  aperture, as used in the measurements, are shown in Fig 15. Vignetting, or decrease of image-plane illumination away from the optic axis, is a property of all (moderate-distortion) wide-angle lenses having high axial numerical aperture. It was measured by photographing a diffusing screen illuminated to uniform radiance by a tungsten lamp and measuring the density and exposure distributions on the radiometrically-calibrated film frame with a two-dimensional scanning

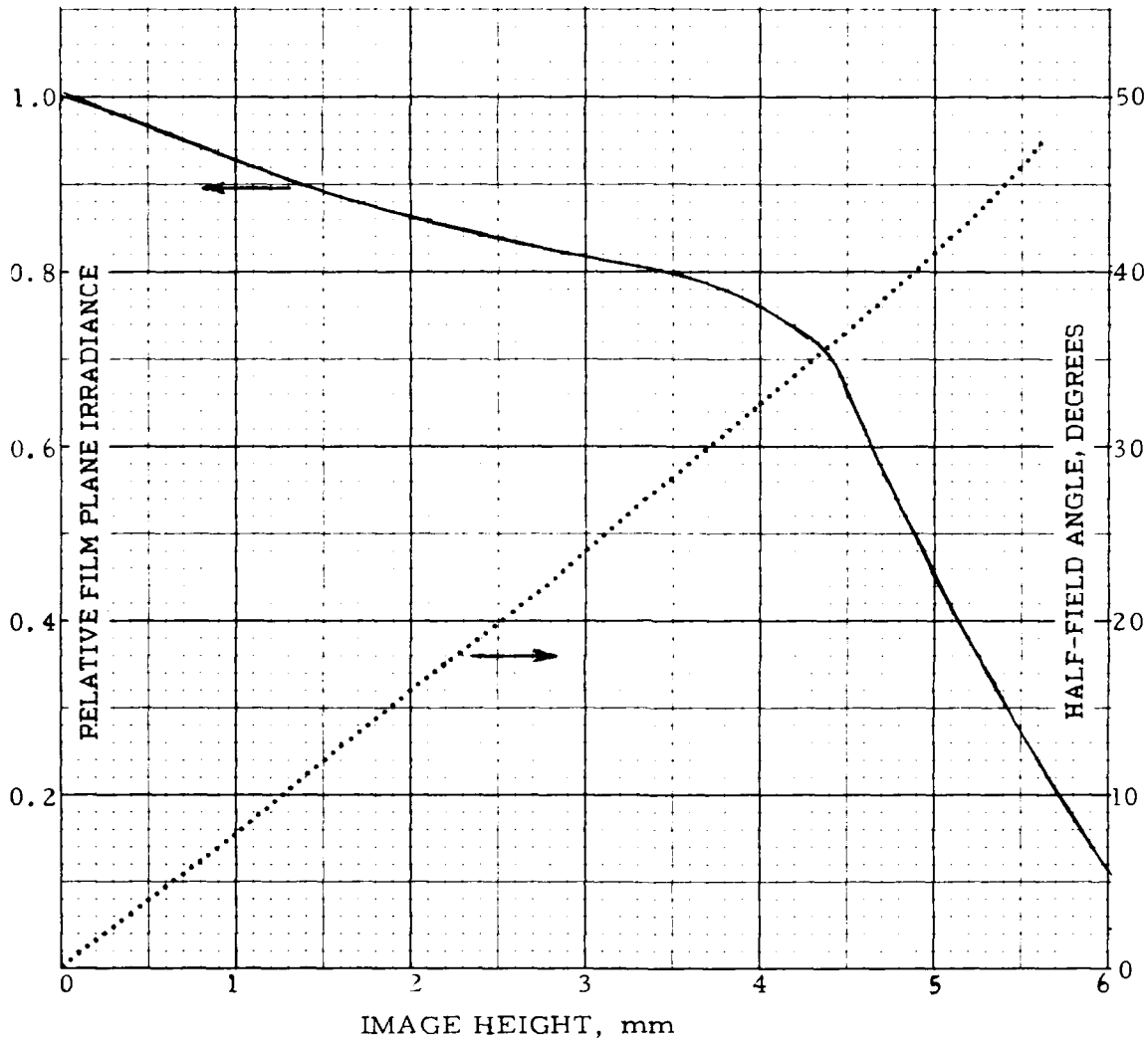


Figure 15. Relative irradiance in the image plane (solid line) and field-of-view half-angle (dotted line) as a function of displacement of the image point from the center of the camera field. These measurements of the vignetting and distortion of the camera lens were used in converting the film density distributions to radiance distributions.

microdensitometer (to produce an equi-density contour plot of the type shown in Fig 17). The break near  $35^\circ$  from the axis is thought to be due to partial obscuration of the exit pupil by a stop within the lens. Transmission of the lens on axis at  $4000 \text{ \AA}$  is given in the manufacturer's literature as 0.62 (its maximum value is 0.81 at  $5000 \text{ \AA}$ ). It should be noted that the large correction for the decrease in aperture ratio toward the edge of the field changes qualitatively the scene surface radiance distributions indicated in Fig 11.

Distortion, or failure of objects at angle  $\Theta$  from the optic axis to image at angle  $\Theta$ , is also a property of otherwise-corrected wide angle lenses. It was measured by photographing a rectangular scene of known dimensions (a large optical target-resolution test chart). The distortion, which we corrected in the final data reduction, has only a small effect on the qualitative "look" of the film density distributions in Fig 11.

#### GEOMETRY OF VIEWING

These representative prints from the film negative illustrate typical intrascene density distributions, and are not intended to reproduce faithfully differences in air fluorescence brightness at the various rocket altitudes. The exit ports of the electron accelerators are about  $1\frac{1}{2}$  meters below the bottom of each frame (see Fig 12).

As these images are not the familiar far-field, "stand-off" views - in contrast to the images from a ground station shown in Ref 18 (pp 53-55) - some interpretation of the viewing geometry is necessary. The irradiances at the film plane are as usual two-dimensional projections to the onboard camera lens of three-dimensional volume emission distributions. Refer, for example, to the column in Fig 12 extending from the lens across the axis of the beam from accelerator #4, which we have taken to lie along the direction of the geomagnetic field. Fig 16 shows the distance from (the anode of) accelerator #4 to the intercept of this column on the beam axis as a function of vertical position on the film and angle to the field line.

Note that the view of the electron impact-excited air volume becomes increasingly foreshortened toward the top of the frame, a perspective effect similar to looking down railroad tracks. The reason for the re-brightenings toward the top in Fig 11 is that the sight path (or column length) through the optically-thin glows is increasing more rapidly with intercept distance than the emission rate per unit volume is decreasing. Plots similar to Fig 10 apply to the other three electron accelerators and to currents from more than one accelerator.

#### APPLICATION OF THE RADIANCE DATA

At altitudes where the electron trajectories are controlled by geomagnetic ( $e\vec{v} \times \vec{B}$ ) forces rather than multiple Coulomb scattering, beams ejected with axis parallel to the magnetic field expand out to the Larmor radius of those electrons that have the highest perpendicular velocity component, and then refocus at a mean distance (parallel velocity)/(cyclotron frequency Be/m). The transition altitude is about 90 km for 3 keV electrons, this radius is just under 1 meter when the beam is initially in a cone of  $15^\circ$  half-angle, and the refocusing distance over PKR is 21 m. The horizontal dimensions on the film of cylinders of  $\frac{1}{2}$  to 30 m radius are shown in Fig 16 (the geometric projection again refers to accelerator #4 only).

The ionization rates within the shaded volume in Fig 12 are to a fair-to-good approximation the product (electron current density) x (atmospheric molecule + atom density) x (mean cross-section of these particles for ionization by 3 keV electrons). A distribution in space of energy deposition that takes into account collisional scattering of primary electrons across the field lines, the changing interaction cross-sections as they slow down, and the contribution of secondaries and the backward-scattered component is given by the transport model of Ref 20. This model is applicable principally between ~92 and 110 km altitude, above which its assumption of an unbounded transport medium overestimates the deposition rates (as an increasing fraction of the primary electrons escapes to the conjugate hemisphere).

3

The projections to the onboard cameras serve to check on the model of volume energy deposition. Where the "core" is nearby cylindrical - as Fig 12 indicates, above about the center of the film frame - the length of the emitting column passing through its axis is proportional to the cosecant of the angle between the two direction vectors. Since in the approximate model the current density is  $\sim$ constant within the field-aligned cylinder, the surface brightness per unit path length would be the volume emission rate along the intercept line. Similarly, in the conical region surface brightness viewed perpendicular to the axis would be expected to vary inversely with the distance to the anode, as the sight path is proportional to this distance and the electron current density is proportional to (distance)<sup>-2</sup>. As the deposition pattern has no preferred direction about the magnetic field vector, it is essentially cylindrically symmetric and lends itself to unfolding by standard means. The volume emission rates so derived from the surface brightness can then be summed to determine energy deposition rates in the fields of view of individual spectroradiometers in the payload, locations of which are shown in Fig 12.

#### PRELIMINARY OVERVIEW OF THE FILM DATA

The electron impact-excitation models of course assume the absence of collective or beam-instability phenomena such as beam-plasma discharge (Ref's 21, 22) or formation of plasma sheaths about the rocket (Ref 23), or other emission such as air fluorescence excited in return current paths physically separated from the outgoing electron beam (Ref 23). Such phenomena would compromise the accuracy of the energy-input data, as the ratio of (volume production rate of N<sub>2</sub><sup>+</sup> First Negative Band photons)/(sum of all ionizations and molecule dissociations) starts to decrease at electron energies  $\lesssim$  40 eV and obviously becomes zero below the 18.7 eV threshold. That is to say, soft plasma electrons would deposit more energy than indicated by the column intensity in the measured fluorescence bands.

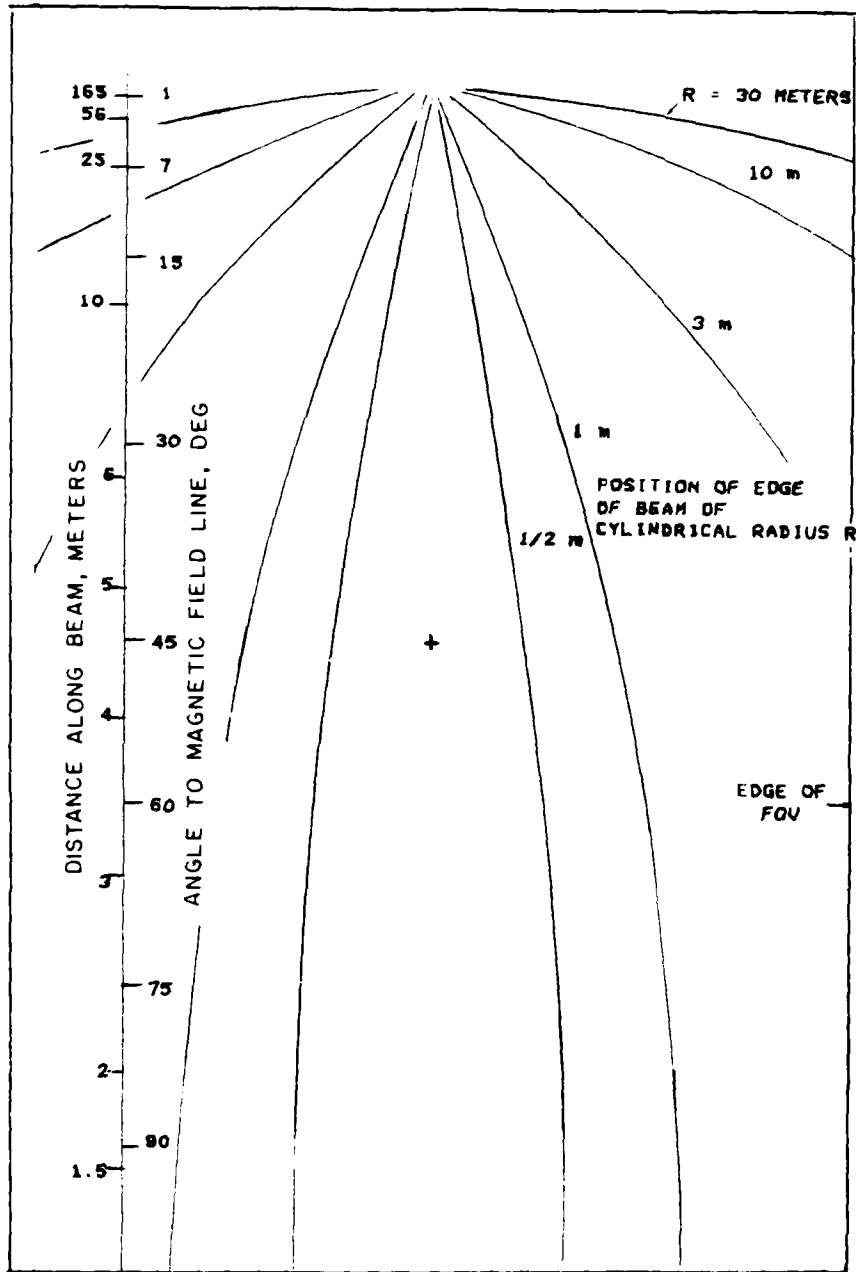


Figure 16. Plot for relating positions on uncorrected (for lens distortion) equidensity contour plots such as Fig 17 to distances in object space. This geometry refers only to ejection of electrons from accelerator #4 along the magnetic field lines, and the plane defined by the beam axis and camera optic axis. The curved lines indicate the distance scale perpendicular to the beam axis in this plane. The angle to the magnetic field is as shown in Fig 12.

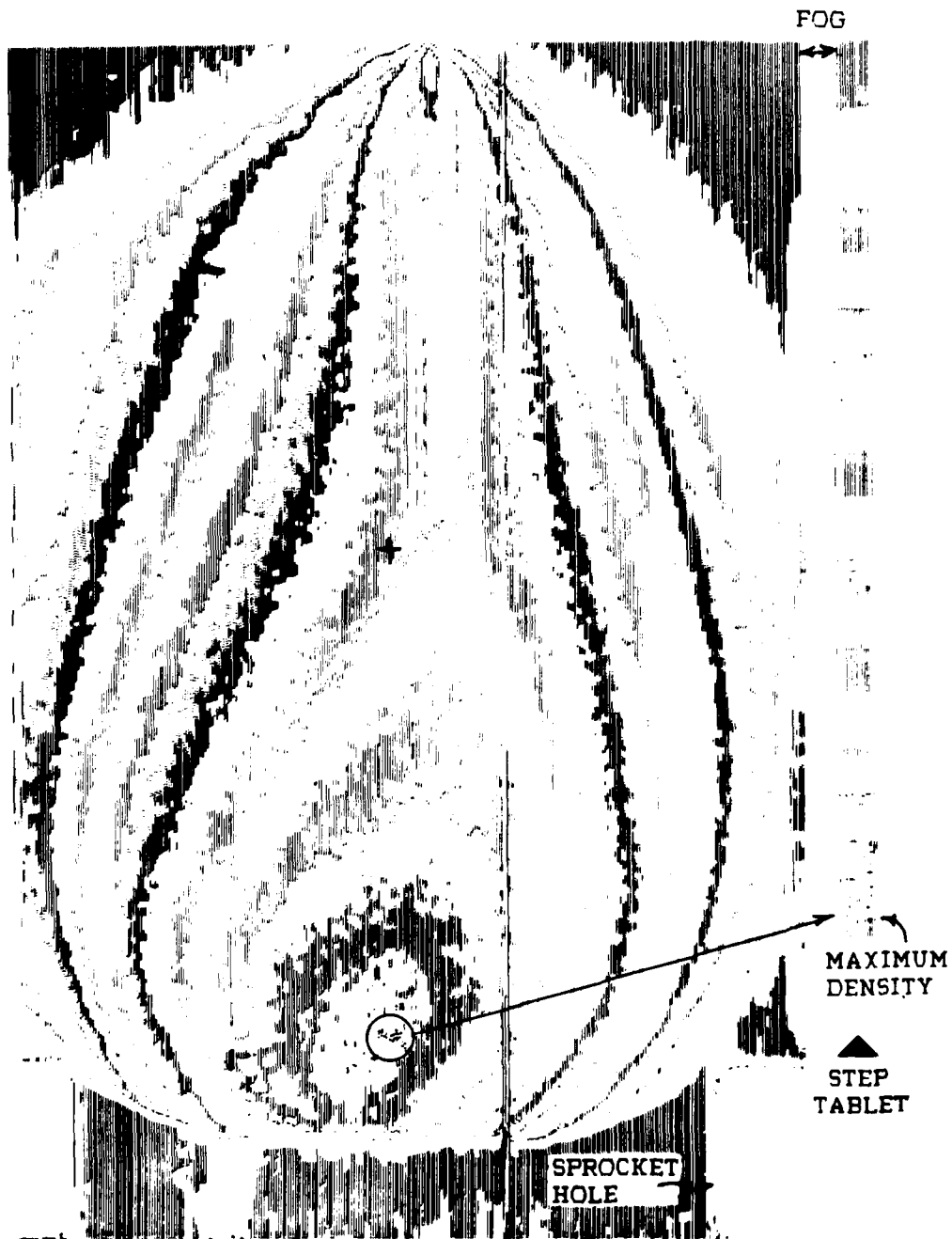


Figure 17. Equi-density contour plot from 0.08 sec exposure at 123 km upleg, EXCEDE: Spectral. The ejected electron current from accelerator #4 (in Fig 12) is 7 amperes. (Same scale as Fig 16.)

A qualitative examination of the films shows no obvious such effects: the density distributions appear to indicate a "smooth" flow from the accelerators. Quantitative analysis of the brightness distributions, on the other hand, shows a considerable departure from predicted behavior, whose implications are discussed in later subsections.

The "radius" of the beam appears from the negatives (before correction for lens vignetting) to be of the order of magnitude expected. In any case, laterally-scattered secondary electrons broaden the energy deposition pattern, as is clear from the color photographs. The beam's increased slope to the right on downleg is believed due to the changed azimuth of the payload's long axis, which was rotated  $20^{\circ}$  under ground control (Ref 18) to give the infrared spectroradiometers a longer sight path through previously-dosed air (that is, to permit viewing afterglows along the rocket trajectory). This maneuver, which moves the direction of the injected beam's axis  $5^{\circ}$  away from the magnetic field vector, was necessary because the rocket's trajectory plane was not in the geomagnetic meridian as planned.

The frame at 109 km on upleg is an 0.8 sec exposure during which a very short pulse of electrons was emitted from the accelerators before they began their normal operation. Two bright spots near the center of this image, thought to be pieces of payload hardware, were also seen by the rocket's video camera (Ref 18). (The video data, which suffer from severe saturation difficulties, and which in any case are not radiometrically calibrated, are interpreted as suggesting some disordering of the velocity distribution of the air fluorescence-exciting electrons.) "Color" and position of these artefacts can be determined from the film data. The remaining frames in Fig 11 are 78 millisecc exposures; the electron beam comes from accelerator #4 only in all except those at 266 and 288 sec. Some structure, which changes in frames 0.01 sec apart, appears in the glow volumes between 99 and 80 km on downleg; this effect has not yet been investigated. The glow still shows some symmetry about the field direction at altitudes as low as 80 km.

## METHOD OF FILM DATA ACCESS

Most of the steps in determining surface radiance distributions from the negatives are standard and have been applied by PhotoMetrics in earlier radiometric-photography efforts (Ref's 24 , 25 ). Since a relatively small number of frames were to be quantified, this initial data reduction was done manually.

The film had been processed by hand in a reel tank using agitation known to give uniform development. Contrast gamma resulting from 8 min in DK 50 at 20°C (68°F) was 0.55 in the step tablet exposed through the BG-12 filter, from which is constructed the density vs log exposure (H&D) characteristic. Both the image area and this calibration tablet are scanned with an "Isodensitracer"<sup>R</sup> to produce an equi-density contour plot such as shown in Fig 17. The contours are then related to steps on the tablet, and each contour of developed density is assigned a film-plane exposure from the H&D transfer curve.

This exposure distribution is then manually converted to a relative scene radiance distribution using the lens-vignetting characteristic in Fig 15. Sufficient spatial resolution is achieved by re-transcribing about 150 exposure points in the two-dimensional grid. The region toward the edge of the camera field is re-contoured to correct for lens distortion, to make displacements from the image center proportional to angles from the optic axis in object space.

The contours are then assigned absolute radiance values applying the sensitometer's known (from past calibrations) spectral irradiance, the BG-12 filter's transmission (manufacturer's specification), and the lens' aperture ratio on axis corrected for transmission at 4000 Å (manufacturer's specification). As noted, a correction was made for the difference in the film's sensitivity to the radiations from the sensitometer and the high-altitude air excited by EXCEDE: Spectral's ejected electrons. Fig's 18 and 19, contour plots of radiance projected to the camera, are examples of results of the procedure.

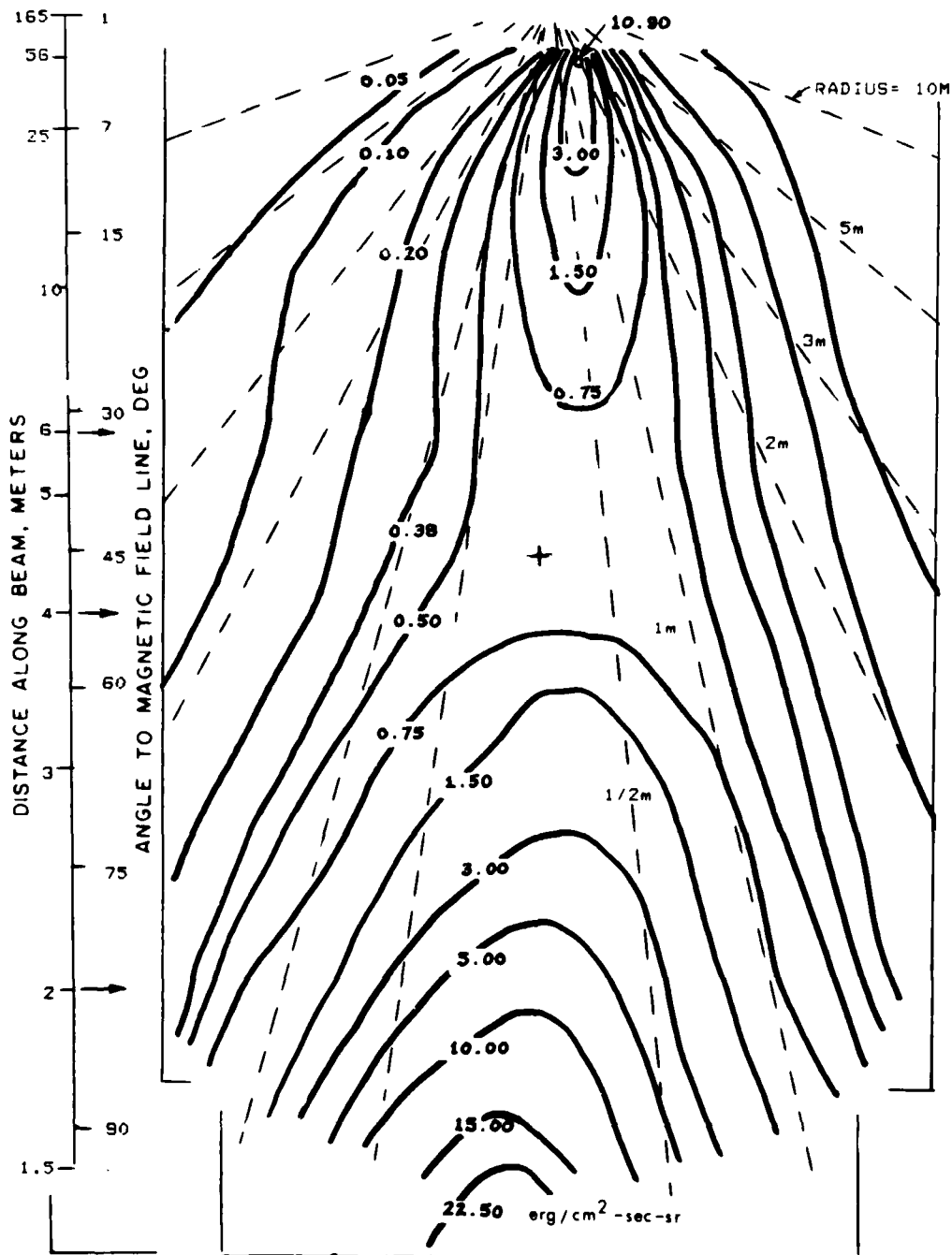


Figure 18. Radiance distribution projected to the onboard camera when EXCEDE: Spectral is at 123 km upleg. The original optical density distribution on the film (Fig 17, same scale) has been converted to scene brightness after correction for the camera lens's vignetting and distortion. 1  $\text{erg/cm}^2 \text{-sec-sr}$  is equivalent to  $2\frac{1}{2}$  megarayleighs at 4000 Å.

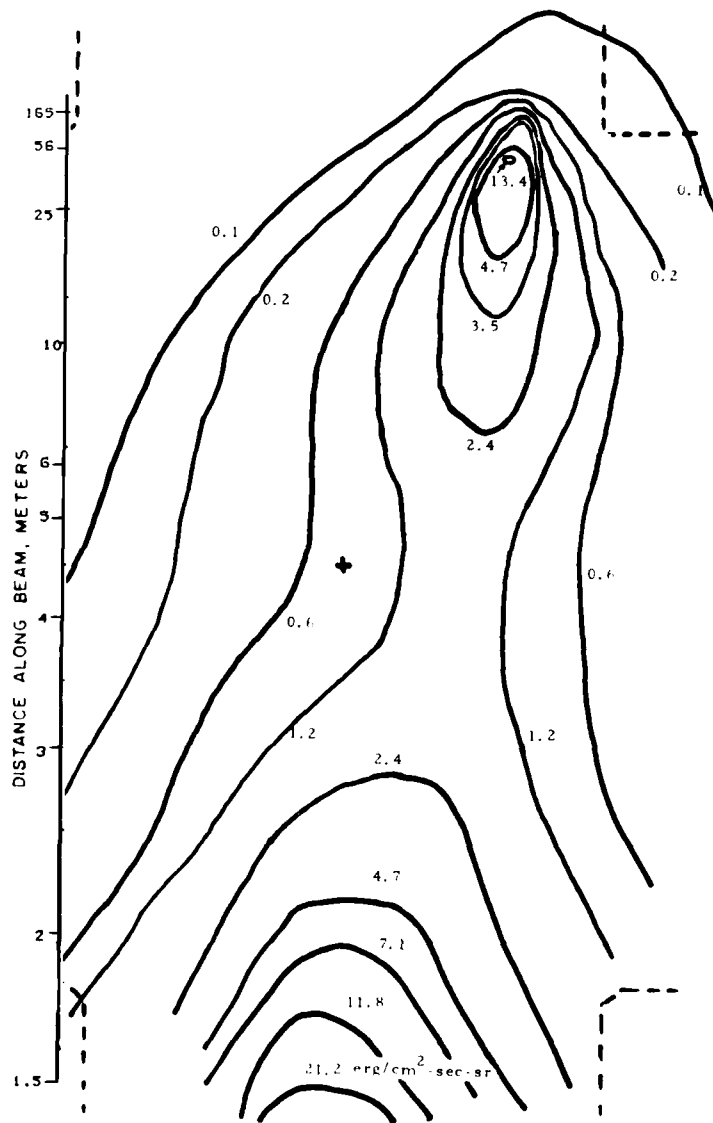


Figure 19. Radiance distribution projected to the onboard camera at 113 km on downleg (244 sec). Electron accelerators #3 and #4 were ejecting electrons at an angle of  $4.7^\circ$  to the field lines. The electron current may have shut off toward the end of the 0.090-sec exposure (see text).

The major errors in calibration are expected to come from the aforementioned uncertainty in the step tablet's attenuation in its high-density range, and in the correction for vignetting, which becomes increasingly large toward the top and bottom of the film area. The film's variable sensitivity with wavelength leads to only a small potential error, since most of the actinic radiation is known to lie in a narrow band (as Fig 13 shows). Reliability of calibration would be improved by a measurement of the lens optical transmission and vignetting to 4000 Å light, a re-check of the BG-12 filter material used, and an independent determination of the film's spectral sensitivity (rolls with the original emulsion number have been saved). A source of error independent of the calibration is the light scattered within the camera's wide-angle lens and body, whose effect on the apparent radiance signal is greatest at the lowest film densities; this flare light has not been quantified. With the effort so far spent on calibration, the mean estimated error in scene radiance is +60%, -40% in the center of the film frames, increasing to +100%, -50% near the corners.

#### GLOW RADIANCE DISTRIBUTIONS AND DIMENSIONS

Two film frames reduced to radiance "maps" are in Fig's 18 and 19, and Fig 17 is the equi-film density plot that served as the basis for Fig 18. The brightness distributions have sufficient axial symmetry to allow volume emission rates to be unfolded. For reference, a scene radiance of 1 erg/cm<sup>2</sup> sec ster is equivalent to 2½ Megarayleighs of ~4000 Å radiation.

The 3 MR measured at 113 km on downleg by the 3914 Å photometer (p 160 of Ref 18), which points into the glow near the center of the camera's field at a different projection angle, is closely consistent with the midfield radiance in Fig 19. These photometer data show a decrease with altitude at a generally lower rate than the atmosphere's density, which indicates that the total neutral-particle density within instrument fields is to some extent altered by outgassing from the

rocket body. (Compare Ref's 26 and 27, which show fluorescence signals proportional to ambient  $N_2$  density up to ~130 km (Polar 5) and 200 km (Echo 1) respectively.)

Attention is directed to a major qualitative difference between the equi-radiance plots and the original negatives or their equi-density plots. After correction for lens vignetting, the radiance contour lines are open in the bottom half of the frame; they would close at angular positions outside the camera's field of view. In the negatives, in contrast, vignetting makes them appear to close at the extremities of the field.

The basis for selection of these two frames for an initial film data assessment is as follows. On upleg a 7 ampere electron beam from accelerator #4 is ejected very close to the field direction, making the air fluorescence pattern almost symmetric about a vertical axis; this symmetry facilitates test of energy-deposition models. The exposures on the 78-millisecond frame at 123 km altitude are "on-scale," so that this single image has a very wide range (factor  $10^3$ ) of artificial-auroral scene brightnesses. This range can be extended downward by reducing the nearby 800-millisecond exposure; and brightness resolution in the most dense regions (in the "core") can be improved by reducing the 8 millisecond exposures (in which the film contrast is greater at high exposures). As noted, flare light in the cameras is an additive factor that has the effect of increasing exposure from directions of weak atmospheric emission; thus the minimum radiances in Figs 18 and 19 are most likely upper limits.

The exposure at 113 km on downleg (244 sec after launch) meets the criteria 1) the altitude is within the expected range of validity of Ref 20's model of energy deposition and 2) good-quality ground imagery, which provides a second projection of the fluorescence, is available. As these photographs (p43 ff of Ref 18) are taken with a manually-tracked camera with  $10^0$  field, only a few of the ~3 sec exposures are free of visually-detectable image jitter. The images from the ground station have insufficient spatial resolution to provide information about the energy deposition distribution transverse to the beam's axis, but give good information about the brightness of the volume along its long dimensions (when the beam penetrates a few 10's m). Images from the

close-in onboard camera have good longitudinal resolution within about 15 m from the electron accelerators, where the infrared instruments view excited air (refer to Fig's 12 and 16), and they of course also provide high-resolution data on the radiance distribution transverse to the direction of beam ejection.

A longitudinal and transverse cuts across the glow at 123 km are re-plotted in Fig's 20 and 21. The radiance viewing transverse to the "core" axis, determined by correcting the radiances projected to the camera for the increased sight path that results from the acute angle of view, is nearly constant beyond ~4 meters; this finding indicates that the electron beam has become cylindrical. Extrapolation to zero brightness of the straight sections of the transverse radiance plots (three of which are shown in Fig 21) indicates that this cylinder's radius becomes somewhat greater than 2 meters. The effective half angle of the initial radiation cone is thus  $30^\circ$ , rather than the  $15^\circ$  of the ejected electron beam (as had been previously measured in the laboratory).

The brightness at high altitudes (see also Fig 22) increases much more rapidly toward the accelerator anode than the  $(\text{distance})^{-1}$  predicted by the aforementioned first-approximation conical-expansion model. The calculated values in Fig 20 assume the 7 amps ejected is confined in a  $15^\circ$  half angle cone to 4 m from the anode with uniform current density, after which the beam becomes cylindrical;  $3 \times 10^{11}$   $\text{N}_2$  molecules/ $\text{cm}^3$  at 123 km; and a  $3 \times 10^{-18}$   $\text{cm}^2$  cross-section for excitation of 3914 Å-band radiation. We increased the initially-calculated radiances by 50% to take into account excitation by secondary electrons and the other air fluorescence bands in Fig 13. Preliminary results from the electron transport calculation with the assumption of an initially-parallel beam (Ref 28) are included in Fig 20.

These film data show considerably more radiation than predicted from the region within a few meters of the beam's ejection into the atmosphere, toward which the onboard spectroradiometers are pointing. Beyond this distance, the "shape" of the axial brightness distribution is about as expected from both energy-deposition models; indeed, if the cylinder's radius were 1 meter rather than the 2+ meters measured from the films, its axial brightness viewed from the camera would fit the models.

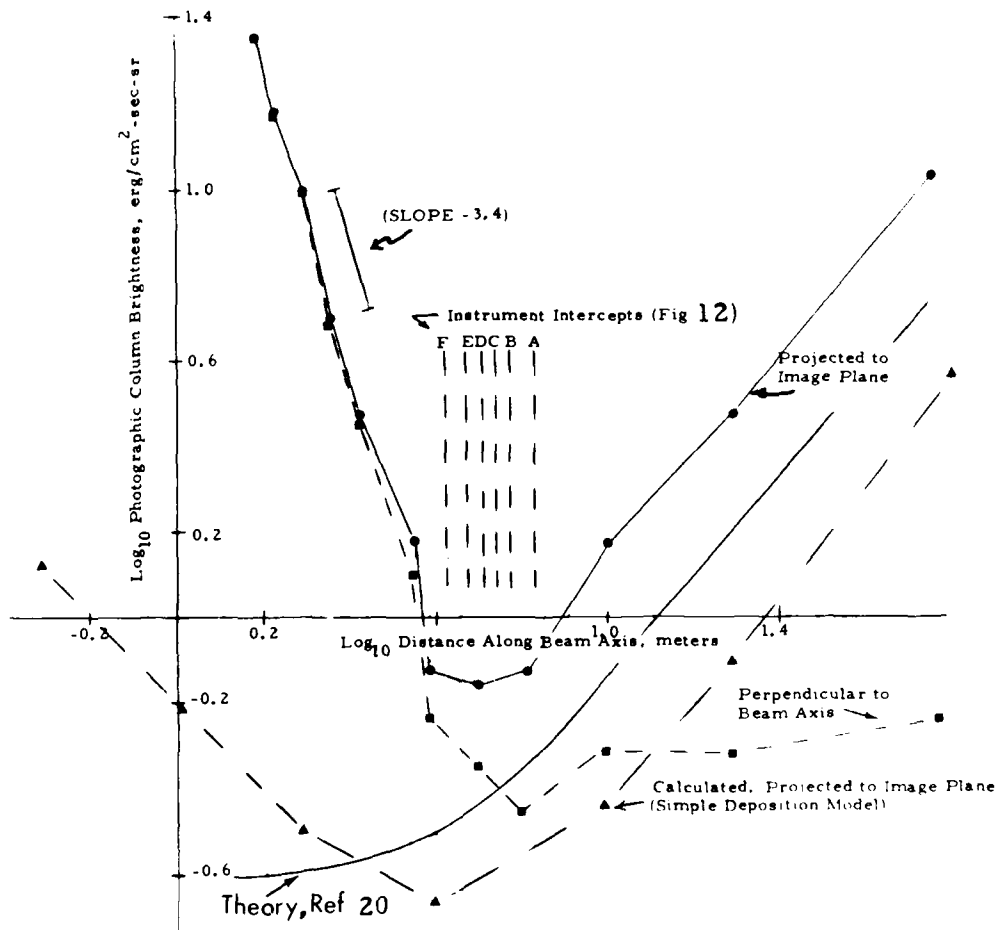


Figure 20. Radiance projected to the onboard camera along the electron beam's axis, and viewing perpendicular to the axis. EXCEDE: Spectral rocket altitude 123 km upleg (154 sec). Note that beyond 4 meters from the anode the beam's brightness viewed normal to its axis remains about constant.

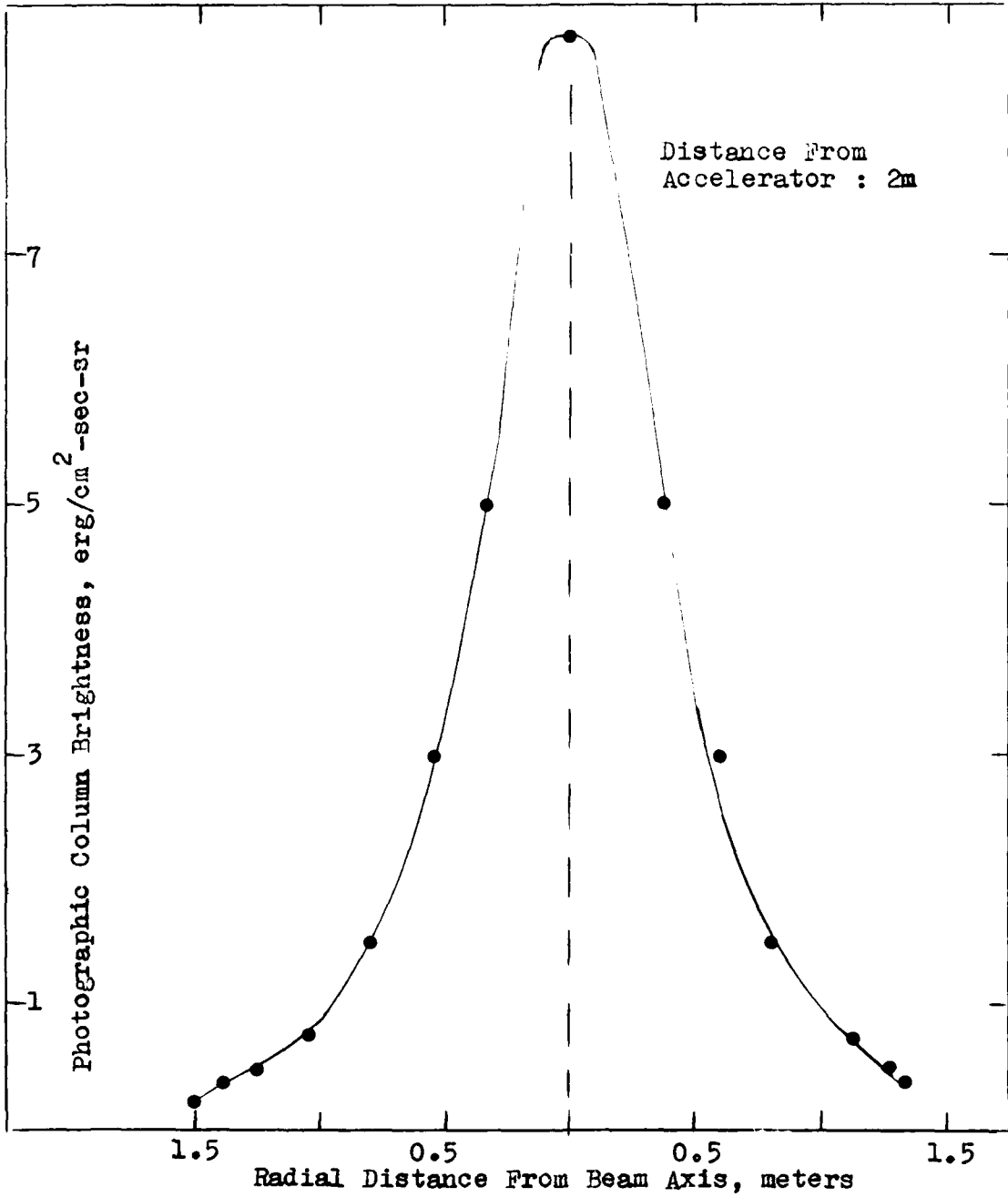
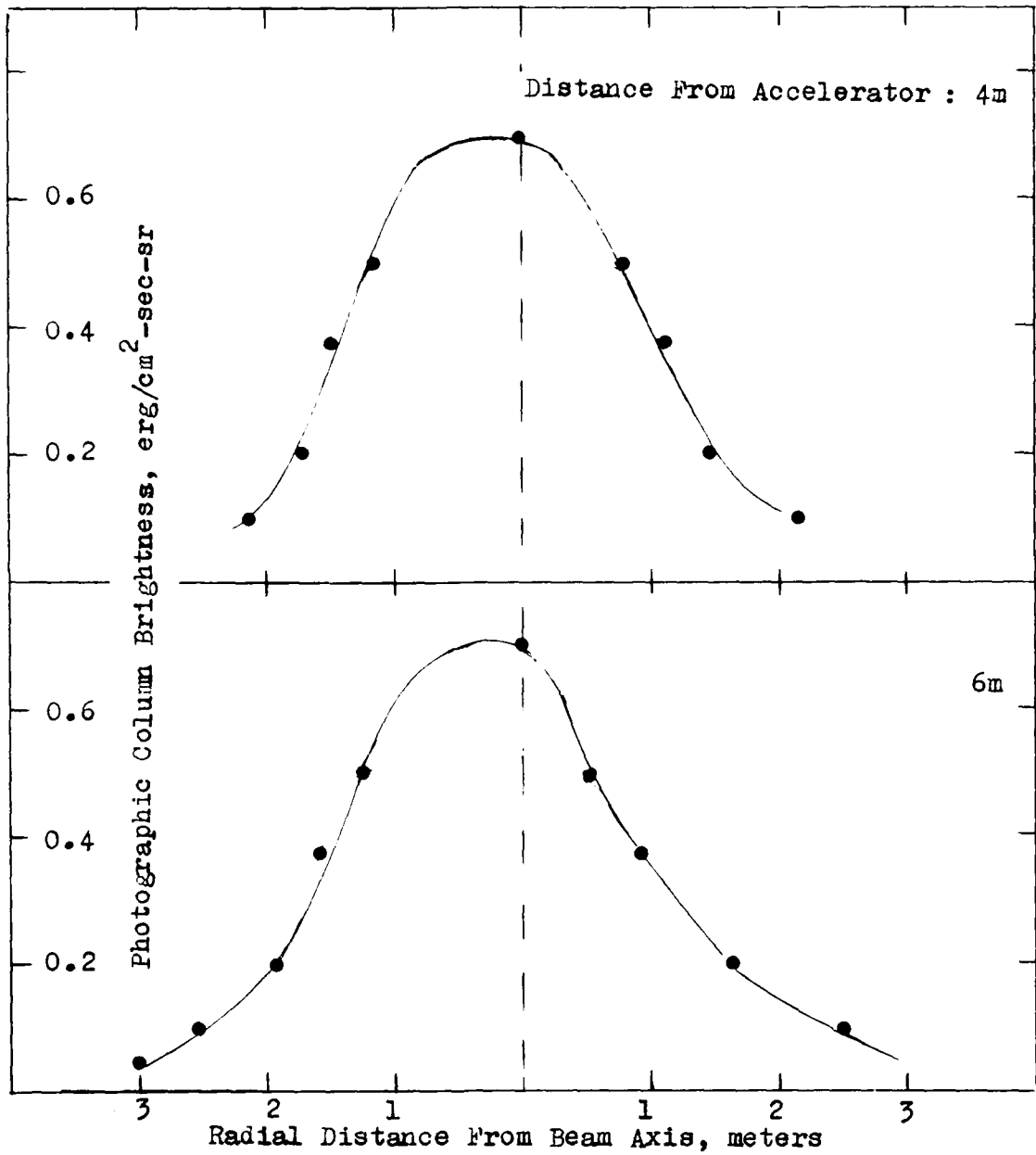


Figure 21. Radiance projected to the onboard camera along lines perpendicular to the electron beam's axis intersecting it at 2, 4 and 6 meters from the anode of the accelerator (Refer to arrows on Fig 18). EXCEDE: Spectral rocket altitude 123 km upleg (154 sec).



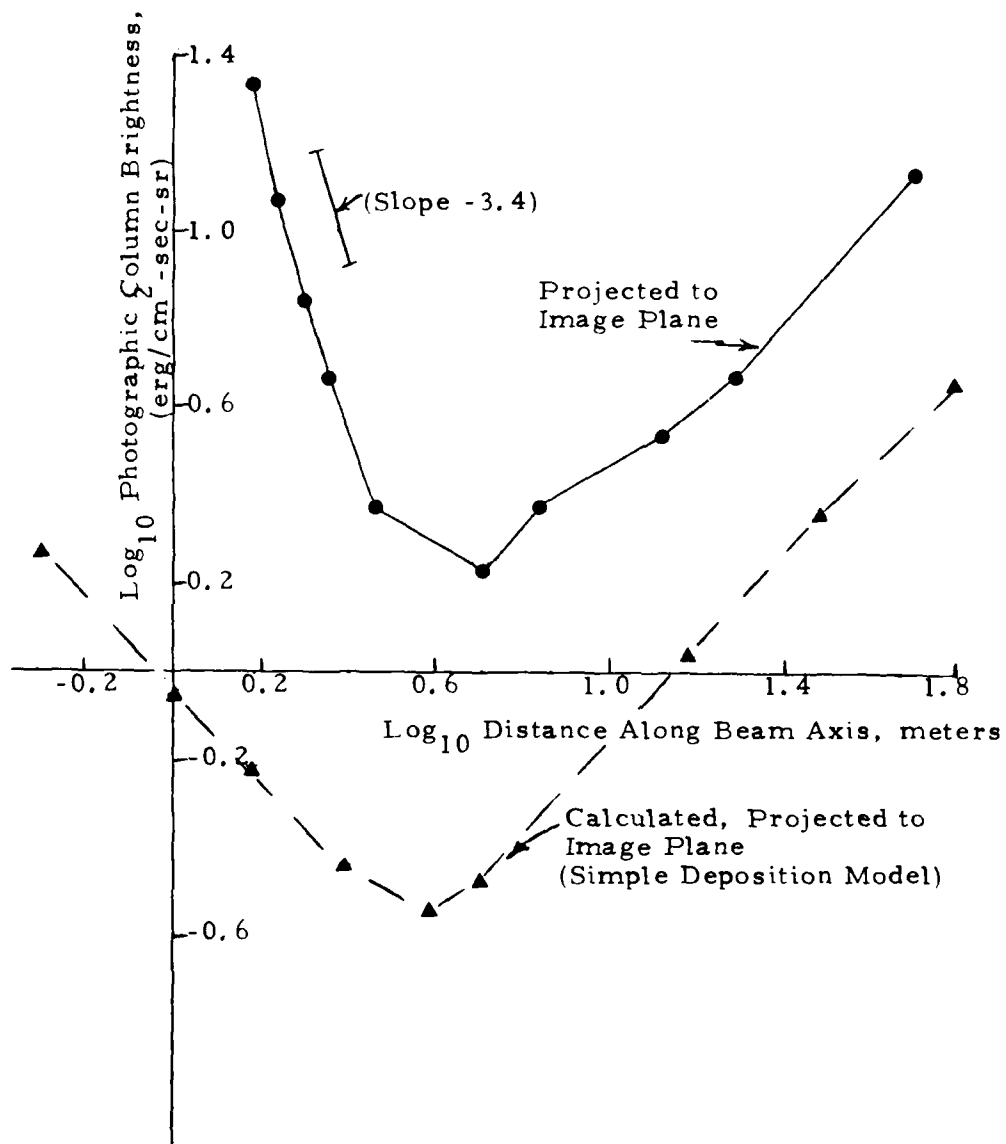


Figure 22. Radiance projected to the onboard camera along the electron beam's axis, EXCEDE: Spectral rocket altitude 113 km downleg (244 sec); replotted from Fig 19.

The axial brightness at 113 km downleg (Fig 19) shows a quantitatively similar very rapid increase toward the accelerator anodes. As an accurate determination of the total charge ejected while the shutter is open has not yet been made from the telemetry record, the comparison of absolute surface brightness is only approximate. Furthermore, the abscissa is subject to a small error, as the geometry scaling in Fig's 19 and 22 is not strictly applicable because the axis of the electron beam is not parallel to the field direction. Nonetheless the data indicate a closely similar interaction with the atmosphere of the ejected beam at the lower downleg altitude, where the atmosphere's density is a factor 4 higher than at 123 km.

The brightnesses near the rocket resemble those seen in low pressure laboratory-tank beam-plasma discharges excited by electron beams (Ref's 21, 22), in which the peak surface radiance becomes about an order of magnitude greater than predicted from the individual initial-particle impacts and the width of the glow region broadens by a factor  $\sim 3$ . Many other observables accompany such discharges: - increased energy spread of the beam electrons, some of which have up to  $1.2 \times$  the initial energy from the accelerator (Ref 22); appreciable electron flux at high pitch angles to the magnetic field, which spreads the beam laterally; intense RF emission at various physically-reasonable frequencies (Ref 29); low-frequency ( $\sim 10$  Hz) flicker in the beam's luminosity; and a greatly enhanced plasma density with increased electron temperature. Other aspects of the discharge near sounding rockets with  $\sim 5$  keV electron accelerators have been observed: intense fluxes of low-energy secondary electrons (Polar 5, Ref 19; also Echo III and Eridan); a qualitatively similar luminosity flicker (Echo IV, Ref 23; also Zarnitsa II); and limited charging of the rocket body, due to unexpectedly high return current (Polar 5, Zarnitsa II).

The data from EXCEDE: Spectral's photometers may provide direct information on the radiation's fluctuation structure, and the energy distribution in the electron beam can be determined from the longitudinal distribution of "core" radiance measured by the ground

cameras. Information about electron energy spectra in the vicinity of the rocket is available from the measured relative intensities of emission features; a well-known example is the ratio of  $N_2$  Second Positive/ $N_2^+$  First Negative bands, and other ratios of visible and UV spectrum features can also be applied (more on this presently). Persistence of the emission for  $\sim 20$  millisecc after the beam is shut off would be expected from measurements of the time dependence of the electron energy spectrum near Echo III (Ref 30). We note that low-energy electrons within the fields of view of the rocket instruments would impact the spectral distribution of infrared radiations; for example the observed strong emission in the 2.7 and 6.3  $\mu m$   $H_2O$  bands might be a result of the water molecule's high cross-section for vibrational excitation by  $\sim 1$  eV electrons (Ref 31), and (as we will show) several other features of the EXCEDE spectrums are also consistent with excitation by heated plasma electrons.

Direct impact excitation of  $N_2$  molecules outgassed from the rocket body might also be invoked as the source of the high radiances close-in along the beam axis. This mechanism, however, does not readily explain the lateral broadening of the electron beam's "core," or its near-constant axial brightness (viewed normally) beyond  $\sim 4$  m and absence of refocusing modes. It is yet to be determined whether outgassing is consistent with the ratios of scene radiances in Fig's 18 and 19a, or the factor - 100 discrepancy between the prediction of the transport model and the measured radiance close-in to the rocket body.

#### SUMMARY AND RECOMMENDATIONS

We have described EXCEDE: Spectral's radiometrically-calibrated camera system and manually derived surface brightness distributions of the air fluorescence excited by electrons ejected from the rocket's electron accelerators at one upleg and one downleg altitude. The radiance data (in Fig's 18-22) are in a form suitable for comparison to the results from theoretical models of energy deposition (for example, Ref 20). The airglows are sufficiently symmetric for

reliable unfolds (not yet performed). To the extent that the excitation rates remain proportional to the rates of emission of the features to which the camera system is sensitive, radiometrically-calibrated film data permit calculation of the referencing power input within the field of each instrument in EXCEDE: Spectral's payload section.

As the black-and-white and/or color film densities are "on-scale" over the full 72 - 128 km measurement altitude range, similar assessments can be made for altitudes above and below the ~92 - 110 km range of validity of Ref: 20's independent particle-transport model. The conversion of film densities to scene brightnesses, which involves correction for the cameras' photometric and geometric nonlinearities, can be readily programmed for execution by computer to produce a "library" of EXCEDE: Spectral radiance and volume emission rate distributions.

The brightness distribution and effective dimensions of the glow within a few meters of the accelerator differ markedly from predictions, and suggest that an electric discharge (similar to those observed from several other ~kilovolts electron-ejection vehicles) may be contributing to the excitation within the fields of the rocket instruments. A possible alternative mechanism, outgassing of  $N_2$  molecules from the rocket body, does not readily explain the broadening of the beam or its absence of node structure. Further information about this enhancement phenomenon should be available in the spectrum (and perhaps time-dependence) data from the rocket's photometers and spectrometers (both persistence and low-frequency flicker is expected in plasma glows), from the ground cameras that measure the distribution of emission intensity along the magnetic field line (those electrons that gain energy in the discharge would have increased end-point range, and the "heated" component would result in increased radiance near the accelerator), and of course from assessment of further frames from the onboard cameras.

A small (and possibly unresolved) very bright region surrounding EXCEDE: Spectral is present in both the groundbased video and film-photographic records reproduced in Ref 18. A similar luminous spot was seen in the Zarnitsa electron-ejection experiment (Ref 30). Heated plasma electrons might be the source of the strong signal in the  $\text{H}_2\text{O}$   $2.7\mu\text{m}$  and  $6.3\mu\text{m}$  vibration-rotation bands, and collisions between directed plasma ions and neutral  $\text{H}_2\text{O}$  could be the cause of the  $\sim 2500\text{ K}$  rotational temperature of  $\text{H}_2\text{O}$ , which also radiates between  $17$  and  $22\mu\text{m}$  (Ref 18).

Several other unexpectedly intense spectrum features reported in Ref 18 are consistent with impact-excitation by the expected large number of  $\sim 10\text{ eV}$  discharge electrons. Enhanced radiations include the ultraviolet Herman-Kaplan ( $E\ ^3\Sigma_g^+ - A\ ^3\Sigma_u^+$ , p 21) and infrared Wu-Benesch ( $W\ ^3\Delta_u - B\ ^3\Pi_g$ , p 29) bands of  $\text{N}_2$ , whose excitation cross-sections peak just above the  $\sim 10\text{ eV}$  threshold and thereafter decrease very rapidly with electron energy, as is characteristic of inter-combination (in this case singlet  $\rightarrow$  triplet) excitation;  $4.3\mu\text{m CO}_2$   $001 - 000$  (p 144), whose excess intensity could be due to the increased vibrational temperature of  $\text{N}_2$  resulting from inelastic collisions with  $2 - 4\text{ eV}$  electrons  $15\mu\text{m CO}_2$  (pp 186-7), whose enhancement (through an electron capture process) would also be due to the soft electrons; and the continuum that underlies the spectra so far published (pp 28-32 and 184), which might be due to plasma radiations. We note also that the interpretation of  $\sim 4.65\mu\text{m}$  emission (p 149 ff) as arising from  $\text{NO}^+$ , which requires three separate reactions, one of which is temperature-dependent, may need to be reconsidered; alternative excitation mechanisms are plasma electron impact on NC molecules, and population of  $\text{CO}(v)$  by direct electron impact on  $\text{CO}_2$ , electron dissociative recombination of  $\text{CO}_2^+$ , or reaction of  $\text{CO}_2$  with  $\text{O}^+$  ions. Evaluation of the absolute volume emission rates in these features, and those in the other  $\text{N}_2$  triplet transitions (in particular, the Second and First Positive systems), can provide information on the atmospheric-excitation conditions in EXCEDE: Spectral instrument fields.

Further information could be derived from spectroscopy of electron beam-irradiated low pressure air in the Johnson Space Center tank, in which various other plasma-diagnostic measurements have been made (Ref's 21,22). It is recommended that future EXCEDE rockets employ remote and in situ sensors such as radiofrequency wave analyzers, plasma density probes, and (in particular) electron energy spectrometers, and also dedicated instruments for absolute measurements of  $N_2$  triplet-manifold features, to characterize the artificial-ionosphere volume. We note also that the high ion densities achievable in ejected beam-induced discharges in the thermosphere may permit verification of theoretical models of the spectral intensity of the plasma radiations, for which no other economically-feasible simulation technique has been proposed.

Our finding of a broadened emitting volume with excess emission intensity close-in to the accelerator, and essentially-expected beam behavior after a few meters, of course refers only to EXCEDE: Spectral's 113 downleg and 123 km upleg altitudes, a range of a factor four in ambient atmospheric density. The altitude (and to a limited extent, ejected-current) dependence of the excitation enhancements, and their overlap on the fields of view of onboard spectroradiometers, can be determined by assessment of further film frames.

### SECTION 3

#### POSITIONING PHOTOGRAPHIC STATIONS FOR TRIANGULATION TO ELIAS AURORAL FORMS

##### BACKGROUND

We describe here the procedure used to calculate the overlap of fields of wide-angle (all-sky,  $165^\circ$  circular) cameras for triangulation to and further characterization of auroral forms whose SWIR emission profiles will be measured from the ELIAS rocket (Ref 2). A master ground station is fixed outside Fort Nelson, BC, Canada ( $58^\circ 48.8' N$ ,  $122^\circ 41.0' W$ ). The decision on where to locate the second site depended in large part on the effectiveness of optical triangulation to regions where incoming-particle energy is deposited within the planned fields of view of the rocket's radiometers; refer to Fig 23.

Candidate ground sites at which instrument and personnel support facilities would be available were

Watson Lake, YT -  $60^\circ 03' N$ ,  $128^\circ 42' W$  (town)  
-  $60^\circ 03' N$ ,  $128^\circ 34'$  (micro-  
wave relay station, away  
from town lights and so  
better suited for measure-  
ment of weak optical signals)

and

Tuchitua, YT -  $60^\circ 54' N$ ,  $129^\circ 12' W$ .

Fig 23 shows the position of these three sites in the  $Q = 4$  auroral oval at 0930 UT (0330 LT, 0130 LT at Poker Range where the rocket trajectory is located) with a typical projection of the instrument fields through irradiated air. The distance between Fort Nelson and Watson Lake (microwave station is 359 km, and between Fort Nelson and Tuchitua 431 km.

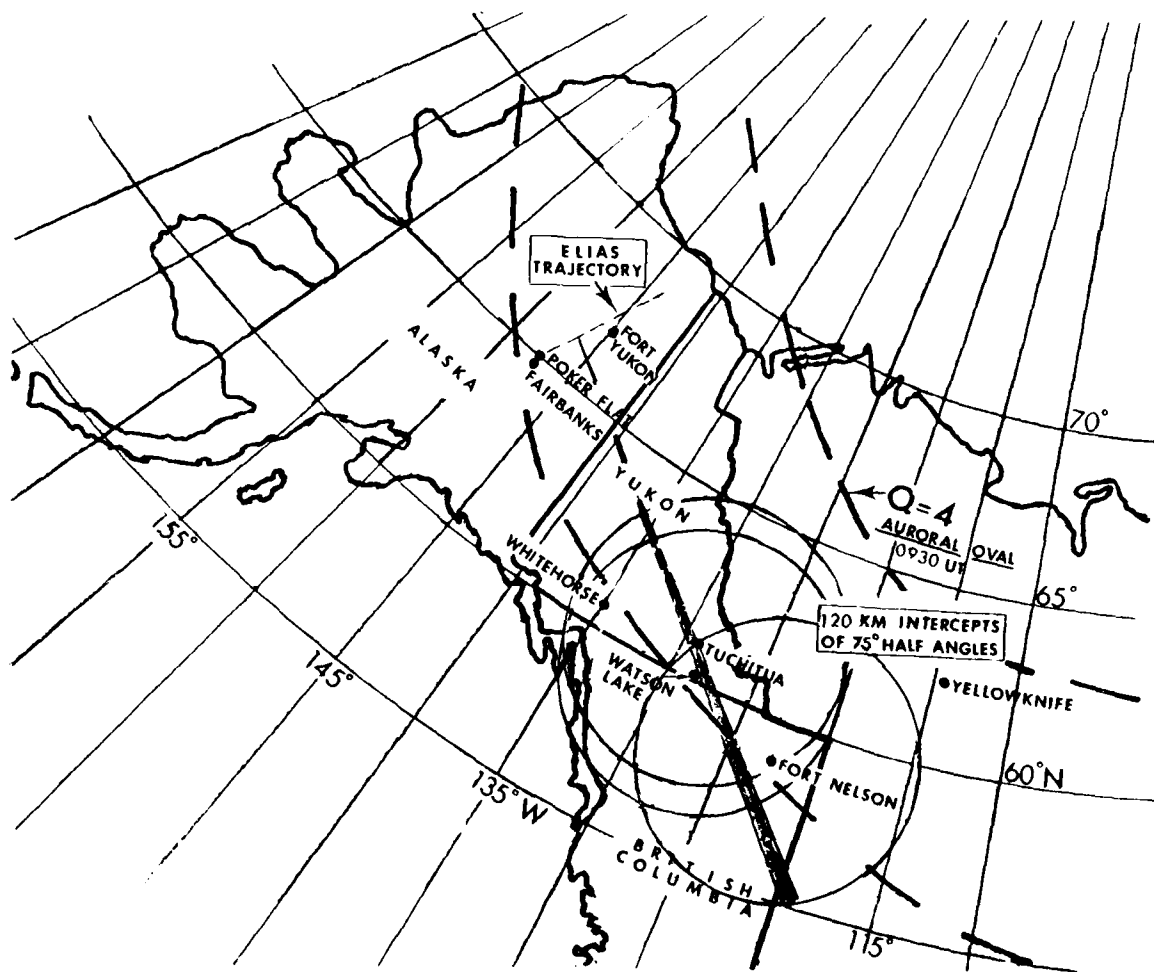


Figure 23. ELIAS limb-viewing geometry with 120 km projections of the 75° zenith angle contours from each ground site and Q = 4 auroral oval at 0930 UT. The projection of the instrument's field is not to scale.

## PROJECTION OF THE CAMERA FIELDS

We select 120 km, the altitude of maximum deposition by an incoming particle beam with the commonly-encountered energy parameter 2.3 keV (in a "Maxwellian" distribution of energies, as described in Appendix II of Ref 6), as the reference altitude for the field overlap calculation. The effect of the earth's curvature is to raise the altitudes at which horizontal planes at Fort Nelson intercept the Watson Lake and Tuchitua zeniths by 10.1 km and 14.7 km respectively. The flat-earth approximation that we applied results in an acceptably small error ( $\sim 2^\circ$ ) in the overlap of effective viewing fields, in terms of impact on the decision on where the second camera site should be located.

We made coordinate transformations of the loci of points at fixed zenith angles from Watson Lake and Tuchitua to a reference frame at Fort Nelson. The procedure is illustrated for the Watson Lake station (138 km east and 339 km north of Fort Nelson) in Fig 24, which defines the symbols used here. Cartesian coordinates of a point  $P_1$  at 120 km altitude and zenith and azimuth angles  $\theta'_1$  and  $\alpha'_1$  from Watson Lake (primed symbols, camera site A) are:

$$x'_1 = (120 \tan \theta'_1) \sin \alpha'_1 \text{ km} \quad (\text{negative for } P_1 \text{ north of Watson Lake, positive south})$$

$$y'_1 = (120 \tan \theta'_1) \cos \alpha'_1 \text{ km} \quad (\text{negative west of Watson Lake, positive east})$$

$$z'_1 = 120 \text{ km.}$$

The coordinates of  $P_1$  with respect to a reference frame at Fort Nelson (unprimed symbols) are:

$$x_1 = -136 + x'_1 \text{ km}$$

$$y_1 = -333 + y'_1 \text{ km}$$

$$z_1 = 120 \text{ km.}$$

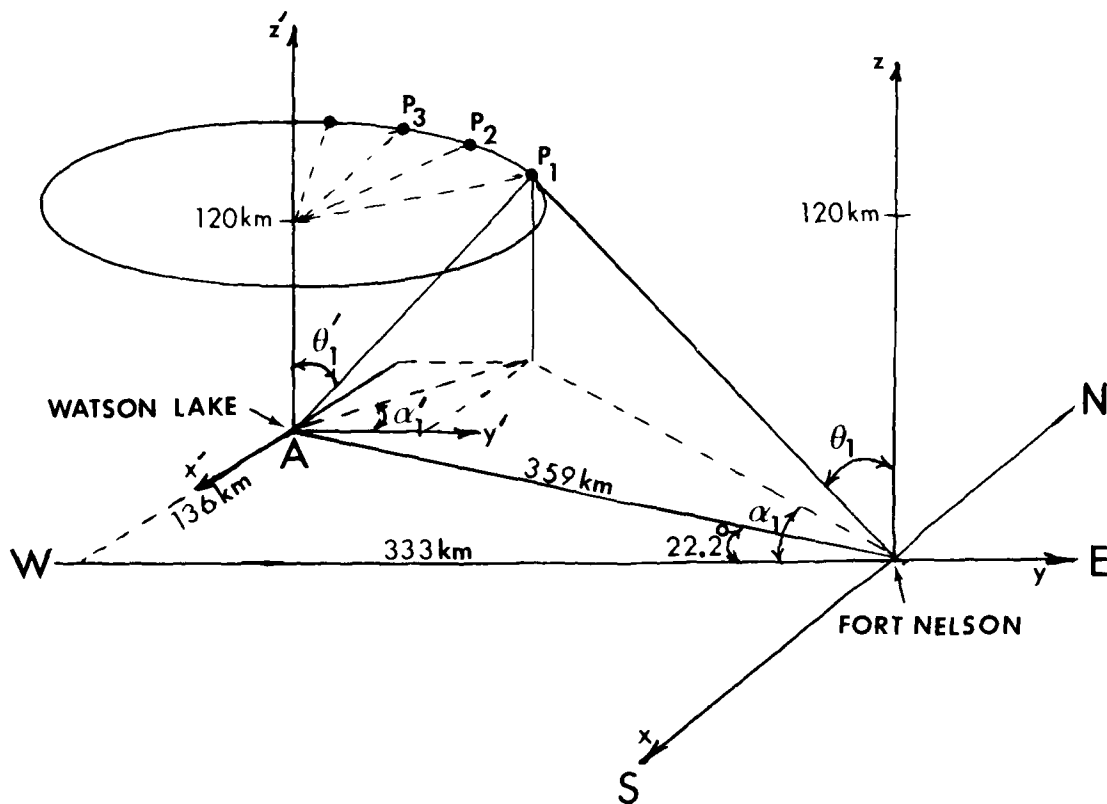


Figure 24. Transformation geometry illustrating the procedure for referencing zenith angle contours from Watson Lake ( $\theta_1'$ ) to a coordinate system with origin at Fort Nelson. Azimuths and elevations ( $\alpha_1, \theta_1$ ) of the locus of 120 km altitude points  $P_1, P_2, P_3 \dots$  are plotted at five values of  $\theta_1$  in all-sky image format in Fig 25.

The zenith and azimuth angles of  $P_1$  from Fort Nelson are

$$\theta_1 = \tan^{-1} \frac{\sqrt{x_1^2 + y_1^2}}{120}, \quad \alpha_1 = \tan^{-1} \frac{x_1}{y_1}.$$

The calculation is repeated for points  $P_2, P_3, \dots$  at the same zenith angle ( $\theta'_1$ ) at azimuths  $\alpha'_2, \alpha'_3, \dots$ . The result describes the projection of the Watson Lake  $\theta'_1$  cone on a 120 km-altitude plane, as seen from Fort Nelson. A similar series of calculations is made for  $\theta'_2, \theta'_3, \dots$ . The dashed lines in Fig 25 show the Watson Lake  $\theta' = 40^\circ, 60^\circ, 70^\circ, 75^\circ$  and  $80^\circ$  field boundaries at 120 km projected to Fort Nelson.

The results of the calculations for a camera located at Tuchitua are represented by dots on Fig 25. Since the Tuchitua site is some 96 km farther north and 31 km farther west of Fort Nelson than is Watson Lake, overlap on the optical aurora takes place over a smaller solid angle of the zenith hemisphere.

#### COMMENTS

The overlaps in Fig 25 are independent of the zenith angles of the cameras' optic axes. The effects of angular compression (which reduces spatial resolution) and vignetting (which reduces brightness resolution) near the edge of the all-sky camera field could be mitigated by tilting fields toward one another. This of course has the effect of reducing the total area from which auroral "input" is assessed by a single camera pair. We note that since foreshortening and the atmosphere's attenuation reduce the reliability of triangulation to forms at  $\geq 75^\circ$  zenith angle, the  $75^\circ$  contour is probably the best choice in determining the effective area over which camera fields overlap.

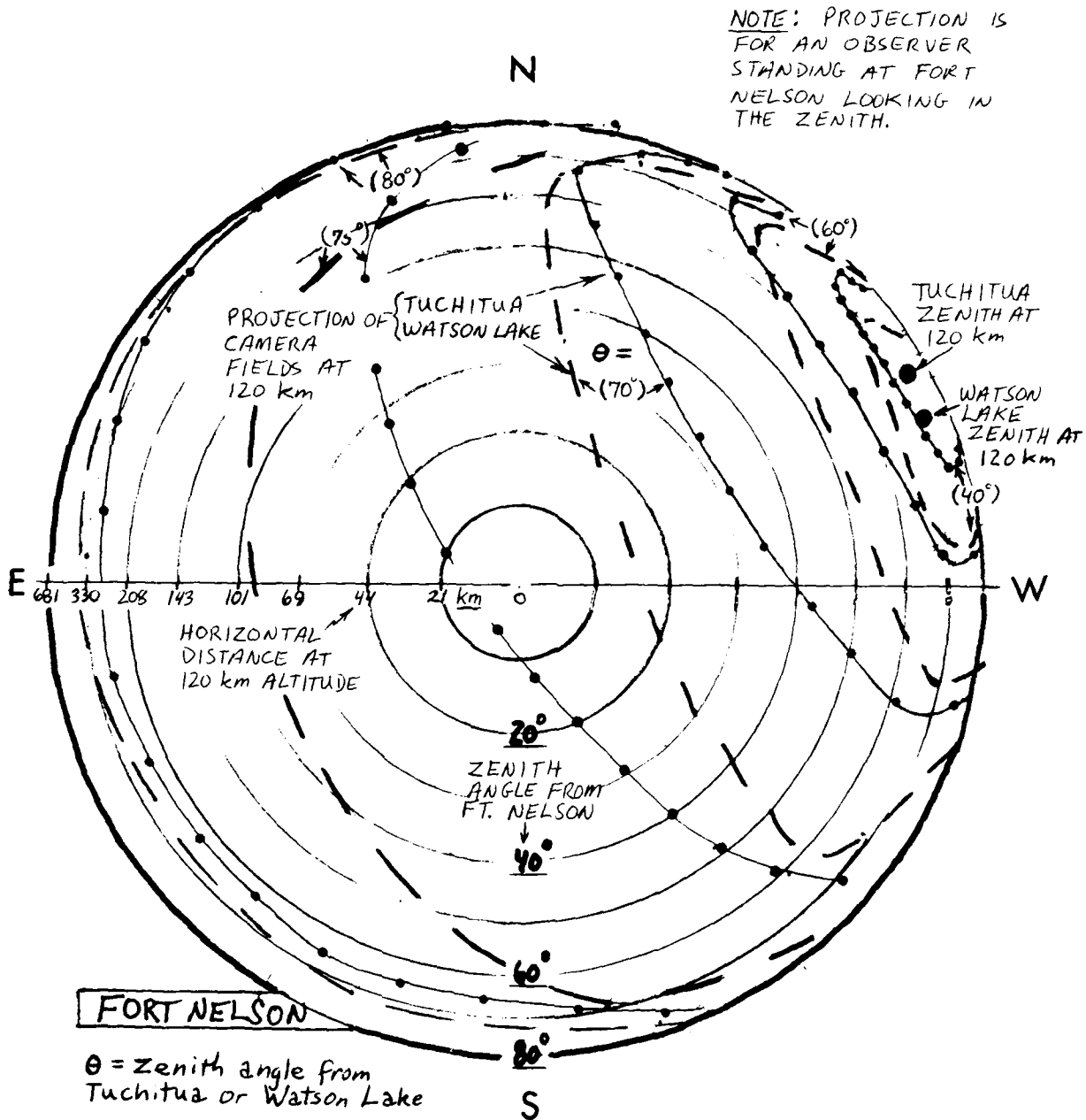


Figure 25. 120 km projections of five contours of zenith angle from Watson Lake (---) and Tuchitua (•—•—•) at Fort Nelson. The zenith hemisphere at Fort Nelson is represented as it would be imaged by a conventional refractive all-sky ( $165^\circ$ ) lens. Earth curvature, which has only minimal effect on the apparent overlap of the camera fields ( $\leq 2^\circ$  in zenith angle), has been neglected in the calculation.

## SECTION 4

### TRANSFER CALIBRATION OF THE AIRCRAFT PHOTOMETER

#### INTRODUCTION

The narrow-field air fluorescence photometer built for the 1979 aircraft measurements (Section 5) was a new design whose pre- and post-flight calibrations are only indirectly applicable to its operation in the field and which otherwise exhibited performance irregularities. These deficiencies were corrected for the 1980 auroral flight series.

Reliable instrument calibration is needed to determine absolute SWIR yields in the dark and sunlit particle-excited atmosphere, and for effective, systematic application of the crosscorrelation and related data-evaluation procedures that we described in the Test Plan (Appendix I of Ref 4). This Section documents our work in conjunction with AFGL/OPR to derive radiometric calibrations for the 1979 flight missions, which are listed in Table 3.

#### PHOTOMETER OPTICS

The photometer is designed to measure intensity in the  $N_2^+$  First Negative 0,0 band at  $3914 \text{ \AA}$  and the OI forbidden green line. A dichroic filter isolates optical wavelengths above the  $N_2^+$  bands, which are directed to a  $5577 \text{ \AA}$  interference filter and separate phototube and recorder channel. Leakage of the  $3914 \text{ \AA}$  interference filter at longer wavelengths invalidated measurements of photometer sensitivity to air fluorescence using a blackbody continuum radiance source, and a separate pre-flight calibration using a monochromator is inaccurate because of the illumination conditions do not match those under which the auroral data are taken. A drift in the instrument's baseline (or "dark") output voltage introduced further difficulties in relating this output to real radiances. Furthermore, a  $3914 \text{ \AA}$  post-calibration for the Spring 1979 flights could not be applied to the Fall 1979 data because the multiplier phototube had been replaced and amplifier gain settings changed in the interim.

Table 3. SWIR emission data flights of narrow-field radiometer/photometer, 1979

<u>Flight</u>	<u>Date</u>	<u>Mission</u> ***	<u>Duration</u> (data duration)	<u>Aurora Encountered</u>
906	21 April 79	N	6.3 hr (4.3)	Equipment checkout; photometer not operating. Weak auroral activity.
907	23 Apr	N	6.5 (4.3)	Frequent pulsating forms moderate intensity.
908	25 Apr	N	7.8 5.5	Strong, some IBC III arcs.
909	26 Apr	T & N	6.0 (4.5)	Strong, IBC II <sup>+</sup> broad arcs.
910	30 Apr	N & T	7.0 (2.5)	Active but low level.
911	01 May	T & N	7.3 (3.3)	Mostly diffuse precipitation, some weak stable arcs.
-----				
924	17 Sep 79	T & N	5.3 (3.4)	Very weak, sporadic activity.
925	20 Sep	HEAO-C Launcher	6.5 -	See Section 7 of DNA 5127F (not an auroral mission).
926	24 Sep	T & N	7.1	Slightly more activity than in 924.
927	27 Sep	N	6.5	~2½ hrs of weak continuous emission.
928	28 Sep	T & N	7.3 (3.7)	Moon up, ½ full. Weak activity all night.
-----				

\* From Pease AFB, NH to the auroral oval region bounded by 60°N.

\*\* Night. T = Twilight.

The photometer design places the wavelength-isolating interference filters in the converging beam of its objective lens. The half-angle over which this nominally-f/3 lens illuminates the filter ( $\tan^{-1} 1/2f$ ) is  $9\frac{1}{2}^\circ$ . Measured in parallel light (effectively,  $f/\infty$ ) at normal incidence, its transmission was found to peak at  $3902 \text{ \AA}$ , with a full-width to half-peak of  $21 \text{ \AA}$  (Fig 26). As the wavelengths transmitted by interference filters decrease with increasing angle of incidence, the passband shifts downward in the photometer's optical system.

The shift in a convergent beam of half angle  $\Theta$  with axis normal to the filter surface is one-half that in a parallel beam at incidence angle  $\Theta$ , which is given by

$$- (\text{center wavelength}) \times \frac{\Theta^2}{2} / (\text{effective filter refractive index})^2$$

(Ref 32). The change in "shape" of the filter characteristic is small for small incidence angles. Effective refractive index, which is intermediate between the high and low indexes of the materials used in the interference filter's component layers, is about 1.45 in designs for the wavelength region near  $3900 \text{ \AA}$  (Ref 33). Thus the calculated downshift in a f/3 illuminating beam is  $12.7 \text{ \AA}$ . This would place the peak transmission at  $3889 \text{ \AA}$  and the upper half-power wavelength at  $3902 \text{ \AA}$ , well shortward of the band's P-branch just below  $3914 \text{ \AA}$ .

Measurements (in 1980) of the spectral sensitivity of the photometer fitted with the 1979 filter, with a properly-filled entrance aperture, showed the downshift to be  $8 \text{ \AA}$ . This suggests that the f-number of the objective lens as mounted is closer to 3.5 and/or the effective refractive index of the interference filter is greater than 1.45. In any case the photometer transmits only a small fraction of the  $3914 \text{ \AA}$  band; applying the relative spectral sensitivity measured in 1980, transmission is about 0.13 when the  $N_2^+$  rotational temperature is 200 - 300 K (that is, for energy deposition below  $\sim 120 \text{ km}$  altitude). The filter also transmits much of the 1,1 band of the  $N_2^+$  First Negative system, whose P-branch head is at  $3884 \text{ \AA}$  and whose intensity is 1/19 that of the 0,0 band.

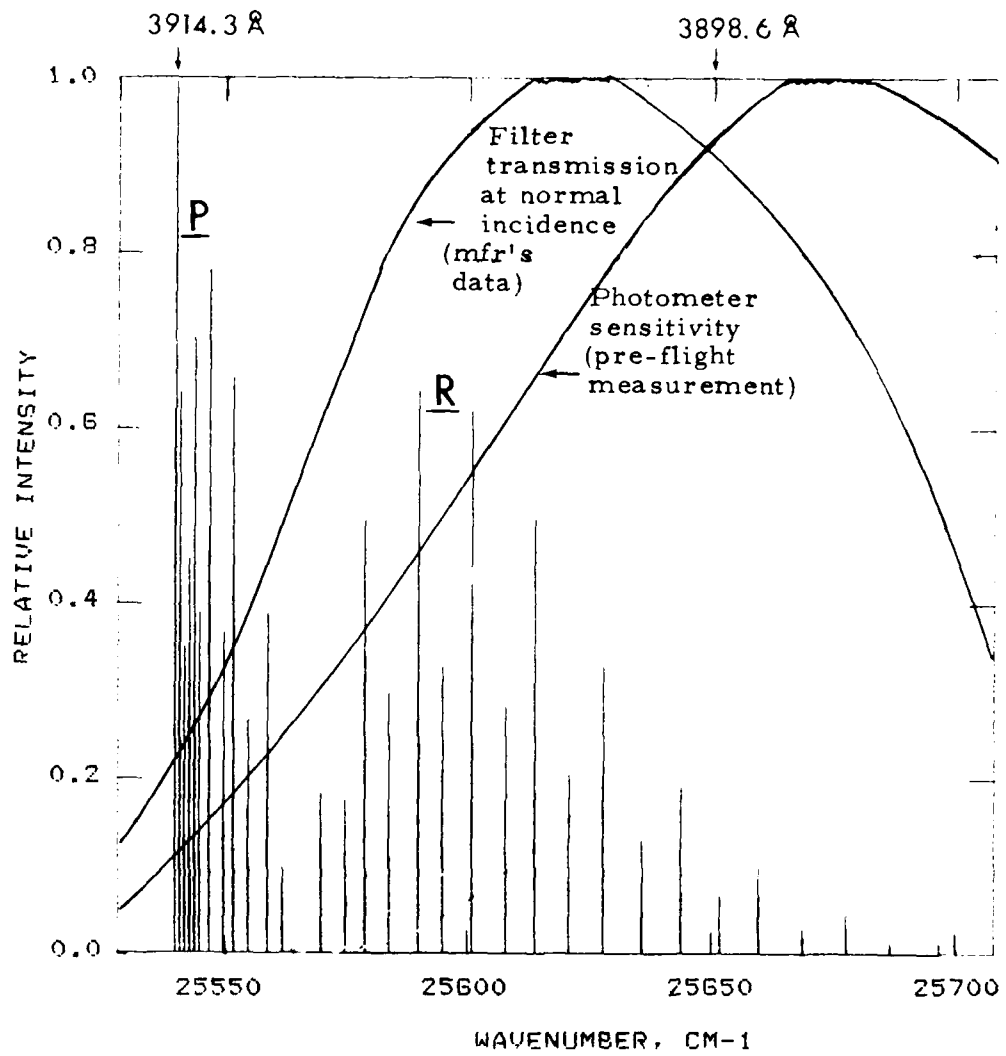


Figure 26. Model relative spectral sensitivity of the narrow-field photometer and spectrum of the  $N_2^+$  0,0 First Negative band at 200K rotational temperature.

## TRANSFER CALIBRATION

A transfer or cross-calibration was available from the data taken by the NKC-135A aircraft's wavelength-sampling photometer (Ref 4). The principal function of this instrument is to determine altitudes of maximum energy deposition (Ref 6), one input to which is the column energy input rate. Its other channels (there are 12 in all, including two used for standardization) measure nitric oxide precursor species radiations and the OI  $^1S - ^1D$  forbidden green line. The filters are in front of the objective lens, and calibration is done by 1) measuring filter transmissions at normal incidence and 2) exposing the photometer to a uniform-radiance source of known spectral emission.

Intensity in the  $N_2^+$  First Negative 0, 1 band at  $4278 \text{ \AA}$  is measured during two  $1\frac{1}{2}$ -second segments of each of the 24-sec cycles of the photometer's filter wheel, and  $5577 \text{ \AA}$  once per cycle. The field of view of this second photometer during the flights in Table 3 was  $2^\circ$  circular (it is defined by an iris); the photometer coaligned with the short wavelength infrared-sensitive radiometer has a  $0.4^\circ$  square field. Its optic axis was pointed toward the zenith in Flights 906-910, after which a glass wedge was installed in its entrance aperture to direct the axis  $13^\circ$  forward and thus nominally parallel to that of the narrow-field photometer. In practice the two instruments may be misaligned by as much as  $1^\circ$  in elevation and azimuth, as they are physically separated in the aircraft by 43 feet; the airframe is known to flex in flight, and in any case even static (ground) alignment over this distance is prohibitively expensive. The new photometer, on the other hand, had been accurately aligned with the radiometer and low light level video camera using a specially-designed optical bench (Ref 34).

Data traces for a transfer or comparison calibration, arbitrarily normalized to one another for display purposes, are shown in Fig 27. The radiances measured by the 12-channel photometer have been manually averaged over the  $1\frac{1}{2}$ -sec dwell time of its filter,

FLIGHT 911 1 MAY 79

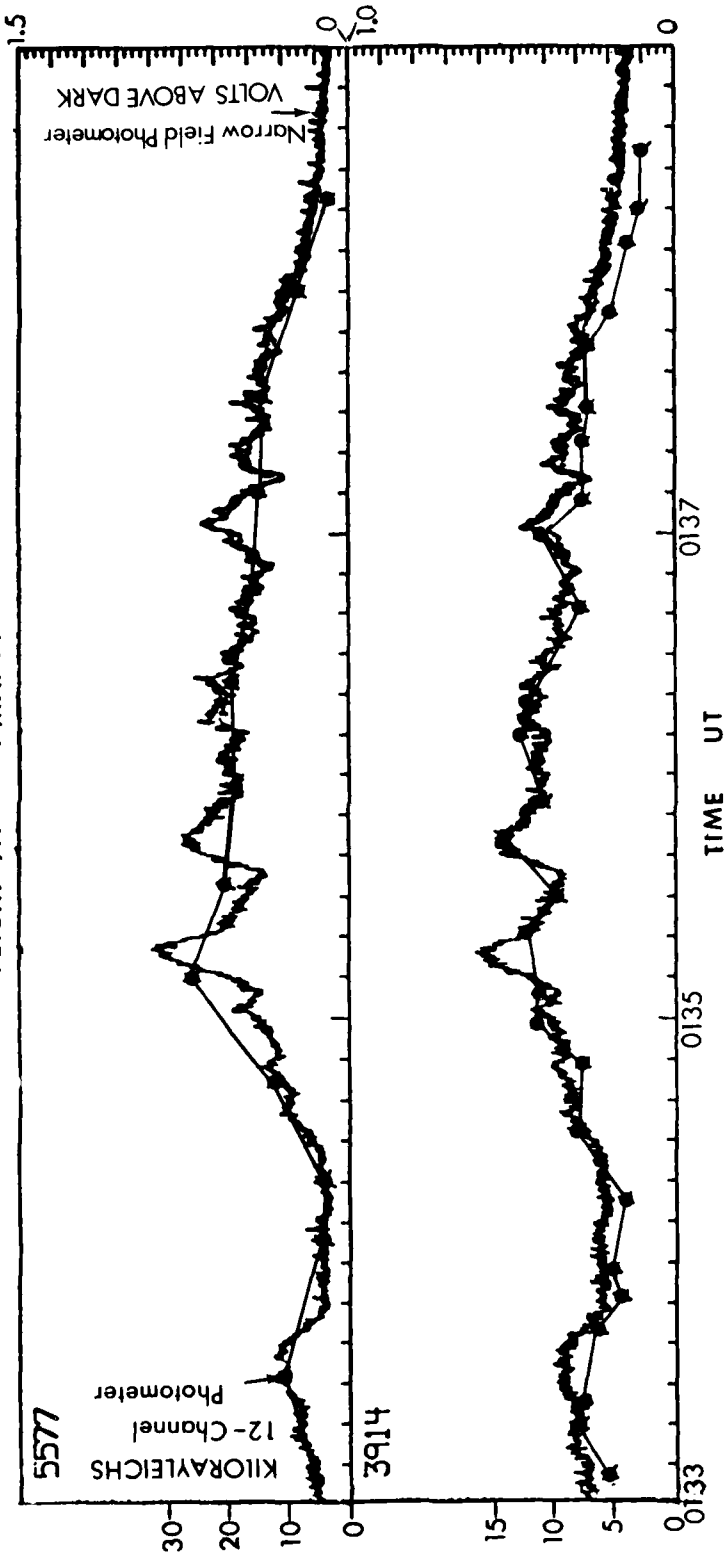


Figure 27. 5777 Å and 3914 Å column brightnesses measured by the 12-channel photometer (dots) overlaid on the voltage output signal from the near-co-aligned narrow field instrument. Data from this segment have been included in the cross-calibration scatter plot in Fig 28. The solid lines are drawn solely for the purpose of linking the radiance samplings of the filter-cycling instrument.

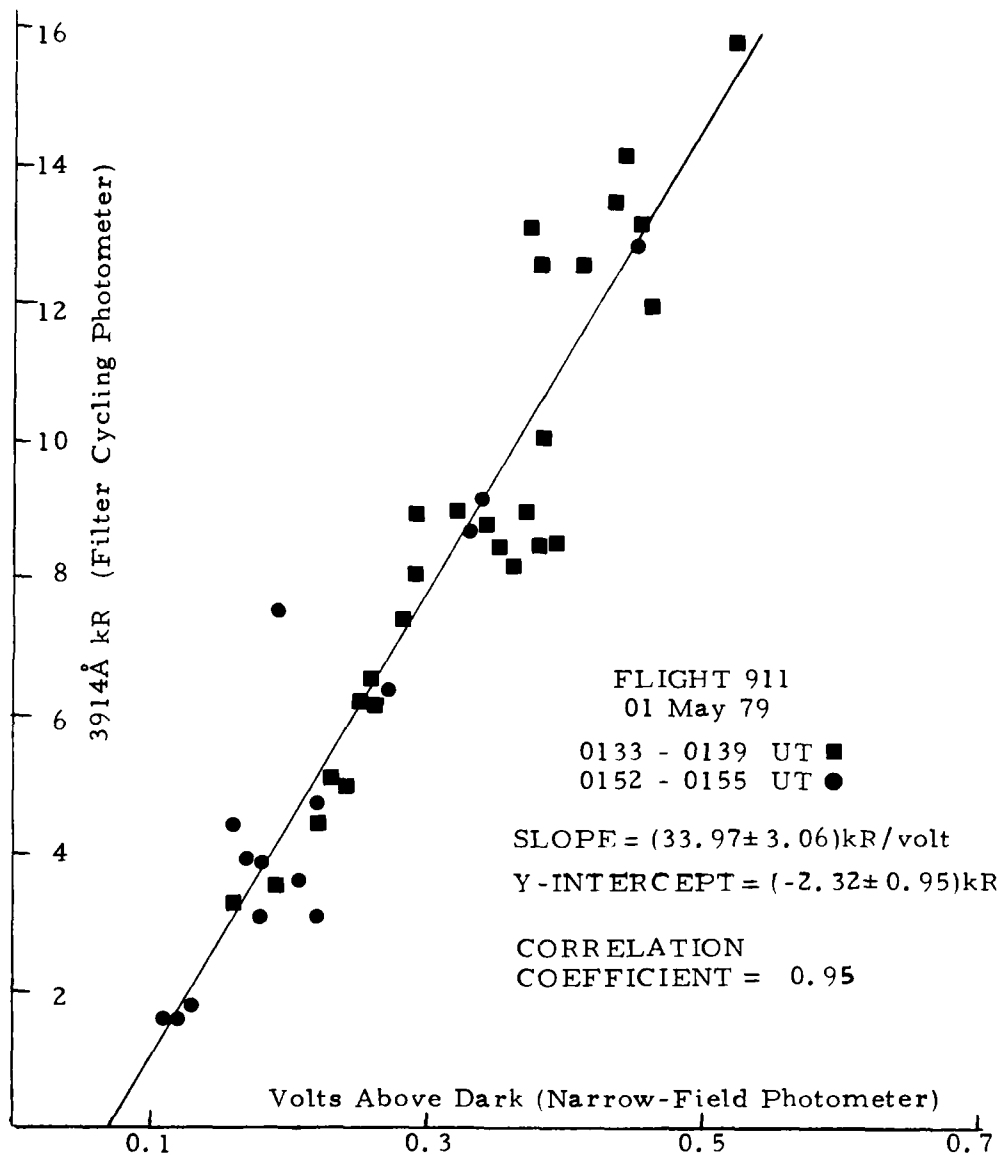


Figure 28. Cross-plot of  $N_2^+$  First Negative band intensities measured by the aircraft's 12-channel photometer and signal output from the narrow-field photometer in a segment of Flight 911. Scatter about the least square fit line is thought to be due to variations in the mean radiances over the two fields of view, which have different acceptance angles with optic axes only nominally coaligned. Failure of the regression line to intercept the origin is caused by a small residual baseline offset in the voltage record. The statistical errors refer to 90% confidence limits.

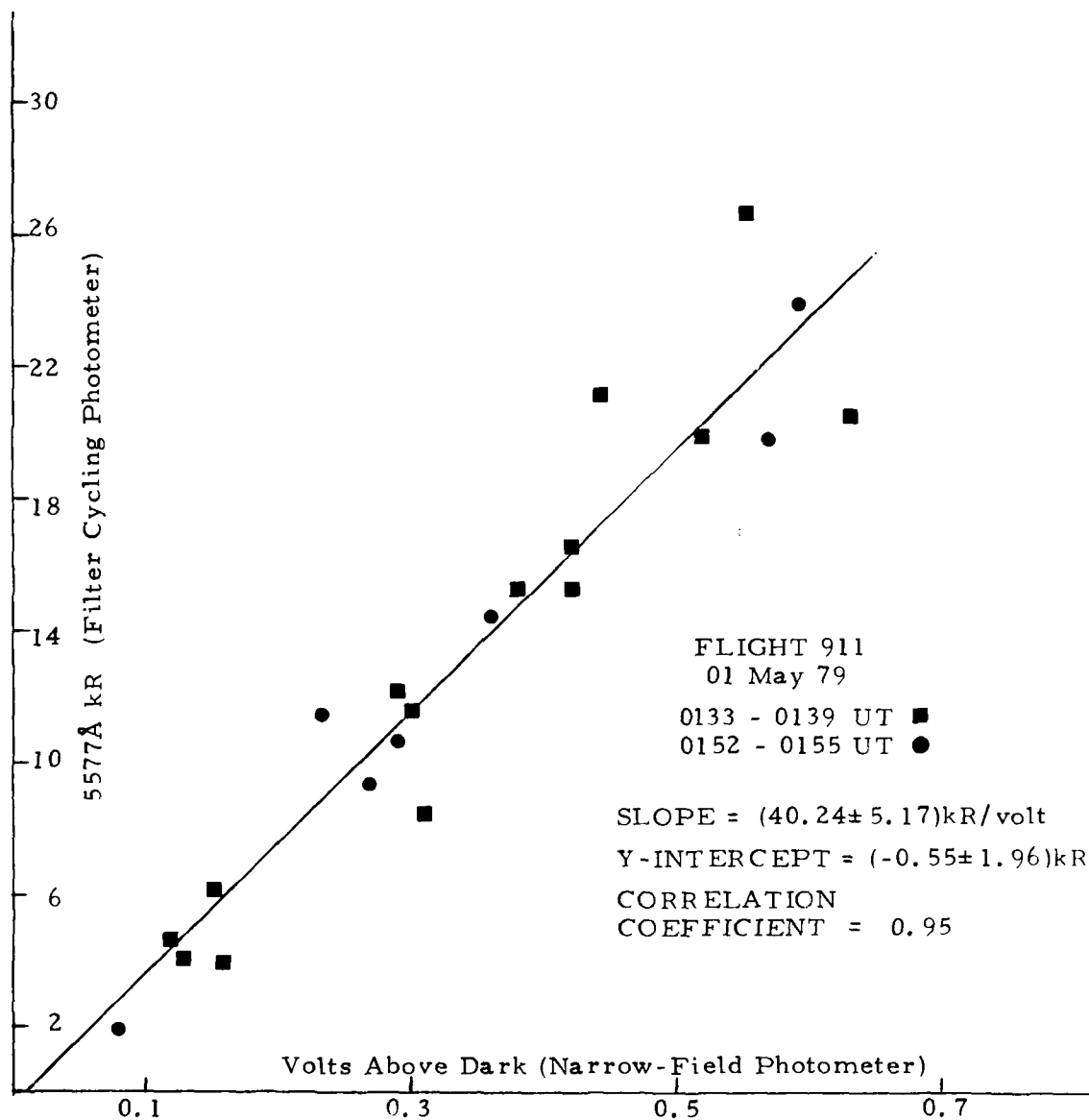


Figure 29. Cross-plot of OI 5577 Å line intensities measured by the 12-channel photometer and signal output from the narrow-field photometer.

and the telemetry voltage readings from the narrow-field photometer are averages over 0.22 sec plotted each 0.30 sec. The latter are expected (on the basis of the electronic design) to be linear in photocurrent. Data on the OI 5577 Å line also serve to indicate the resolution of the wavelength-cycling instrument in identifying narrow arcs, pulsations, and other rapid changes in brightness of the auroral scene.

The two First Negative Band traces show some degree of scatter, which suggests that the auroral radiance does not have the same average over the narrow and wider fields. Differences in local mean radiance would be expected when the particle input distributions are rapidly varying (in space and/or time). A cross-plot of the two data streams in Fig 27, with points added from a further 3 min of IBC II aurora some 18 min later, shows a correlation coefficient of 0.95 and a  $\pm 9\%$  statistical error (90% confidence limit) in the best-fit slope (Fig 28). The narrow-field photometer readings for Fig 28 were taken from a printout of the telemetry voltages with running average 0.22 sec at the center point of the wavelength-cycling photometer's  $1\frac{1}{2}$ -sec average reading, and each data point was given equal statistical weight in locating the regression line.

A plot for the 5577 Å channel (Fig 29) shows the same correlation but somewhat more uncertainty in slope, which may be due to the smaller number of data points. Weighting radiances below  $\sim 5$  kR would perhaps increase the reliability of each transfer characteristic, as weak aurora (in particular, diffuse forms) tends to vary less in space and time. On the other hand the short-lived positive and negative differences between the two mean radiances in strong aurora are at least in first approximation equally probable, and thus do not seriously reduce the accuracy of the cross-calibration.

Note also that the best-fit line for the 3914 Å band fails to extrapolate through the origin of zero output (telemetry) volts. Although this finding implies some error in the zero correction applied to the narrow-field photometer data, the accuracy of the transfer calibration is not affected if this offset remains constant

throughout the measurement period. (Within statistical error, the 5577 Å regression lines does pass through the origin.)

#### APPLICATION

The transfer calibrations from the segment of Flight 911 in Fig's 28 and 29 are now being applied to the Spring 1979 narrow-field photometer records. Concurrently an effort is underway to validate the procedure by relating the pre- and post-flight measurements of the spectral sensitivity of the new instrument to this transfer calibration. Similar cross-calibrations in segments of the Fall 1979 auroral flights indicate that the slope of the regression line (which is proportional to the instrument's output voltage to photocathode current "gain") remains constant, with some variation in the zero-illumination baseline voltage; this effect is now being investigated.

A new interference filter for the 3914 Å band, with negligible leakage and maximum transmission shifted to longer wavelengths to increase the photometer's sensitivity, was installed for the Fall 1980 flights. In addition a full system calibration was performed with a monochromatic illuminator that fills the instrument's entrance aperture. We plan to apply the transfer calibration procedure described hereto the precalibrated 1980 data, to validate its application for the 1979 auroral flights.

## SECTION 5

### AIRCRAFT SWIR STRUCTURE DATA

The data missions of NKC-135A A/C 55-3120 listed in Table 3 were supplemented by five further ~5 hr flights in the auroral oval near twilight from Eielson AFB, AK (plus nighttime ferry flights from and to Pease AFB, NH, during which the narrow-field instruments were operated) in August 1980. (The Test Plan for the aircraft program is in Appendix I of Ref 4, a discussion of atmospheric-scattering backgrounds when the auroral ionosphere is sunlit is in Section 5 of Ref 3, and a preliminary account of the sky radiance measurements by the 2.8 - 3.1  $\mu\text{m}$ -sensitive radiometer and its co-aligned air fluorescence photometer in 1979 is in Section 1 of Ref 3.) Some of the twilight data again showed obviously longer SWIR radiance decay times than typically measured at night (an early example of this "lag" effect is in Fig 4d of Ref 3), while traces from other flight segments indicated less definite delays.

Final calibrations (Section 4) were not applied to the aircraft records by the experiment group in time for PhotoMetrics to quantify infrared-visible correlations (by applying the procedures in the Test Plan, for example) and assess apparent chemiluminous yields under steady-state particle bombardment. To determine the dependence of decorrelation on auroral and measurement conditions, we have listed these parameters in Table 4 for 15 ~5 min segments of  $\geq$  IBC II (20 kR  $\text{N}_2^+$  First Negative 0, 0 band) near -zenith intensity. It should be noted that further periods of high SWIR enhancement signal/noise are present in the data traces.

The entries in Table 4 are as follows. The first column lists the flight date and the time of meridian passage (which is needed to determine solar elevation) at the midpoint of the data segment, whose duration is in the second column. Aircraft position, fuselage heading, and direction of the flight trajectory follow; the latter two azimuths

Table 4. Auroral and observation parameters during SWIR enhancements

FLIGHT# / DATE Meridian Passage	TIME (Z)	A/C POSITION		TRAJECTORY			DECLINATION (degrees)	SOLAR ANGLE (not 13 deg corrected)	SOLAR ANGLE (13 deg corrected)	ILLUMINATED HEIGHT (km) (h=1.98 $\phi$ )	RATIO <sup>++</sup>		PEAK ALTIMITUDE <sup>+++</sup> (km)	MAGNETIC INDEX <sup>+++</sup>		AIRCRAFT ALTIMITUDE (km)
		Lat	Long	HEADING True Mag	AZIMUTH (degrees)	DECLINATION (degrees)					(6300/4278) (5577/3914) photons/photon	K		K <sub>p</sub>		
907/23Apr79 1158 TNP	0248	52.69	67.06	007	029	012	12.30	-21.67 D	-21.50	453.0	6.5/16.5	<100/47.0	119.5	4	5	
	0250:120	52.99	66.95	007	029	012		-21.74 D	-21.55	455.1						
	0250:125	< A/C turning>														
909/27Apr 1158	0237	61.34	71.30	321	340	331	13.61	-10.98 D	-10.75	113.3	11.1/14.9	84.8/43.2	133.7	3	3	
	0240	61.63	71.76	321	340	331		-10.82 D	-10.59	109.9						
	0213	58.90	68.67	325	360	338	13.60	-12.14 D	-11.91	139.0	7.0/18.3	753.1	119.5	3	3	
	0216	59.22	68.93	325	360	338		-12.02 D	-11.79	136.2						
	0220	59.54	69.20	325	360	338	13.60	-11.89 D	-11.73	134.8	9.6/24.3	96.0/70.6	119.8	3	3	
	0224	60.07	69.67	325	360	338		-11.66 D	-11.43	128.0						
0256	61.76	69.61	144	180	155	13.61	-12.08 D	-12.31	148.5	5.1/6.4	29.1/18.6	127.7	3	3		
	0259	61.45	69.28	144	180	155		-12.58 D	-12.80	160.6						
908/25Apr 1158	0637	47.08	67.51	340	360	344	13.01	-23.42 D	-23.28	531.1	4.9/11.9	76.7/34.5	120.0	7	8	
	0640	47.36	67.66	340	360	344		-22.89 D	-22.75	507.2						
924/18Sep 1154	0016	58.36	73.57	281	316	279	2.19	-9.40 D	-9.18	82.6	11.0/10.9	73.8/31.6	159.5	4	6	
	0019	58.20	74.12	249	300	269		-9.55 D	-9.34	85.5						
926/25Sep 1152	0016	58.04	77.67	(264	292	265)*	-0.54	-10.05 D	-9.83	94.7	<del>44/8.2</del>	65.1/23.8	127.2	3	4	
	0022	57.32	78.02	171	168	198		-10.84 D	-10.94	117.3						
927/27Sep 1151	0220	54.77	68.83	327	356	327	3°	-30.70 D	-30.47	989.9	2.5/1.3	13.7/3.6	145.1	3	3	
	0223	55.05	69.13	330	360	330 (turn)		-30.62 D	-30.40	985.7						
928/29Sep 1151	0119	57.10	76.59	230	260	228	-2.11	-20.21 D	-20.13	397.1	4.5/11.8?	(50.4/34.1)?	118.1?	3	4	
	0123	56.76	77.27	230	260	228		-20.53 D	-20.45	489.8						
023/07Aug80 1206	0654	62.99	122.82 <sup>+</sup>	284	252	286	16.36	-9.12 D	-8.99	79.2	2.6/9.0	47.9/26.1	116.0	3	2	
	0704	63.34	124.75	284	252	286		-8.75 D	-8.62	72.8						
026/18Aug 1204	1125	65.86	147.49 <sup>+</sup>	029	360	030	12.97		-10.10 I	100.0	4.1/36.6	<196/106>	108.8	2	5	
	1126	65.16	147.36	029	360	030			-9.95 I	97.0						
	1159	64.36	148.43 <sup>+</sup>	209	177	207	12.96		-9.31 I	84.9	4.4/12.4	<56/36>	118.8	2	5	
1203	63.93	148.95	209	177	207			-9.61 I	90.3							
027/19Aug 1204	1024	64.30	148.42 <sup>+</sup>	026	358	029	12.65		-12.89 I	162.8	2.6/21.2	111.8/61.5	108.8	6	5	
	1030	64.93	147.65	026	358	029			-12.13 I	144.2						
	1055	65.85	147.46 <sup>+</sup>	212	179	208	12.65		-11.45 I	128.5	4.7/10	<56/39>	119.5	6	5	
1109	63.88	149.02	212	179	209			-12.34 I	149.2							

\* After flight 023, refers to latitude/longitude of intercept at 120 km of the 13-titled instruments

++ 12-channel photometer readings at maximum auroral column brightness; In zenith in flights 909, 908, & 907; Bracketed values are from narrow-field photometer

+++ K's refer to College, AK sector

\* Aircraft is turning to S 0015:30 - 0017:56

typically differ by a few degrees because of crosswinds. When the fuselage is oriented at  $180^\circ$  magnetic azimuth, the coaligned input- and output-measuring instruments point up the field lines.

The elevation angle of the center of the solar disk at the aircraft's zenith and (the directly applicable figure) at the latitude and longitude of the 120-km altitude intercept of these instrument fields follows the solar declination (also included because it is an input to the program for calculating solar elevation). Symbols D and I indicate decreasing (evening twilight) or increasing (morning twilight) elevation, to indicate whether the region had been sunlight-"predosed." The next column is the earth's shadow height (see Fig 27 of Ref 3). The tangent altitude at which  $\frac{1}{2}$  the incident solar flux is transmitted through the (1966 U.S. Standard) atmosphere is 34 km at a wavelength  $3400 \text{ \AA}$ , 45 km at  $3050 \text{ \AA}$ , and 70 km at  $2380 \text{ \AA}$  (Ref 35). To a good approximation, the minimum auroral altitude reached by half these ultraviolet photons can be found by adding their "screening" heights to the illuminated height listed in Table 4. (Note: this supersedes the definition of illuminated altitude in Ref 3.)

Column intensity ratios of optical-auroral emission features at the time in the data segment when the energy input rate is a maximum are given in the next column. Next is the altitude of peak energy deposition at this time, calculated from the  $6300 \text{ \AA}/4278 \text{ \AA}$  ratio and  $4278 \text{ \AA}$  intensity as described in Appendix II of Ref 6. In Flights 908 and 909, before the wavelength-cycling photometer's field had been directed  $13^\circ$  forward, these altitudes refer to the aircraft zenith; in the other flights they refer to the excitation in the fields of the coaligned  $0.4^\circ$  instruments.

Still incomplete in the table are the three-hour magnetic indexes K and Kp (the K's provisionally entered all refer to the College, AK sector) and the altitude in the atmosphere from which the aircraft measurement was made (available in the navigator's log). Video and photographic all-sky images of auroral excitation distribution

before and during these data segments (available but not reproduced here) are a further, and of course very important, input to the evaluation of the flight data.

The lag in SWIR radiance falloff observed in some of the enhancements is usually accompanied by a longer rise time, as might be expected from the discussion of decorrelation in the Test Plan. Additionally, a very preliminary review of the data traces in Table 4 indicates some tendency for the mean chemiluminous yield to be higher in sunlit aurora than at night. As noted, a systematic evaluation of this data base is underway.

## REFERENCES

1. A.T. Stair Jr., and J.C. Ulwick (jt ed. 's), Proceeding of the Second DNA Infrared Data Review Meeting, AFGL-TM-18 (Apr 79).
2. H.C. Fitz, Jr. (ed.), Proceedings of the DNA Program Meeting, 23-24 Jan 80, Defense Nuclear Agency, Washington, DC.
3. I.L. Kofsky and D.P. Villanucci, Further Assessment of Infrared Data from Aircraft and Rocket Probes, DNA 5127F (30 Nov 79).
4. I.L. Kofsky, D.P. Villanucci, and W.S. Andrus, Assessment of Rocketborne and Airborne Infrared Data, DNA 4731F (30 Nov 78).
5. I.L. Kofsky, D.P. Villanucci, and G. Davidson, Assessment and Evaluation of Simulation Data, HAES Report No. 69, DNA 4303F (15 Nov 77).
6. I.L. Kofsky, D.P. Villanucci, and R.B. Sluder, Data Reduction and Auroral Characterizations for ICECAP III, HAES Report No. 59, DNA 4220F (31 Jan 77).
7. I.L. Kofsky, R.B. Sluder, and C.A. Trowbridge, Data Reduction and Auroral Characterizations for ICECAP II, HAES Report No. 27, DNA 3789F (25 Oct 75).
8. W.T. Rawlins, G.E. Caledonia, J.J. Gibson, and A.T. Stair, Jr., Infrared Emission from NO ( $\Delta v = 1$ ) in an Aurora: Spectral Analysis and Kinetic Interpretation of HIRIS Measurements, J. Geophys. Res., in press.
9. D.H. Archer, Requirements for Improved Infrared Prediction Capability, HAES Report No. 78, DNA 4585F (30 Apr 78).
10. Preliminary Field Report on Nike-Hydac IR 807.57-1, AFGL, Oct-Nov 78. (The passband centers for the  $N_2^+$  First Negative 0, 1 transition are 4278 Å and 4259 Å.)
11. Range data provided by the University of Alaska Geophysical Institute (1977).
12. D. Baker (Utah State University), private communication (1977).
13. D.H. Archer (Mission Research Corp.), private communication (1976); results from MRC's ARCTIC code.

AD-A105 872

PHOTOMETRICS INC WOBURN MA

F/G 18/3

EVALUATION OF INFRARED SIMULATION DATA. (U)

NOV 80 I L KOFSKY, D P VILLANUCCI, R B SLUDER DNA001-80-C-0010

UNCLASSIFIED

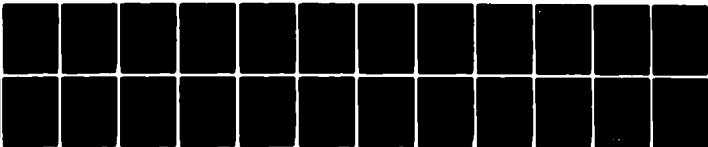
PHM-04-80

DNA-5521F

NL

2 of 2

40 A  
10-802



END

DATE

FILED

11-81

DTIC

REFERENCES (Continued)

14. R.B. Sluder and I.L. Kofsky, Photographic Measurements of Artificial Aurora Excited by Energetic Electron Beams (EXCEDE II), Final Report on Utah State University Subcontract SC-78-050 (30 Nov 78).
15. R.B. Sluder and I.L. Kofsky, Onboard Measurements of Artificial Aurora - EXCEDE: Spectral, Quick-Look Report on Results from Launch of 19 Oct 79 (09 Nov 79).
16. R.R. O'Neil et al., EXCEDE II, AFGL-TM-OPR-03 (Mar 77).
17. R.R. O'Neil, Summarized Results, EXCEDE: Spectral [1978], AFGL-TM-16 (undated), Section 7.
18. R.R. O'Neil (ed.), EXCEDE: Spectral [1979] Preliminary Results, AFGL-TM-41 (undated).
19. B.N. Maehlum et al., Planet. Space. Sci. 28, 279 (1980).
20. P.W. Tarr, Arctic Code Electron Deposition Theory with Application to Project EXCEDE, HAES Report No. 10, DNA 3636T (18 Jun 75).
21. W. Bernstein et al., J. Geophys. Res. 84, 7271 (1979).
22. R.J. Jost, H. R. Anderson, and J.O. McGarity, Geophys. Res. Lett. 7, 509 (1980).
23. G. Israelson and J.R. Winckler, J. Geophys. Res. 84, 1442 (1979).
24. I.L. Kofsky, J.D. Geller, and C.A. Trowbridge, Sky Background Measurement Program, AFCRL-70-0032 (30 Nov 69).
25. C.A. Trowbridge and I.L. Kofsky, Densitometric Analysis to Determine Artificial Cloud Expansion Characteristics, AFCRL-75-0147 (14 Mar 75).
26. B. Grandal, E.V. Thrane, and J. Trøim, Planet Space Sci. 28, 309(1980).
27. G. Israelson and J.R. Winckler, J. Geophys. Res. 80, 3709 (1975).
28. D.H. Archer, private communication (1980).

REFERENCES (Concluded)

29. W. Bernstein et al., *J. Geophys. Res.* 80, 4375 (1975).
30. J.R. Winckler, *Rev's. Geophys. Space Phys.* 18, 659 (1980).
31. I.J. Olivero, R.W. Stagat, and A.E.S. Green, *J. Geophys. Res.* 77, 4797 (1972).
32. R.H. Eather and D.L. Reasoner, *Appl. Optics* 8, 229 (1969).
33. Infrared Industries, Inc. (Waltham, MA), *Optical Filters Guide and Catalog* (1973).
34. R.B. Sluder, W.S. Andrus, and I.L. Kofsky, *Aircraft Program for Target, Background, and Sky Radiance Measurements*, AFGL-TR-79-0139 (15 Jun 79).
35. G.T. Best and N.W. Rosenberg, *Spectroscopic Studies of Barium Releases*, AFCRL-70-0724 (12 Nov 70).

## APPENDIX I

### INFRARED SKYGLOW FROM IONOSPHERE RECOMBINATION

This appendix documents a low level-of-effort followup on our measurements (Ref 3, Section 7) of an enhanced 2.8 - 3.1  $\mu\text{m}$ -band radiation background accompanying the ionospheric plasma density depletion that resulted from exhaust of  $\text{H}_2\text{O}$  and  $\text{H}_2$  molecules by an Atlas-Centaur satellite launching vehicle. The data were taken with the NKC-135A aircraft's narrow-field radiometer (Section 4) on 20 Sep 79 at the Atlantic Missile Range. The aircraft's photometer and low light level video camera also measured widespread, intense emission in the OI 6300  $\text{\AA}$  and 5577  $\text{\AA}$  lines, which serves as an indicator of the growth of the F-region plasma depletion (and of the development of any spatial irregularities in free electron density).

We interpreted this  $\sim 25$  kR maximum near-zenith intensity, 200-sec persistence airglow as 1,0 and 2,1 vibrational (Meinel) bands of the hydroxyl radical, whose upper states are the lower states of electronic ( $A^2\Sigma - X^2\Pi$ ) transitions of OH that are excited by electron dissociative recombination of  $\text{H}_2\text{O}^+$  (and perhaps  $\text{H}_3\text{O}^+$ ). The SWIR background glow originates from altitudes more than 100 km above the aurora, and is expected to extend over a  $\sim 10^{4\frac{1}{2}}$   $\text{km}^2$  area. We reported these aircraft measurements at a symposium held in November 1979. A memorandum report summarizing the results presented by others investigating the plasma depletion is on pp 97-99, with the Symposium Proceedings referenced on p 99.

Our hypothesis that the infrared radiation is a cascade effect of electronic excitation of hydroxyl can be verified by measuring the intensity and spatial distribution of emission of the electronic bands, some of which extend above the atmospheric ozone cutoff to  $\sim 3450$   $\text{\AA}$ . We suggested, therefore, that these ultraviolet measurements be made on the exhaust path of an Atlas-F thruster that was scheduled to

launch a NOAA satellite on 21 May 1980. We also reviewed the applicability of a dedicated rocket release of  $H_2O$  and  $CO_2$  molecules planned for April 1980, concluding that measurements from the aircraft would not be cost-effective. A memorandum report on the releases from the satellite-launching and sounding rockets is reproduced on pp 100-101.

As the aircraft platform was not committed for the 21 May 80 release event, we assembled a UV-sensitive camera for use at a ground station. Staff of Boston University's astronomy department operated the camera (under DOE sponsorship) at Mt. Palomar Observatory, CA, which afforded a good view of the depleted volume of ionosphere over the Pacific Ocean. The background material for measurements of the UV glow's growth, persistence and spectrum, which at our request was also distributed to other appropriately-located astronomy observatories, is on pp 102-103. A checklist for the field operation with a full description of the camera system is on pp

Launch of the satellite from Vandenberg AFB was delayed eight days, by which time the full moon had come directly into the camera's field. Moonlight scattered in the lens (principally) and atmosphere increased the film background to a level at which no depletion-associated enhancement is readily detectable, as reported on p 107. We note that the aircraft could have been positioned to view the trajectory without the moon in the camera field.

Several similar launches scheduled for the next few years provide a further opportunity to investigate the processes that produce infrared, visible, and UV sky background enhancements that result from injection of reactive molecular species into the F region. Additionally, the Firewheel releases of barium and lithium atoms in the magnetosphere, whose applications to nuclear-effects simulation are reviewed in Appendix III of Ref 4, are forthcoming (refer to page 107).



MEMORANDUM

DATE: 5 December 1979  
TO: P. Lunn, H.C. Fitz, Jr., DNA/RAAE  
FROM: I.L. Kofsky, PhotoMetrics, Inc.  
SUBJECT: Workshop/Symposium, "Preliminary Evaluation of Ionospheric Disturbances Associated with HEAO-C Launch with Applications to the SPS Environmental Assessment", 12-13 November 1979, North Andover, MA.

The symposium was organized for the Solar Power Satellite Office of DOE (Argonne Nat'l Lab) by Prof. Michael Mendillo of Boston University, who was among the group that recognized and publicized the ionosphere hole made by the Skylab launch by a Saturn V. It was held at BU's conference center, some 25 miles north of Boston. DOE is interested in the environmental effects - on the troposphere and stratosphere as well as the ionosphere - of the heavy-lift launch vehicles that would be needed to construct SPS in geosynchronous orbit.

The program and list of participants is referenced below; much of ionosphere-depletion community was represented. Mendillo and AFGL (J. Klobuchar) had coordinated the field measurements on the 20 Sep 79 ionosphere disturbance produced by the exhaust gases from the Atlas-Centaur rocket that put HEAO-C into orbit. It's my understanding that individual experiment groups (listed in the program) paid their own way.

We were invited to present the optical/IR results from the DNA/AFGL aircraft mission, in particular our video film of the 6300 Å depletion glow. The all-sky pictures and other photometry-radiometry data created a big stir at the symposium - we got compliments from several quarters, and urgent requests to locate and size the depleted plasma volume.

-----  
A preliminary report of these data, with a brief review of the major results reported by other ionosphere-diagnostics groups, is in Section 7 of PhotoMetrics' Report 5127F, 30 Nov 79.

Here are some of the findings about the ionosphere depletion that may apply to technical questions of interest to RAAE.

- 1.a) The column electron content of the ionosphere through the hole, measured by a network of polarimeters, decreased by a factor 5 in less than 5 min.

- 2 -

- b) At the F-layer peak the volume electron density, measured by the incoherent-scatter radar at Millstone Hill, decreased by a factor about 10.
  - c) The depletion extended out a couple of hundred km from the release trail, and
  - d) persisted until at least an hour before dawn. Pre-sunrise restoration of the F-region measured from two of the polarimeter sites is not explained.
2. a) The polarimeters detected no phase scintillations that would result from spatial structure (of about 10 km scale size).
- b) A preliminary review of the video camera and zenith photometer results also indicates that the depletion volume was "smooth" (to  $\sim 1$  km scale). Analysis of these optical data is incomplete, and we'd like to take a closer look for structure (as discussed in Section 7 of 5127F).
3. a) Some fading at HF was measured, but the effects were not pronounced.
- b) Some signal fluctuations, tentatively interpreted as due to multipath, were seen by differential doppler measurements using Transit satellites.
  - c) Some oddities in VLF phase were also reported (by United Aircraft, using the Omega system).
4. a) The intensities of the O-atom glows were about an order of magnitude greater than predicted.
- b) The afterglow, which measures the column rate of recombination of the ionosphere plasma, grew to fill about half an all-sky frame, with
  - c) a low-contrast hole in the middle where most of the free electrons had already been lost.
5. a) Population of vibrational states of OH above the ninth, which was thought to have been seen at

Lagopedo, was not detected. (This earlier report was verbally retracted at the Workshop.)

- b) An enhancement of the airglow background in the 2.8-3.1 $\mu$ m band was measured by the aircraft's radiometer; the effect is discussed in detail in 5127F. (It has applications to EXCEDE and to some surveillance-system observations.)

-----

The fact that no pronounced irregularities developed in the  $\sim$ 5 hr before the electron density was restored by solar photons, provides at least some sort of bound for ionosphere-dynamics calculations. Plans are being made (by Mendillo and others) for a release of H<sub>2</sub>-H<sub>2</sub>O-CO<sub>2</sub> from Space Shuttle over the Jicamarca incoherent-scatter radar, where the earth's magnetic field lines are nearly horizontal and post-sunset natural inhomogeneities appear regularly, and where NRL's calculations of plasma instability development (Memorandum Report 3940, 3769, 3604, for example) apply.

References: Proceedings of the [11-13 Nov 79] Workshop Symposium on the Preliminary Evaluation of the Ionospheric Disturbances Associated with the HEAO-C Launch, with Applications to the SPS Environmental Assessment (ed. M. Mendillo and B. Baumgardner), Department of Energy Conf-7911108, Aug 1980.

M. Mendillo, D. Rote, and P. A. Bernhardt, Preliminary Report on the HEAO Hole in the Ionosphere, EOS 61 #28, 8 July 80.

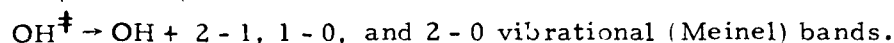
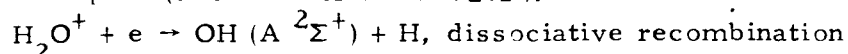


MEMORANDUM

DATE: 28 January 1980  
TO: A.T. Stair, Jr, E.R. Huppi  
FROM: I.L. Kofsky  
SUBJECT: Ionospheric Plasma Depletions, Spring 1980

Releases of molecular gases that recombine the F-region's free electrons are planned by NASA (Atlas-F rocket launch from Vandenberg, 21 May) and NRC-Canada (100 kg of high explosive, 300 km over Churchill, moon-down window opens 02 April). I'd recommend that the aircraft make IR/Optical measurements on the persisting skyglows from the NASA release cloud, but not at the Canadian experiment. Particulars follow.

1. NASA rocket exhaust. The major purpose would be to verify the mechanism that I proposed for the unexpected  $\sim 20$  kR  $2.8 - 3.1 \mu\text{m}$ -band enhancement that resulted from the Atlas-Centaur launch of 20 Sep 79 (Section 7 of DNA 5127F):



We'd measure the UV emissions principally with the aircraft's cameras, as there isn't time to organize a high-standard spectrometer and imaging system. The results apply to interpreting  $2.8 \mu\text{m}$  earth limb data, and also to EXCEDE's observations of water vapor emissions.

As noted in 5127F, similar ionosphere depletions near the geomagnetic equator are planned using Space Shuttle; these are expected to generate F-region plasma irregularities of the type described by S. Ossakow at the 23-24 Jan 80 DNA Program Meeting. In view of the fact that these inhomogeneities produce important LWIR and SWIR spatial structure (not to mention VHF-UHF scintillations), it would be prudent to understand the phenomenology of the molecule releases. And in view of the fact that plasma emissions are thought by some theoretical groups to be the dominant LWIR background, I would expect that the nuclear-effects and phenomenology community would be actively interested in the equatorial "plumes." In this regard, it is worth noting that a large rocket exhaust trail is a potential active mitigant of the persisting free-electron overdensities predicted by the late-time disturbed F region codes.

The Atlas-F is now scheduled for 1053 UT (3 AM local) in a near-vertical trajectory from Vandenberg AFB, CA, burning RP-1 (kerosene)



with LOx to 435 km altitude. Major expected exhaust gases are H<sub>2</sub>O (31½ mol %), H<sub>2</sub> (11%), OH (4½%), CO (35%), and CO<sub>2</sub> (12½%). As the engine exhausts 121 kg/sec of these gases, the column intensities in the optical/IR depletion glows should be at least as high as from the Atlas-Centaur. The rocket will place in orbit a replacement NOAA-B weather-and-environment satellite; I'm told (through AFGL) that postponements of this type launch are common. I'd want the aircraft to stay on station through dawn - an hour or two later - to measure the effect of solar radiation on the emissions from the partially-depleted ionosphere.

2. NRC explosive release: "Water Hole." This is a Lagopedo-like explosion at 300 km, which produces mainly H<sub>2</sub>O and CO<sub>2</sub> along with some N compounds. The plasma depletion is expected to a) increase the kinetic energy of the auroral particles, making them penetrate 5-10 km lower in altitude (LASL speaking) or b) "shift" and introduce instabilities in the auroral precipitation distribution (NRC speaking). Launch conditions are an IBC I<sup>+</sup> (or more intense) arc located where the depletion cloud can be placed on its field lines, >10° solar depression, no moon, and good visibility from ground sites at Fort Churchill and Gillam, Manitoba.

Like Lagopedo, the experiment will have a mother-daughter configuration: release from the rocket's forward section, in situ diagnostic measurements from a previously-separated pod. (The best description is in JGR 84, 4393 (01 Aug 79)). Los Alamos (John Zinn, Morris Pongratz) is building the nitromethane-ammonium nitrate explosive canister for National Research Council-Ottawa (Project Scientist is Bryan Whalen, 613-992-2734, modeler Andrew Yau). The ground sites will have monochromatized image intensifiers, photometers, and radio receivers (I don't have particulars on these). LASL will be contributing to the groundbased measurements.

I'd expect the cost of making aircraft measurements on Water Hole would be prohibitive in comparison to the value of the information returned, considering that the decision to launch the rocket is made à la ICECAP: - rocket up on the pad every night. Hence my recommendation, No action.

-----

On the other hand the NASA launch decision can be expected to be firm a day or so before (last-minute equipment failures excepted), so only one flight mission would be needed. The aircraft has enough range to fly out of Pease, remain on-station through 10° solar depression just west of Vandenberg (1205Z, 0405 local standard time), and land at one of the southern California USAF bases for refueling. TEAL RUBY measurements are now tentatively planned for 13-23 May from Fairchild AFB, WA; if this flight program materializes, the data flight could easily be made from Fairchild, which is less than two flight hours from the Western Test Range.



442 MARRETT ROAD, LEXINGTON, MASSACHUSETTS 02173 • (617) 862-8050

DATE: 28 February 1980  
 TO: Jeff Baumgardner, Boston University  
 FROM: I. L. Kofsky, PhotoMetrics  
 SUBJECT: Expected Ultraviolet Airglow from 21 May 80 Atlas-F  
 Rocket Exhaust: Measurement Recommendations

### Background

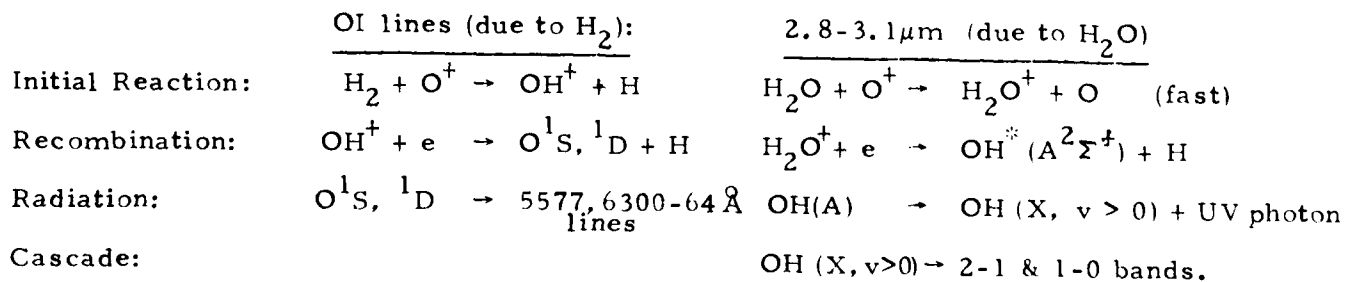
A major unexpected effect accompanying the ionospheric plasma depletion caused by the H<sub>2</sub>-H<sub>2</sub>O trail release from the 20 Sep 79 Atlas-Centaur engine was the persisting, ~20 kR increase in the 2.83-3.14 μm near-zenith radiance measured from a USAF NKC-135 A atmospheric research aircraft. The original data in two infrared bands, along with some of those on the shorter-wavelength airglows measured by zenith-pointing photometers, are in DNA 5127F, Section 7.

For the reasons outlined below, I believe this infrared glow to be rotation-vibration (Meinel-band) radiation from OH molecules. This hypothesis can be tested by measuring the spatial and spectral distribution of UV radiation in hydroxyl electronic bands, whose lower states would be the upper states of the vibrational transitions.

### Model

The fact that the time dependence of the 2.83-3.14 μm enhancement follows closely the as-expected OI green (and red) line afterglow (Fig 40 in 5127F), strongly suggests that it is also associated with an electron loss process. The data from the other radiometer and photometers (Fig's 38, 39) fail to show a discernible increase in radiation originating from  $v > 3$  of the ground electronic state of hydroxyl. On the other hand, the 2.83-3.14 μm-band enhancement (Fig 39) could be due to the OH 3-2, 2-1, and/or 1-0 transitions.

Here is what I believe is happening (e and O<sup>+</sup> are ambient in the F-region, the rocket releases 7 kg/km of H<sub>2</sub>O and ½ kg/km of H<sub>2</sub>): -



That is, the low-lying vibrational states of OH are indirectly populated following emission of the well-known A-X electronic bands. (Dissociative recombination of  $H_2O^+$  is  $7\frac{1}{2}$  eV exothermic, while the zeroth vibrational level of the OH A state is at  $4\frac{1}{2}$  ev.) The tabulation in Gaydon & Pearse (The Identification of Molecular Spectra, Chapman and Hall, London 1965, p247) shows that 1/3 of the A-X photons in the laboratory "[seen] from almost all sources where water vapour is present") are from transitions that terminate in  $v' = 1$  or 2. While the laboratory excitation mechanisms may not be the same as the one we have proposed for the ionosphere, the infrared cascade should be to a large extent independent of how the  $A^2\Sigma^+$  state was populated.

### Suggested Measurements

This selective excitation process could be verified by UV spectrophotometry of the Atlas-F depletion afterglow. The principal A-X bands transmitted by the earth's ozone layer are the 1-1 near 3125 Å, 2-2 near 3190 Å, and 0-1 near 3450 Å. Transmission by 0.25 atm-cm of  $O_3$  at the two shorter wavelengths is 0.61 and 0.81, and even at the strong 0-0 band near 3060 Å - which in any case does not contribute to infrared emission - it is about 0.25. Since the radiating source covers a wide angle of sky, Rayleigh outscatter by air molecules is to some extent compensated by in-scattered photons. The total peak transmitted OH electronic bands intensity should be of the order of 10 kilorayleighs.

Spectra of the glow at these wavelengths near the atmospheric ozone cutoff would be most desirable. Images of the UV glow, with time resolution  $\sim 10$  sec if possible, would also be extremely useful. High spatial resolution isn't necessary, as little if any structure is expected. Filter photometry in any of these electronic bands would also be desirable.

If the process proposed above is substantially correct - or even if the  $e + H_2O^+$  reaction directly populates vibrational states of OH - the growth rate and extent of the UV-IR glow should be somewhat smaller than the component of the OI (red and green line) glow due to  $H_2$ , because the  $H_2O$  molecules have slower outward diffusion-transport than the  $H_2$  molecules. On the other hand the  $H_2O$  moves outward more rapidly than  $CO_2$  exhausted from the rocket, which also produces OI radiation through the reactions  $CO_2 + O^+ \rightarrow CO + O_2^+$ ,  $O_2^+ + e \rightarrow O^1S, D + O$ . Figure (from experience with the Atlas-Centaur) on an initial UV glow about  $\pm 10^\circ$  from the rocket trajectory, expanding to  $\pm 35^\circ$  as it weakens.

If possible data should be taken through dawn at the radiating altitudes, or better still, until scattered sunlight washes out the optical measurements. A checklist for UV photography from Mt. Palomar is attached.

## PROGRAM FOR UV CAMERA

---

THIS IS A 35MM FORMAT CAMERA - A NIKON SP - EQUIPPED WITH AN ULTRAVIOLET TRANSMITTING LENS AND FILTER. IT HAS A MECHANICALLY OPERATED FOCAL PLANE SHUTTER, A FIXED IRIS AND REQUIRES NO BATTERIES OR OTHER POWER SOURCES . IT IS DESIGNED TO RECORD EMISSION FROM THE 0-1, 1-1 AND 0-2 A-X ELECTRONIC BANDS OF OH BELOW 346 NM.

WE EXPECT THIS RADIATION TO BE PRESENT ON THE BASIS OF OUR OBSERVATIONS/INTERPRETATION OF OH INFRARED (2800 NM) EMISSION WHEN THE EXHAUST GASES OF THE 20 SEPT 79 CENTAUR REACTED WITH THE IONOSPHERE. IF SO, WE'D HAVE SOME EXCELLENT NEW INFORMATION ON THE OH\* EXCITATION RATE COEFFICIENT IN  $E + H_2O^+$  REACTIONS AND A "MAP" OF  $H_2O-H_2O^+$  DIFFUSION. IF NOT, THE IR RADIATION IS PROBABLY THERMAL FROM PARTICULATES, SO WE'D HAVE DATA TO CHECK BERNHARDT'S MODEL OF PARTICLES FORMATION IN THE CENTAUR EXHAUST. IN EITHER CASE THE INFORMATION IS VALUABLE TO BOTH THE DOE-SPS/ENVIRONMENT AND DOD LAUNCH VEHICLE SURVEILLANCE COMMUNITIES.

**\*\*OPTICS\*\*** THE LENS IS A SIMPLE BICONVEX LENS OF FUSED SILICA, 25 MM FOCAL LENGTH. THE APERTURE IS FIXED AT F/1.1. THE EXTREME EDGES OF THE FIELD OF VIEW ARE 80(HOR) X 68(VERT) DEGREES, ALTHOUGH REASONABLY SHARP IMAGES ARE OBTAINED ONLY WITHIN THE CENTRAL 40 DEG.

A UV TRANSMITTING FILTER - 3MM THICK SCHOTT GLASS UG-11 - IS LOCATED DIRECTLY IN FRONT OF THE LENS. ITS FWHM PASSBAND IS APPROX. 270 - 370 NM, PEAK TRANSMISSION 70%; VIRTUALLY ALL OF THE VISIBLE EMISSION IS ABSORBED. WE DON'T EXPECT ANY EMISSIONS BETWEEN 346 AND 380 NM TO CONFUSE OUR MEASUREMENT OF OH ELECTRONIC BANDS EMISSION.

**\*\*FILM\*\*** THE EMULSION USED IS EASTMAN KODAK 2475 - A HIGH SPEED BLACK & WHITE FILM. IT IS PACKAGED IN ORDINARY 35MM FILM CARTRIDGES, NO PROBLEM IN RELOADING.

**\*\*POINTING\*\*** THE CAMERA SHOULD BE MOUNTED ON THE TRIPOD (SUPPLIED) AND SET TO ELEVATION 50 DEG, AZIMUTH 225 DEG TRUE, +/- 1 DEG, FROM PALOMAR. THE CAMERA BODY CAN BE USED AS A REFERENCE SURFACE FOR ALIGNMENT, AT THIS ACCURACY. REFER TO THE ATTACHED DIAGRAMS OF THE EXPECTED ANGULAR EXTENT OF THE GLOW. NOTE: YOU PROBABLY WON'T BE ABLE TO DETECT IT VISUALLY. IN ANY CASE, THE GLOW WE'RE LOOKING FOR WOULD HAVE 1/3 THE EXTENT OF A GLOW WHOSE PRODUCTION IS DOMINATED BY DIFFUSION OF H2 MOLECULES.

**\*OPERATION\*** THE CAMERA AS DELIVERED HAS 2475 FILM IN IT, SO IT IS NOT NECESSARY TO LOAD THE CAMERA PRIOR TO LAUNCH. EXPOSURES ARE MADE BY SETTING THE SHUTTER SPEED CONTROL TO "B" (BULB) AND HOLDING THE SHUTTER RELEASE BUTTON DOWN FOR THE REQUIRED EXPOSURE DURATION.(A CABLE RELEASE IS SUPPLIED TO MINIMIZE CAMERA VIBRATION.) THE SHUTTER IS COCKED AND FILM ADVANCED BETWEEN EXPOSURES BY MANUALLY OPERATING THE FILM ADVANCE LEVER. PLEASE BE CAREFUL TO MINIMIZE DRIFT OF THE FIELD BY STEADYING THE CAMERA WHEN YOU ADVANCE FILM.

A BRIEF PRE-LAUNCH CHECKLIST:

- \* ACCURATE WATCH, LIGHT TO SEE IT, CHECKLIST
- \* READ INSTRUCTIONS TO RELOAD FILM
- \* POINTING, 50 DEG EL, 225 DEG AZ
- \* SHUTTER SPEED, SET ON "B"
- \* ADVANCE/REWIND SWITCH, SET TO ADVANCE ("A")
- \* FOCUS SETTING, SET TO INF. ("OO")
- \* SHUTTER, COCK FOR FIRST EXPOSURE.
- \* CABLE RELEASE, ATTACHED.
- \* LOCAL FLOURESCENT LIGHTS OFF!
- \* EYES, DARK ADAPTED

\*\*\*\*\* EXPOSURE SEQUENCE \*\*\*\*\* ROLL 1

TWO FRAMES WILL BE EXPOSED BEFORE LAUNCH TO ESTABLISH A BACKGROUND LEVEL. BEGINNING 180 SEC AFTER LAUNCH, TWO FRAMES PER MINUTE WILL BE TAKEN, ALTERNATING 10SEC AND 30 SEC EXPOSURE TIMES, WITH 10SEC INTERVALS TO ADVANCE THE FILM. THIS GIVES TWO FRAMES PER MINUTE.

FRAME #	TIME, START	DURATION	DONE
1	LAUNCH-5MIN	10SEC	< >
2	-4MIN	30	< >
3	LAUNCH+180 SEC	10	< >
4	200	30	< >
5	240	10	< >
6	260	30	< >
7	300	10	< >
8	320	30	< >
9	360	10	< >
10	380	30	< >
11	420	10	< >
12	440	30	< >
13	+8 MIN 0 SEC	10	< >
14	8 20	30	< >
15	9 0	10	< >
16	9 20	30	< >
17	10 0	10	< >
18	10 20	30	< >
19	11 0	10	< >
20	11 20	30	< >
21	12 0	10	< >
22	12 20	30	< >
23	13 0	10	< >
24	13 20	30	< >
25	14 0	10	< >
26	14 20	30	< >
27	15 0	10	< >
28	15 20	30	< >
29	16 0	10	< >
30	16 20	30	< >

CONTINUE TILL FILM WON'T ADVANCE --  
10 SEC EXPOSURE ON THE MINUTE, 30 SEC EXPOSURE 20 SEC PAST THE MINUTE.

WRITE DOWN THE TIME OF LAST FRAME <      >.

THE MOST CRITICAL DATA IS IN THE FIRST 18 MIN. THE UV GLOW RADIANCE WILL MOST LIKELY BE BELOW EXPOSURE THRESHOLD BY THIS TIME. NONETHELESS, CONSIDERING ALL THE UNCERTAINTIES AND THE POSSIBILITY OF A SUNLIGHT ILLUMINATION EFFECT, WE'D LIKE TO CONTINUE THE MEASUREMENTS PROGRAM THROUGH DAWN AT 200KM (14DEG SD) AT LEAST.

..... REWIND FILM, INSTALL NEW ROLL AS OUTLINED BELOW, ADVANCE THREE FRAMES; WRITE DOWN TIME AT START <      >.

MAKE A SERIES OF 60 SEC EXPOSURES, WITH A 60 SEC INTERVAL TO ADVANCE FILM. THAT IS, ONE EXPOSURE EACH 2 MINUTES. THIS WILL TAKE THE MEASUREMENTS THROUGH DAWN AT THE RADIATING ALTITUDES (AND BELOW).

RELOADING INSTRUCTIONS-----

- 1) REMOVE CAMERA FROM TRIPOD
- 2) TURN RING SURROUNDING SHUTTER RELEASE FROM "A" TO "R"
- 3) REWIND FILM FULLY INTO CARTRIDGE
- 4) INSTALL NEW FILM (THE LITTLE BLACK CYLINDER GOES DOWN; THE TAKEUP SPOOL WORKS BACKWARD FROM WHAT YOU MAY EXPECT)
- 5) REASSEMBLE, RETURN RING TO "A"----- GO!

##### INVENTORY #####  
CAMERA, NIKON SP, S/N 6220480  
LENS/FILTER ASSEMBLY (ON CAMERA)  
CABLE RELEASE  
TRIPOD  
5 ROLLS 2475 FILM, RE135-36  
GLOW DIRECTION PLOTS (2)  
PROGRAM/INSTRUCTIONS/CHECKLIST (3 COPIES)

##### QUESTIONS, EMERGENCIES: #####

RANDALL B SLUDER      (617) 861-7540  
IRVING L KOFSKY      (617) 235-1014  
PHOTOMETRICS      (617) 862-8050



MEMORANDUM

DATE: 17 June 1980  
TO: P. Lunn, DNA/RAAE  
FROM: I.L. Kofsky, PhotoMetrics  
SUBJECT: Status of "Target of Opportunity" Upper-Atmospheric  
Chemical Releases

1. ATLAS-F (trail release of H<sub>2</sub>, H<sub>2</sub>O, CO<sub>2</sub> in the F-region → ionosphere plasma depletion and airglows; for applications to nuclear-effects simulation see Section 7 of DNA 5127F.)

PhotoMetrics had loaned Boston University astronomy department (Mendillo/Baumgardner) a 35 mm camera with simple ultraviolet lens and filter, for photographing the expected widespread glow in the hydroxyl electronic bands. B. Baumgardner operated the camera as per an exposure and pointing schedule we provided, from Mt. Palomar Observatory looking W toward the ionospheric release region S of Vandenberg AFB (BU/DOE paid all expenses).

Launch was delayed 8 days, by which time the full moon had come directly into the field of view. (Los Alamos was able to relocate their optical instruments N of WTR, to avoid direct moonlight irradiation.) Moonlight scattered in the atmosphere and camera resulted in the high film density of ~0.8 in the expected afterglow image area. No glow image has been detected in a preliminary visual inspection of the 2 rolls of 36 exposures through local dawn. If a more careful look fails to show a glow pattern, an upper limit to the brightness can be established.

This launch vehicle failed to place its payload in orbit. A replacement launch is planned for November 1980, also from WTR, as per 14 June Science News story. BU uncertain whether they'll have funds to send technical personnel.

2. FIREWHEEL (Ba (and Li) at ~9 earth radii → artificial aurora; for nuclear-effects simulation applications see Appendix III of DNA 4731F).

Launch on an Ariane rocket 23 May also failed. Replacement status uncertain, as per 9 June Aviation Week story. Note: a winter launch would result in measurable artificial aurora in Alaska, as noted in 4731F.

APPENDIX II  
MEMORANDUM

DATE: 1 July 1980

TO: Memo for Record - 1010 FROM: I. L. Kofsky

SUBJECT: DNA-AFGL Nuclear Weapons Effects Chemistry  
Conference, 26-27 June 1980

The meeting was organized by M. Bortner of GE-Valley Forge (early planning stages) and K.S. W. Champion of AFGL (final arrangements). Conferences with the similar purpose of reviewing the chemistry of deionization (primarily) and excitation-deexcitation of infrared had been run by Dr. Champion since about 1960, with most of the focus on laboratory work. The lag since the last one reflects the decreased activity in this field.

Capt. P. Lunn represented DNA/RAAE. There were 43 attendees at 1216 on 26 June, 48 at 1000 27 June; about half were from AFGL.

Major topics were D-region positive and negative cluster ions; reaction rate coefficients appropriate to the E region and the heated F region; sensitivity of radiowave propagation and infrared emission models to chemical reaction rate coefficients; kinetics and specific reactions of  $\text{NO}^{\pm}$  and  $\text{NO}$ ; structure of the  $\text{NO}_2$  molecule;  $\text{CO}_2$  emission processes; interpretation of EXCEDE data; the "primary" species produced when air is bombarded by energetic charged particles; and results from and plans for COCHISE and LABCEDE. Critical new ideas include the presence of  $\text{Cl}^-$  ions in the D region (not everyone believes these measurements) and hydrated  $\text{Na}^+$  ions at stratospheric altitudes; the anticorrelation of  $[\text{NO}]$  and T in the lower thermosphere, due to the fact that  $\text{NO}$  molecules are important radiators (through the  $\text{NO}' + \text{O} \rightarrow \text{NO}^{\pm} + \text{O}'$  reaction seen in several HAES investigations); the variability of the O-atom profile, as measured from rockets by the method of resonance scattering of the  $1304 \text{ \AA}$  OI triplet; the discrepancy between HIRIS II measurements of a collisional relaxation-dominated  $\text{NO}$  vibrational fundamental band spectrum and the generally-accepted model for depopulation of  $\text{NO}^{\pm}$  in the atmosphere; the related discrepancy between the small auroral yield of  $\text{NO} \Delta v = 1$  photons measured by HIRIS II and the large yields of  $\Delta v = 2$  photons "seen" by several HAES rocket and aircraft radiometers; and the application of EXCEDE to clarifying optical emission processes in the upper atmosphere.

One classified paper was given on the emissions from the E and F-region following the high-altitude nuclear explosion Starfish. I was pleased to find that NRL's large-scale MHD codes verify our earlier ideas on the mechanism that causes persisting and widespread atmospheric emission in the UV, visible, and near IR (in AFCRL-66-443, June 1966). Additionally, the time dependence of the two principal radiations checks with the measurements we made from Maui and the distant aircraft station with wide-angle photometers (in Project 8A.1).



Session I. - D-Region. The material presented in this session reflects an increasing interest in the lower D region of the ionosphere, extending into the stratosphere (this is sometimes called the C region). The old problems of negative ion chemistry remain largely unsolved. Field data from both total solar eclipses - rapid shutoff and turnon of photodestruction -, and solar proton events - increased ionization rates -, were presented. The 1972 SPE results on reduction of  $[O_3]$  suggest that in the stratosphere as many as 2 NO molecules are produced per ion pair. (The number for the E region is usually taken as 1.5, 0.9 from direct impact dissociation of  $N_2$  and 0.6 in subsequent chemical reactions.)

Session II. - E- & F-Regions. Papers on reaction chemistry from the longstanding laboratory groups: Pittsburgh, NOAA, AFGL/LKB, SRI, and from the UT theoretical group. Two papers covered the sensitivity to rate coefficients of communications from ELF through UHF-SHF. The results, some of which were obtained by committee, are not readily summarizable. The main clear conclusion seems to be that the characteristic time for the various F-region propagation effects to die off varies between 1.7 and 2.7 hr, depending on rate coefficients at the high temperatures predicted by the magnetohydrodynamics-chemistry (phenomenology) codes. The time constants depend also on the altitude profile of concentration of  $O_2$ , which is known to vary naturally.

The paper on EMP-lightning effects near low-altitude fireballs highlighted the extreme complexity of high-pressure air chemistry. Some of the ideas on ion recombination and formation of new species also apply to propagation of high-intensity particle beams through the atmosphere.

Session III: - Infrared. A paper (by Champion) reviewing systematic variability of the mesosphere and thermosphere, as presented at the COSPAR meeting earlier in June, served as background. Its principal direct bearing on nuclear explosion-excited infrared emission is the inverse correlation between temperature and mean NO concentration in the high-latitude lower thermosphere, over a solar cycle. This is due to the fact that solar activity changes the interplanetary and geomagnetic field, which in turn determines the flux into the atmosphere of incoming charged particles, whose ionization leads to dissociation of air and thus production of NO; this species plays an important part in the energy budget of the upper atmosphere, as it radiates  $5.3\mu m$  photons following the exchange (thermal) reaction with O. As noted, the  $NO + O \rightarrow NO^+ + O'$  process was identified in DNA's HAES program, and plays a prominent role in interpretation of SWIR radiation data.

AFGL's new capability for high-quality direct measurement of  $[O]$  profiles will no doubt be extremely useful in future rocket-based nuclear effects simulation investigations. (As is well known, oxygen



atoms play an important part in  $\text{NO}^{\pm}$  chemistry: they quench  $\text{NO}^{\pm}$  and its major precursor  $\text{N}^{\pm}\text{D}$ , and they react with  $\text{N}_2^+$  to make  $\text{NO}^+$ .) The VUV data presented by R. Huffman of AFGL are also in his group's recent paper in *Journal of Geophysical Research* 85, 2201 (1 May 80). Their measurements of UV emission intensities looking downward from a low altitude orbiting satellite by day may contain useful information about the natural variability of species concentrations in the upper atmosphere (complementing R. Philbrick's mass-spec data).

As noted, the data from HIRIS II are at variance with the currently-accepted DNA/DoD model of excitation and de-excitation of  $\text{NO}(v)$  at altitudes near 110 km. First, the measured spectrum fits a collisional-depopulation scheme, while the conventional wisdom is that there aren't enough O atoms (or other reactive species) to depopulate in competition with the radiative cascade. Second, the HIRIS yield of fundamental-band photon energy is  $1\frac{1}{4}\%$ , while theory predicts about 3%. Meanwhile, the overtone-band intensity measured with radiometers on aircraft and sounding rockets averages  $\sim 0.6\%$ , which fits a model with negligible collisional relaxation of  $\text{NO}(v)$  molecules.

A. T. Stair described some aircraft observations of auroral particle-associated 2.8-3.1 $\mu\text{m}$ -band emissions at twilight, which are anomalous in that the radiation is much more "smeared" ( $\sim 6$  sec delay) than that from the dark upper atmosphere ( $\lesssim 2$  sec). We have been looking into possible origins of this phenomenon, so far without success: neither day-night changes in the ambient auroral-latitude atmosphere or the flux of solar photons is able to account for the reported difference in grow-in and decay time. (PhotoMetrics was co-author of Stair's presentation.)

EXCEDE: Spectral (Oct 79) produced some technically very interesting and potentially useful results. The data are an excellent source of information on collisional quenching of various atmospheric emission features, for example. Evaluations of spectroscopically-measured  $\text{CO}_2$  and  $\text{NO}$  emission, and of  $\text{NO}^+$  (or  $\text{N}_2\text{O}$  or  $\text{CO}$ , or whatever is radiating 4.4 to 4.6 $\mu\text{m}$ ), need better information on energy deposition volumes; both papers made ad hoc assumptions about the optical path length through the particle excited volumes. These energy-input and geometric data are available in our onboard photographs of the air fluorescence.

J. Kumer (LMSC) updated the suggestion he had made at the April 1979 HAES IR Data Review that some 4.3 $\mu\text{m}$  emission measured from IC807.15-1, which penetrated an auroral arc, is "prompt." He highlighted his talk by comparing power spectral densities of spatial variations at 4.3 $\mu\text{m}$ , assuming a fast mechanism operative above 115 km altitude, with those at 2.7 $\mu\text{m}$ .



Session 4: - Excited State Chemistry. This session led off with another sensitivity paper, this one of the sensitivity of IR background radiances to chemical rate coefficient parameters. Results again are not readily summarized in a brief review.

F. Gilmore updated the theory of production of excited (and ionized) states in air by charged particles and (x- and  $\gamma$ -rays) from nuclear explosions. He made the point that some heretofore-unexpected emitters tend to fill in the wavelength gaps between the bands from the known radiating species. These include OH (as H from dissociated  $H_2O$  reacts with  $O_3$ ) and CO ( $10^{-2}$  molecules produced per ion pair).<sup>2</sup> Gilmore judged that he has not yet carried his calculations far enough.

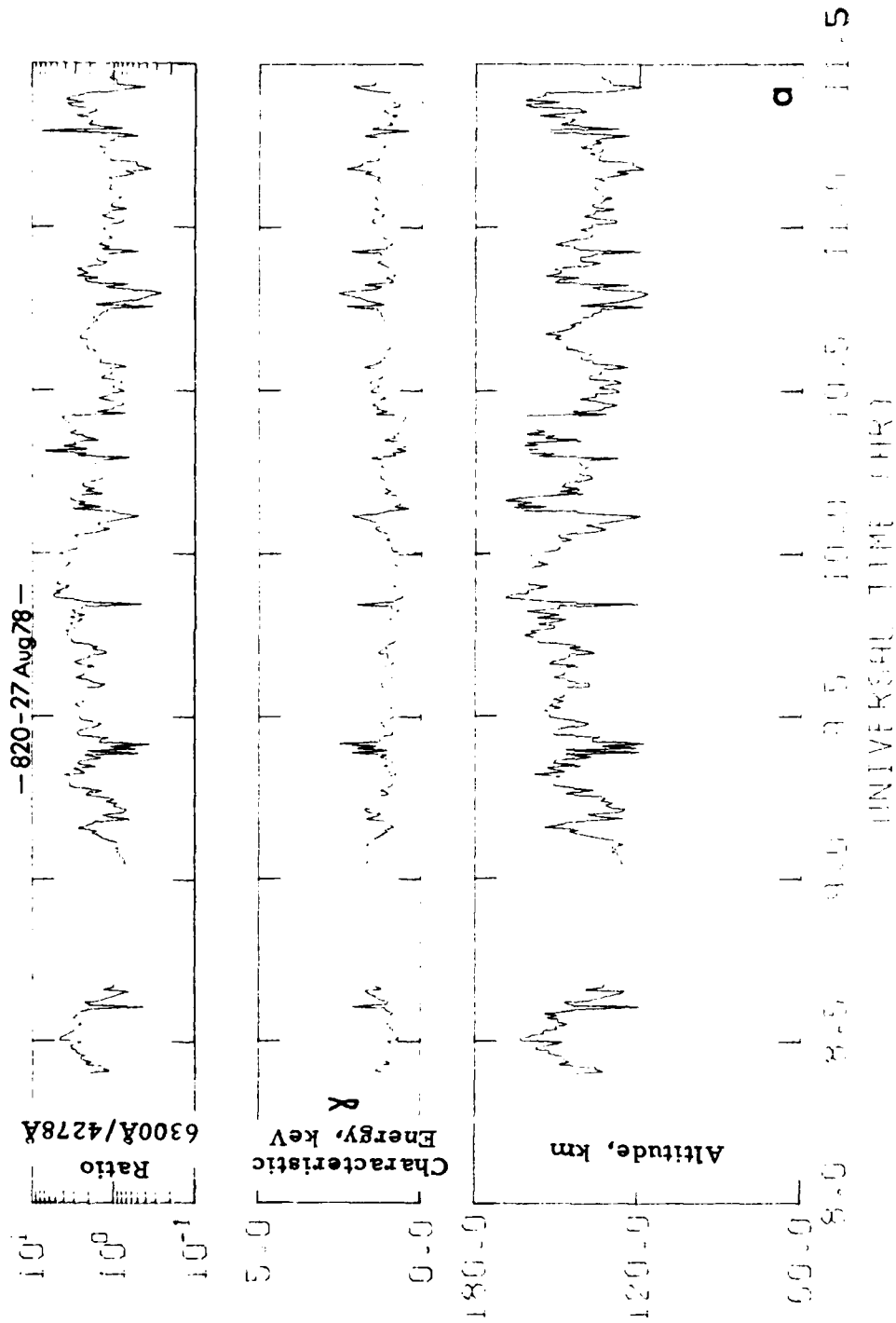
The presentations on LABCEDE and COCHISE included the information given at recent DNA conferences. Prof. F. Kaufman spoke on the complexities of the  $NO_2$  molecule, and on laboratory measurements on reactions of  $N_2^D$  with  $O_2$  and O,  $N_2^P$  with  $O_2$ , and  $N_2(A)$  with  $O_2$  and O. He does not expect much  $NO^+$  to result from the reaction of  $N_2(A)$  with O atoms.

As noted, the meeting focused on more or less basic chemistry issues rather than immediate applications to nuclear effects simulation. The major exception was the papers on sensitivity, whose intent is to identify reaction processes that require further investigation.

## APPENDIX III

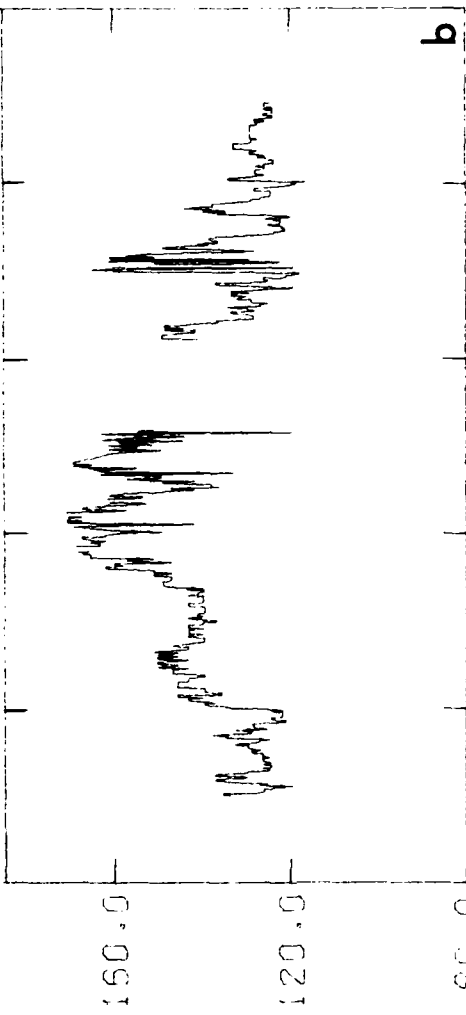
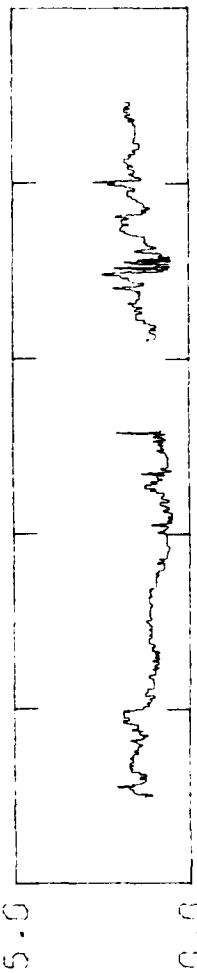
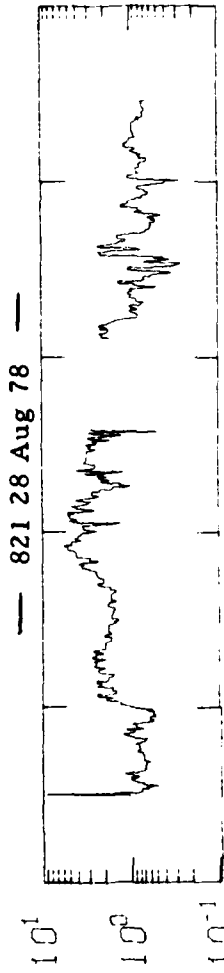
### AURORAL ALTITUDES

The altitude of maximum particle-energy deposition rate and incident-electron spectral index  $\alpha$  (Appendix II of Ref 6) during the four 1978 auroral flights from which 2.8 $\mu$ m-band enhancement data were evaluated in Ref 3 are presented in Fig IIIa-d. Similar altitude-dependence data for the seven 1976-77 missions of the NKC-135 optical aircraft are in Fig 4 of Ref 4. These two figures provide a complete listing of OI 6300 Å / N<sub>2</sub><sup>+</sup> 4278 Å mission ratio, characteristic energy of the incoming electrons, and peak emission altitude for the chemiluminous-yield ratios determined from the data taken by the zenith-pointing wide-angle SWIR radiometer and air fluorescence photometer (summarized in Table 2 of Ref 3).



Figures IIIa-d. Plots of 6300 Å/4278 Å emission ratio, characteristic energy of incoming electron flux, and altitude of peak energy deposition for the four 1978 and auroral flights evaluated in Ref 3.

Ratio 6300A/4278A  
 Characteristic Energy, keV  $\alpha$

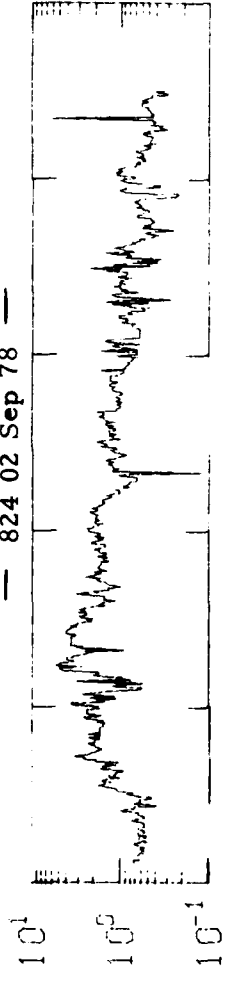


b

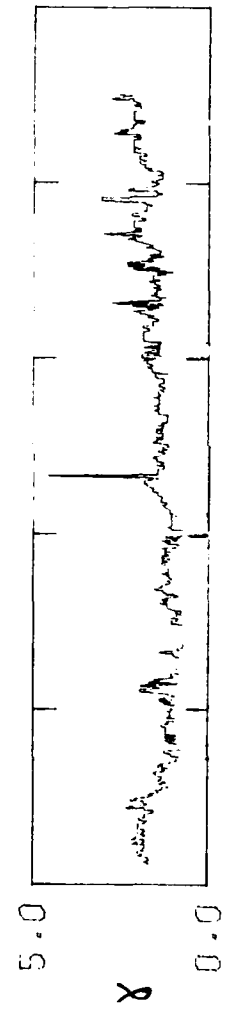
UNIVERSAL TIME (HR)

Ratio 6300Å/4278Å

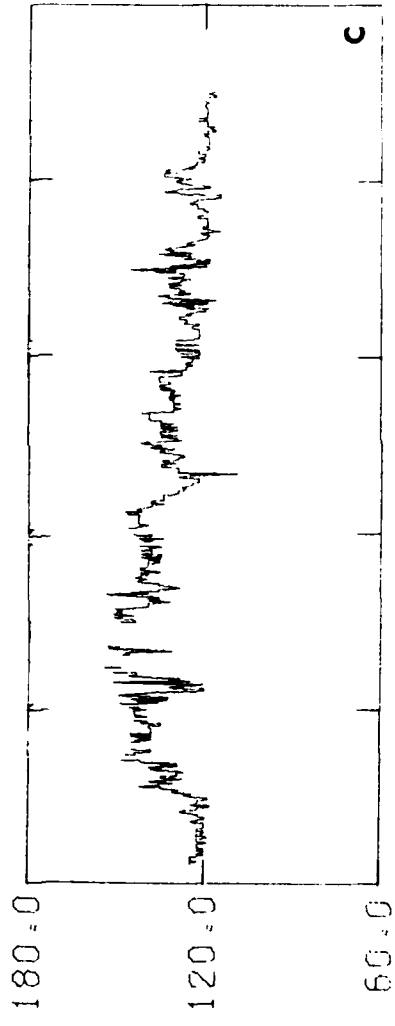
— 824 02 Sep 78 —



Characteristic Energy, keV

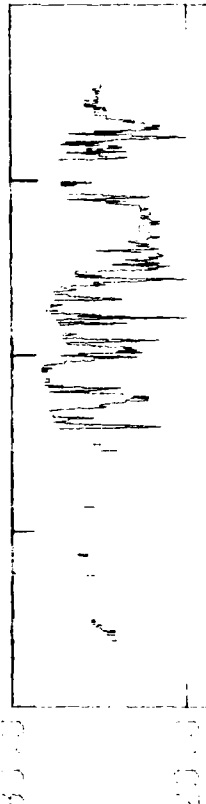
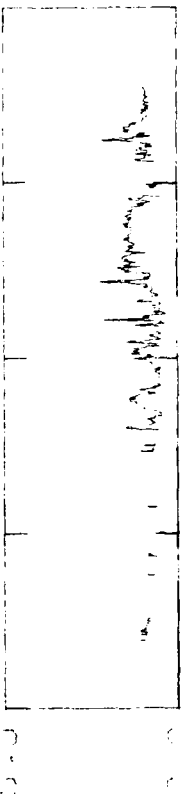
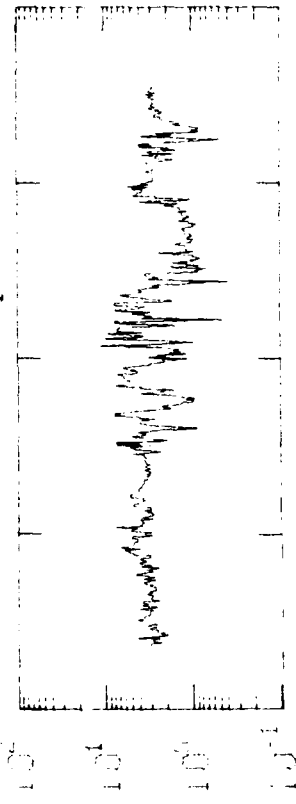


Altitude, km



UNIVERSAL TIME (HR)

826 07 Sep 78



UNIVERSITY TIME

**BLANK PAGE**

## DISTRIBUTION LIST

### DEPARTMENT OF DEFENSE

Assistant Secretary of Defense  
 Comm. Cnd. Cont & Intell  
 ATTN: Dir of Intelligence Sys, J. Babcock

Command & Control Technical Center  
 ATTN: C-312, R. Mason  
 ATTN: C-650, G. Jones  
 3 cy ATTN: C-650, W. Heidig

Defense Communications Agency  
 ATTN: Code 480  
 ATTN: Code 480, F. Dieter  
 ATTN: Code 810, J. Barna  
 ATTN: Code 205  
 ATTN: Code 101B

Defense Communications Engineer Center  
 ATTN: Code R123  
 ATTN: Code R410, N. Jones

Defense Intelligence Agency  
 ATTN: DT-5  
 ATTN: DB-4C, E. O'Farrell  
 ATTN: DB, A. Wise  
 ATTN: DT-1B  
 ATTN: Dir, E. Tighe  
 ATTN: DC-7D, W. Wittig

Defense Nuclear Agency  
 ATTN: NAFD  
 ATTN: STNA  
 ATTN: RAAE  
 ATTN: NATD  
 3 cy ATTN: RAAE  
 4 cy ATTN: TITL

Defense Technical Information Center  
 12 cy ATTN: DD

Field Command  
 Defense Nuclear Agency  
 ATTN: FCPR

Field Command  
 Defense Nuclear Agency  
 Livermore Branch  
 ATTN: FCPRL

Interservice Nuclear Weapons School  
 ATTN: TTV

Joint Chiefs of Staff  
 ATTN: C3S  
 ATTN: C3S, Evaluation Office

Joint Strat Tgt Planning Staff  
 ATTN: JLTW-2  
 ATTN: JLA

National Security Agency  
 ATTN: W-32, O. Bartlett  
 ATTN: B-3, F. Leonard  
 ATTN: R-52, J. Skillman

### DEPARTMENT OF DEFENSE (Continued)

Under Secretary of Defense for Resch & Engrg  
 ATTN: Strategic & Space Sys (OS)

AMCCS System Engineering Org  
 ATTN: R. Crawford

### DEPARTMENT OF THE ARMY

Assistant Chief of Staff for Automation & Comm.  
 Department of the Army  
 ATTN: DAAC-ZT, P. Henry

Atmospheric Sciences Laboratory  
 U.S. Army Electronics R&D Command  
 ATTN: DELAS-EO, F. Miles

BMD Advanced Technology Center  
 Department of the Army  
 ATTN: ATC-T, M. Capps  
 ATTN: ATC-O, W. Davies

BMD Systems Command  
 Department of the Army  
 2 cy ATTN: BMDSC-rw

Deputy Chief of Staff for Ops & Plans  
 Department of the Army  
 ATTN: DAMO-RQC

Harry Diamond Laboratories  
 Department of the Army  
 ATTN: DELHD-I-TL, M. Weiner  
 ATTN: DELHD-N-P, F. Wimenitz  
 ATTN: DELHD-N-RB, R. Williams  
 ATTN: DELHD-N-P

U.S. Army Chemical School  
 ATTN: ATZN-CM-CS

U.S. Army Comm-Elec Engrg Instal Agency  
 ATTN: CCC-EMEO-PED, G. Lane  
 ATTN: CCC-CEO-CCO, W. Neuendorf

U.S. Army Communications Command  
 ATTN: CC-OPS-W  
 ATTN: CC-OPS-WR, H. Wilson

U.S. Army Communications R&D Command  
 ATTN: DRDCO-COM-RY, W. Kesselman

U.S. Army Foreign Science & Tech Ctr  
 ATTN: DRXST-SQ

U.S. Army Materiel Dev & Readiness Cmd  
 ATTN: DRCLDC, J. Bender

U.S. Army Missile Intelligence Agency  
 ATTN: J. Gamble

U.S. Army Nuclear & Chemical Agency  
 ATTN: Library

U.S. Army Satellite Comm Agency  
 ATTN: Document Control

DEPARTMENT OF THE ARMY (Continued)

U.S. Army TRADOC Sys Analysis Actvy  
ATTN: ATAA-PL  
ATTN: ATAA-TDC  
ATTN: ATAA-TCC, F. Payan, Jr

DEPARTMENT OF THE NAVY

COMSPTEVFJR

Department of the Navy  
ATTN: Code 606, R. Berg

Joint Cruise Missiles Project ofc  
Department of the Navy  
ATTN: JCMG-707

Naval Air Development Center  
ATTN: Code 6091, M. Setz

Naval Air Systems Command  
ATTN: PMA 271

Naval Electronic Systems Command  
ATTN: PME 106-4, S. Kearney  
ATTN: PME 117-2013, G. Burnhart  
ATTN: PME 117-20  
ATTN: Code 3101, T. Hughes  
ATTN: Code 501A  
ATTN: PME 106-13, T. Griffin  
ATTN: PME 117-211, B. Kruger

Naval Intelligence Support Ctr  
ATTN: NISC-50

Naval Ocean Systems Center  
ATTN: Code 532, J. Bickel  
ATTN: Code 5322, M. Paulson  
3 cy ATTN: Code 5324, W. Moler  
3 cy ATTN: Code 5323, J. Ferguson

Naval Research Laboratory  
ATTN: Code 7550, J. Davis  
ATTN: Code 4137  
ATTN: Code 4750, S. Ossakow  
ATTN: Code 7500, B. Wald  
ATTN: Code 7950, J. Goodman  
ATTN: Code 4700, T. Coffey

Naval Space Surveillance System  
ATTN: J. Burton

Naval Surface Weapons Center  
ATTN: Code F31

Naval Telecommunications Command  
ATTN: Code 341

Office of Naval Research  
ATTN: Code 465  
ATTN: Code 420  
ATTN: Code 421

Office of the Chief of Naval Operations  
ATTN: OP 65  
ATTN: OP 941D  
ATTN: OP 981N

DEPARTMENT OF THE NAVY (Continued)

Strategic Systems Project Office  
Department of the Navy  
ATTN: NSP-2141  
ATTN: NSP-2722, F. Winterly  
ATTN: NSP-43

DEPARTMENT OF THE AIR FORCE

Aerospace Defense Command  
Department of the Air Force  
ATTN: DC, T. Long

Air Force Geophysics Laboratory  
ATTN: OPR, M. Gardiner  
ATTN: OPR-1  
ATTN: LEB, M. Champion  
ATTN: OPR, A. Stair  
ATTN: S. Basu  
ATTN: PnP  
ATTN: PnJ, J. Buchau  
ATTN: R. Thompson

Air Force Weapons Laboratory  
Air Force Systems Command  
ATTN: SCL  
ATTN: NTIC  
ATTN: NTN

Air Force Wright Aeronautical Lab  
ATTN: W. Hunt  
ATTN: A. Johnson

Air University Library  
Department of the Air Force  
ATTN: AUL-LSE

Air Weather Service, MAC  
Department of the Air Force  
ATTN: DWP, R. Babcock

Assistant Chief of Staff  
Studies & Analyses  
Department of the Air Force  
ATTN: AF/SASC, W. Neaus  
ATTN: AF/SASC, C. Rightmeyer

Ballistic Missile Office  
Air Force Systems Command  
ATTN: ENSH, J. Allen

Deputy Chief of Staff  
Operations Plans and Readiness  
Department of the Air Force  
ATTN: AFXOKT  
ATTN: AFXOXFD  
ATTN: AFXOKS  
ATTN: AFXOKCD

Deputy Chief of Staff  
Research, Development, & Acq  
Department of the Air Force  
ATTN: AFRDS  
ATTN: AFRDSP  
ATTN: AFRDSS

DEPARTMENT OF THE AIR FORCE (Continued)

Electronic Systems Division  
Air Force Systems Command  
ATTN: DCKC, J. Clark

Electronic Systems Division  
Air Force Systems Command  
ATTN: XRW, J. Deas

Electronic Systems Division  
Air Force Systems Command  
ATTN: YSEA  
ATTN: YSM, J. Kobelski

Foreign Technology Division  
Air Force Systems Command  
ATTN: TQTD, B. Ballard  
ATTN: NUIS, Library

Headquarters Space Division  
Air Force Systems Command  
ATTN: SKY, C. Kennedy  
ATTN: SKA, D. Bolin

Headquarters Space Division  
Air Force Systems Command  
ATTN: YZJ, W. Mercer

Headquarters Space Division  
Air Force Systems Command  
ATTN: E. Butt

Rome Air Development Center  
Air Force Systems Command  
ATTN: OCS, V. Coyne  
ATTN: TSLD

Rome Air Development Center  
Air Force Systems Command  
ATTN: EEP

Strategic Air Command  
Department of the Air Force  
ATTN: DCXT  
ATTN: NRT  
ATTN: DCXR, T. Jorgensen  
ATTN: DCX  
ATTN: XPFS

OTHER GOVERNMENT AGENCIES

Central Intelligence Agency  
ATTN: OSWR/NED

Department of Commerce  
National Bureau of Standards  
ATTN: Sec Ofc for R. Moore

Department of Commerce  
National Oceanic & Atmospheric Admin  
ATTN: R. Grubb

Institute for Telecommunications Sciences  
National Telecommunications & Info Admin  
ATTN: W. Utlaut  
ATTN: A. Jean  
ATTN: L. Berry

U.S. Coast Guard  
Department of Transportation  
ATTN: G-DOE-3/TP54, B. Romine

DEPARTMENT OF ENERGY CONTRACTORS

EG&G, Inc  
ATTN: D. Wright  
ATTN: J. Colvin

Lawrence Livermore National Lab  
ATTN: L-369, R. Ott  
ATTN: L-31, R. Hager  
ATTN: Technical Info Dept, Library

Los Alamos National Lab  
ATTN: MS 664, J. Zinn  
ATTN: D. Simons  
ATTN: P. Reaton  
ATTN: D. Westervelt  
ATTN: E. Jones  
ATTN: R. Taschek  
ATTN: MS 670, J. Hopkins

Sandia Laboratories  
Livermore Laboratory  
ATTN: E. Murphey  
ATTN: T. Cook

Sandia National Lab  
ATTN: ORG 1250, W. Brown  
ATTN: ORG 4241, T. Wright  
ATTN: Space Project Div  
ATTN: 3141  
ATTN: D. Thornbrough  
ATTN: D. Dahlgren

DEPARTMENT OF DEFENSE CONTRACTORS

Aerospace Corp  
ATTN: I. Garfunkel  
ATTN: S. Bower  
ATTN: D. Olsen  
ATTN: N. Stockwell  
ATTN: R. Slaughter  
ATTN: V. Josephson  
ATTN: T. Salmi  
ATTN: J. Straus

University of Alaska  
ATTN: T. Davis  
ATTN: N. Brown  
ATTN: Technical Library

Analytical Systems Engineering Corp  
ATTN: Radio Sciences

Analytical Systems Engineering Corp  
ATTN: Security

Barry Research Corporation  
ATTN: J. McLaughlin

BDM Corp  
ATTN: L. Jacobs  
ATTN: T. Neighbors

Berkeley Research Associates, Inc  
ATTN: J. Workman

BETAC  
ATTN: J. Hirsch

Booz-Allen & Hamilton, Inc  
ATTN: B. Wilkinson

## DEPARTMENT OF DEFENSE CONTRACTORS (Continued)

Boeing Co  
 ATTN: M/S 42-33, J. Kennedy  
 ATTN: G. Hall  
 ATTN: S. Tashird

University of California at San Diego  
 ATTN: H. Booker

Charles Stark Draper Lab, Inc  
 ATTN: J. Gilmore  
 ATTN: D. Cox

Communications Satellite Corp  
 ATTN: D. Fang

Comsat Labs  
 ATTN: R. Taur  
 ATTN: G. Hyde

Cornell University  
 ATTN: M. Kelly  
 ATTN: D. Farley, Jr

Electrospace Systems, Inc  
 ATTN: H. Logston

ESL, Inc  
 ATTN: J. Marshall

General Electric Co  
 ATTN: M. Bortner  
 ATTN: A. Harcar

General Electric Co  
 ATTN: A. Steinmayer  
 ATTN: C. Zierdt

General Electric Co  
 ATTN: F. Reibert

General Electric Co  
 ATTN: G. Millman

General Research Corp  
 ATTN: J. Ise, Jr  
 ATTN: J. Garbarino

Harris Corp  
 ATTN: E. Knick

Horizons Technology, Inc  
 ATTN: R. Kruger

HSS, Inc  
 ATTN: D. Hansen

IBM Corp  
 ATTN: F. Ricci

University of Illinois  
 ATTN: Security Supervisor for K. Yeh

Institute for Defense Analyses  
 ATTN: J. Bengston  
 ATTN: E. Bauer  
 ATTN: H. Wolfhard  
 ATTN: J. Aein

## DEPARTMENT OF DEFENSE CONTRACTORS (Continued)

International Tel & Telegraph Corp  
 ATTN: G. Wetmore  
 ATTN: Technical Library

JAYCOR  
 ATTN: J. Sperling

JAYCOR  
 ATTN: J. DonCarlos

Johns Hopkins University  
 ATTN: T. Potemra  
 ATTN: J. Phillips  
 ATTN: T. Evans  
 ATTN: J. Newland  
 ATTN: P. Komiske

Kaman Tempo  
 ATTN: DASIAC  
 ATTN: W. McNamara  
 ATTN: T. Stephens  
 ATTN: W. Knapp

Linkabit Corp  
 ATTN: I. Jacobs

Litton Systems, Inc  
 ATTN: R. Grasty

Lockheed Missiles & Space Co, Inc  
 ATTN: W. Imhof  
 ATTN: M. Walt  
 ATTN: R. Johnson

Lockheed Missiles & Space Co, Inc  
 ATTN: Dept 60-12

M.I.T. Lincoln Lab  
 ATTN: D. Towle

Martin Marietta Corp  
 ATTN: R. Heffner

McDonnell Douglas Corp  
 ATTN: W. Olson  
 ATTN: J. Moule  
 ATTN: G. Mroz  
 ATTN: R. Halprin  
 ATTN: N. Harris

Meteor Communications Consultants  
 ATTN: R. Leader

Mission Research Corp  
 ATTN: R. Kilb  
 ATTN: R. Bogusch  
 ATTN: Tech Library  
 ATTN: R. Hendrick  
 ATTN: D. Sappenfield  
 ATTN: S. Gutsche  
 ATTN: F. Fajen

Mitre Corp  
 ATTN: G. Harding  
 ATTN: A. Kymmel  
 ATTN: B. Adams  
 ATTN: C. Callahan

DEPARTMENT OF DEFENSE CONTRACTORS (Continued)

Mitre Corp  
ATTN: M. Horrocks  
ATTN: J. Wheeler  
ATTN: W. Foster  
ATTN: W. Hall

Pacific-Sierra Research Corp  
ATTN: E. Field, Jr  
ATTN: H. Brode  
ATTN: F. Thomas

Pennsylvania State University  
ATTN: Ionospheric Research Lab

Photometrics, Inc  
ATTN: I. Kofsky  
4 cy ATTN: D. Villanucci  
4 cy ATTN: R. Sluder

Physical Dynamics, Inc  
ATTN: E. Fremouw

Physical Research, Inc  
ATTN: R. Deliberis

R & D Associates  
ATTN: R. Lelevier  
ATTN: F. Gilmore  
ATTN: M. Gantsweg  
ATTN: C. Greifinger  
ATTN: B. Gabbard  
ATTN: W. Karzas  
ATTN: W. Wright  
ATTN: R. Turco  
ATTN: H. Ory  
ATTN: P. Haas

R & D Associates  
ATTN: B. Yoon

Rand Corp  
ATTN: C. Crain  
ATTN: E. Bedrozian

Riverside Research Institute  
ATTN: V. Trapani

Rockwell International Corp  
ATTN: R. Buckner

Rockwell International Corp  
ATTN: S. Quilici

DEPARTMENT OF DEFENSE CONTRACTORS (Continued)

Santa Fe Corp  
ATTN: D. Paolucci

Science Applications, Inc  
ATTN: C. Smith  
ATTN: L. Linson  
ATTN: E. Straker  
ATTN: D. Hamlin

Science Applications, Inc  
ATTN: SZ

Science Applications, Inc  
ATTN: J. Cockayne

SRI International  
ATTN: W. Jaye  
ATTN: R. Leadabrand  
ATTN: D. Neilson  
ATTN: C. Rino  
ATTN: J. Petrickes  
ATTN: W. Chesnut  
ATTN: R. Livingston  
ATTN: R. Tsunoda  
ATTN: G. Smith  
ATTN: G. Price  
ATTN: M. Baron  
ATTN: A. Burns

Sylvania Systems Group  
ATTN: M. Cross

Technology International Corp  
ATTN: W. Boquist

Tri-Com, Inc  
ATTN: D. Murray

TRW Defense & Space Sys Group  
ATTN: D. Dee  
ATTN: R. Plebuch

Utah State University  
ATTN: K. Baker  
ATTN: L. Jensen  
ATTN: J. Dupnik

Visidyne, Inc  
ATTN: C. Humphrey  
ATTN: J. Carpenter

**DATE**  
**ILME**